Prediction of flow-induced vibration in shell-and-tube heat exchangers

by

Marilize van Zyl

Submitted in partial fulfilment of the requirements for the degree

M.Eng.

in the Faculty of Engineering, the Built Environment and Information Technology
University of Pretoria

Pretoria

July 2004

Prediction of flow-induced vibration in shell-and-tube heat exchangers

by

Marilize van Zyl

Supervisors : Prof. P.S. Heyns
Prof. K.J. Craig
Department : Mechanical and Aeronautical Engineering
Degree : M.Eng.

Summary

Flow-induced vibration can cause premature tube failure in shell-and-tube heat exchangers and is therefore incorporated in the heat exchanger design, together with the heat transfer and pressure drop, as a primary concern. In this study three methods for the prediction of flow-induced vibration were investigated. The results of the three methods were compared with each other and with experimental data. For comparison purposes vibration measurements were taken on a Tail gas shell-and-tube heat exchanger at Sasol Synthetic Fuels (SSF).

Firstly, software developed by the Heat Transfer Research Institute (HTRI) was used to predict flow-induced vibration in the Tail gas shell-and-tube heat exchanger. The HTRI analyses calculated excitation frequencies due to vortex shedding, turbulence buffeting, fluid-elastic instability and acoustic resonance. These excitation frequencies were then compared to the lowest HTRI calculated natural frequency of the tubes (using a 20 percent margin of uncertainty) to predict whether vibration would occur. Additional natural frequency calculations were made to determine higher natural frequencies of the tubes, using equations from the Tubular Exchanger Manufacturers Association (TEMA) standards. Finite Element Methods (FEM) were used to determine the effect that the support configurations have on the tubes' natural frequencies.

Secondly, Computational Fluid Dynamic (CFD) analyses were used to simulate the flow velocities and pressure drops through the heat exchanger. These results were

compared with the HTRI predicted average cross-flow velocity and pressure drop values.

Thirdly, vibration measurements were recorded on the Tail gas heat exchanger using Siglab 20-42 data acquisitioning equipment. Vibration on the heat exchanger shell was measured using strain gauges as well as 500 mV/g and 100 mV/g accelerometers. Support vibration measurements were recorded using 2 V/g accelerometers.

The CFD analyses predicted that vibration (for a specific excitation frequency) would occur over a range of mass flow rates, while the HTRI analyses only predicted vibration at a single mass flow rate. The experimental results confirmed that vibration did occur at the HTRI predicted natural frequency, but also over a range of other mass flow rates, as predicted by the CFD analyses.

Keywords: Flow-induced vibration, vortex shedding, turbulence buffeting, fluid-elastic instability, shell-and-tube heat exchanger, tube vibration, tubes in cross-flow, Computational Fluid Dynamic (CFD) analysis, Finite Element Methods (FEM), Heat Transfer Research Institute (HTRI) analysis.

Voorspelling van vloei-geïnduseerde vibrasie in dop-en-buis hitteruilers

deur

Marilize van Zyl

Studieleiers : Prof. P.S. Heyns
Prof. K.J. Craig
Departement : Meganiese en Lugvaartkundige Ingenieurswese
Graad : M.Ing.

Opsomming

Vloei-geïnduseerde vibrasie in dop-en-buis hitteruilers kan veroorsaak dat die buise voor hul verwagte ontwerpleeftyd faal. Dit is dus noodsaaklik om vibrasie analises in te sluit by die ontwerp van hitteruilers, tesame met warmteoordrag en drukval as primêre oorwegings. In hierdie studie word drie metodes vir die voorspelling van vloei-geïnduseerde vibrasie ondersoek, onderling vergelyk, en ook met eksperimentele waarnemings vergelyk. Vir hierdie doel is 'n afvoer gas dop-en-buis hitteruiler by Sasol Sintetiese Brandstowwe (SSF) gebruik.

Eerstens is daar van sagteware, wat deur die *Heat Transfer Research Institute* (HTRI) versprei word, gebruik gemaak om vloei-geïnduseerde vibrasie in die hitteruiler te voorspel. Die HTRI analises bereken die opwekkingsfrekwensies as gevolg van vorteks afgooiing, turbulente opwekking, vloei-elastiese onstabiliteit en akoestiese resonansie. Die opwekkingsfrekwensies word dan met die laagste HTRI berekende natuurlike frekwensie van die buise vergelyk (deur van 'n 20 persent onsekerheidsband gebruik te maak) om te bepaal of die buise gaan vibreer. Addisionele natuurlike frekwensies, hoër as die HTRI natuurlike frekwensie van die buise, is bereken met behulp van die *Tubular Exchanger Manufacturers Association* (TEMA) standaarde. Eindige element metodes is gebruik om die effek wat die buis ondersteuning op die natuurlike frekwensies van die buise het, te bepaal.

Tweedens is berekenings vloei-dinamika (CFD) analises gebruik om die vloeisnelhede en drukval deur die hitteruiler te simuleer. Hierdie resultate is met die HTRI analises se gemiddelde dwarsvloei snelhede en drukvalle vergelyk.

Derdens is vibrasiemetings op die afvoer gas hitteruiler geneem deur van die Siglab 20-42 dataverwerker gebruik te maak. Vibrasie op die dop van die hitteruiler is met behulp van rekstrokies, sowel as 500 mV/g en 100 mV/g versnellingsmeters gemeet. Die voetstukvibrasie van die hitteruiler is met 2 V/g versnellingsmeters gemeet.

Die CFD analises het voorspel dat vibrasie (vir 'n spesifieke opwekkingsfrekwensie) sal voorkom oor 'n band van massavloeitempo's, terwyl die HTRI analises vibrasie slegs by 'n enkele massavloeitempo voorspel het. Die eksperimentele resultate bevestig dat vibrasie wel by die HTRI voorspelde frekwensie voorkom, maar ook oor 'n band van massavloeitempo's, soos die CFD analises voorspel het.

Sleutelwoorde: Vloei-geïnduseerde vibrasie, vorteks afgooiing, turbulente opwekking , Vloei-elastiese onstabiliteit, dop-en-buis hitteruilers, buis vibrasie, buise in dwarsvloei, berekenings vloei dinamika analises, eindige element metodes, *Heat Transfer Research Institute* (HTRI) analises.

Acknowledgements

I would like to thank the following people for their contributions:

- Prof. K.J. Craig and Prof. P.S. Heyns.
- Hein Botes my mentor at Sastech for all his support, as well as Daan le Roux for all his help.
- Chris Roets from SSF for his help with the measurements at Sasol.
- Dr. Albert Zapke from GEA for the use of their software.
- Danie de Kock for his help with the flow simulations.
- Danie Gouws for his help with the strain gauges.
- Francois du Plooy for his help with the vibration measurements.
- Sasol for their financial support.
- Anton van der Hoven for all his help and support.

Table of contents

Nomenclature

A	Area	m^2
A_f	Fin surface area	m^2
A_g	Gap Area	m^2
A_p	Prime (unfinned) area	m^2
a	Amplitude	m
C	Fluid force coefficient	
C_D	Drag coefficient	
C'_D	Fluctuating drag coefficient	
C_L	Lift coefficient	
C'_L	Fluctuating lift coefficient	
C_n	Frequency constant	
C_u	U-tube frequency constant	
c_r	Critical velocity	m/s
d	Characteristic length	m
d_o	Tube outside diameter	in
D	Diameter	m
D_i	Tube inside diameter	m
D_o	Tube outside diameter	m
E	Modulus of elasticity	N/m^2
F	Force	N
f	Friction factor	
f_a	Acoustic frequency	Hz
f_n	Natural frequency	Hz
f_{ns}	Stressed tube natural frequency	Hz
f_{nu}	U-tube natural frequency	Hz
f_s	Acoustic shedding frequency	Hz
f_{tb}	Turbulent buffeting frequency	Hz
f_{tba}	Acoustic turbulence buffeting frequency	Hz
f_{vs}	Vortex shedding frequency	Hz
f_{vsa}	Acoustic vortex shedding frequency	Hz
g'	Fluctuating forces in the x-direction	N
h	Height	m
h'	Fluctuating forces in the y-direction	N
I	Second moment of area	m^4
K	Turbulence kinetic energy	m^2/s^2
	Stiffness	N/m
K_{gv}	Gate value loss coefficient	
K_t	Total loss coefficient	

k	Added mass coefficient	
L	Length	m
L_{mid}	Mid-span length	m
l	Effective flow length	m
l_n	Length associated with n^{th} mode shape	m
M_e	Effective mass per unit length	kg/m
M_m	Material mass per unit length	kg/m
M_s	Virtual mass per unit length of shell-side fluid displaced by the tube	kg/m
M_t	Mass per unit length of the fluid inside the tube	kg/m
$\dot{m}$	Mass flow rate	kg/s
m_n	Effective mass per unit length of the n^{th} mode	kg/m
N	Number of spans	
P	Perimeter	m
	Pressure	Pa
	Tube pitch	m
P_a	Axial load	N
ΔP	Pressure drop	Pa
p_l	Longitudinal tube pitch	m
p_t	Transverse tube pitch	m
q	Distributed load	N/m
R	U-tube bend radius	m
	Particular gas constant	kNm/kmolK
$\bar{R}$	Universal gas constant	kNm/kmolK
Re	Reynolds number	
r	Radius	m
S_a	Acoustic Strouhal number	
Sr	Strouhal number	
t_b	Baffle plate thickness	in
U_g	Cross flow velocity in gaps	m/s
u	Velocity in x-direction	m/s
u_c	Cross flow velocity	m/s
u_∞	Free stream velocity	m/s
V	Volume	m^3
v	Velocity in y-direction	m/s
w_o	Effective weight per unit length	lb
X_p	Pitch to diameter ratio	
y^+	Wall plus value	

Greek symbols

$\bar{\bar{\alpha}}$	Added mass matrix	
$\bar{\bar{\alpha}}'$	Damping matrix	
$\bar{\bar{\alpha}}''$	Stiffness matrix	
$\bar{\bar{\beta}}$	Added mass matrix	
$\bar{\bar{\beta}}'$	Damping matrix	
$\bar{\bar{\beta}}''$	Stiffness matrix	
δ	Logarithmic damping	
δ_b	Tip deflection	m
ε	Roughness	m
	Strain	
	Turbulent dissipation	
Φ	Mode shape	
Φ_D	Drag force phase angle	rad
Φ_L	Lift force phase angle	rad
κ	Curvature	m
λ	Ratio of end zone span length to central span length	m
μ	Viscosity	Pas
ρ	Mass density	kg/m^3
ρ_o	Reference fluid density	lb/in^3
ρ_s	Mass density of shell-side fluid	kg/m^3
$\bar{\bar{\sigma}}$	Added mass matrix	
$\bar{\bar{\sigma}}'$	Damping matrix	
$\bar{\bar{\sigma}}''$	Stiffness matrix	
Ω_D	Drag force circular frequency	rad/s
Ω_L	Lift force circular frequency	rad/s
$\bar{\bar{\tau}}$	Added mass matrix	
$\bar{\bar{\tau}}'$	Damping matrix	
$\bar{\bar{\tau}}''$	Stiffness matrix	
ξ	Damping ratio	
ξ_n	Damping ratio of the n^{th} mode	

Abbreviations

CFD	Computational Fluid Dynamics
FEI	Fluid-Elastic Instability

FEA	Finite Element Analysis
HEDH	Heat Exchanger Design Handbook
HTFS	Heat Transfer and Fluid flow Services
HTRI	Heat Transfer Research Institute
PSD	Power Spectral Density
SSF	Sasol Synthetic Fuels
TEMA	Tubular Exchangers Manufacturing Association

Heat exchanger classifications according to TEMA

BEM	Bonnet, One Pass Shell, Fixed Tubesheet
AKL	Channel, Two Pass Shell, Fixed Tubesheet
CEU	Channel Integral with Tubesheet, One Pass Shell, U-Tube Bundle
CEN	Channel Integral with Tubesheet, One Pass Shell, Fixed Tubesheet
R	Petroleum and related processing applications

Chapter 1

Introduction

1.1 Motivation

Flow-induced vibration in shell-and-tube heat exchangers has been studied for more than 40 years. More intensified efforts for the prediction of failure in shell-and-tube heat exchangers are being made because of the cost associated with premature failure. Several phenomena associated with flow-induced vibration exist. These include fluid-elastic instability, acoustic resonance, vortex shedding, turbulence buffeting and parallel-flow eddy formation. Tube vibration is not only caused by the excitation frequencies associated with the above mentioned phenomena, but also by motion dependent fluid forces, which are in turn caused by tube vibration, as described by Goyder and Whalley (1987).

Sasol Synthetic Fuels (SSF) uses more than two thousand shell-and-tube heat exchangers in their processes. In a never-ending quest for excellence, plant production capacities is ever increasing. This often leads to the operation of equipment, including shell-and-tube heat exchangers, above their intended design limits. Because shell-and-tube heat exchangers are susceptible to flow-induced vibration, vibration analyses are required in such instances. Several assessment methods exist, as described in the Heat Exchanger Design Handbook HEDH (1998) and Tubular Exchangers Manufacturing Association TEMA (1988). These methods are used in software such as the Heat Transfer and Fluid Flow Services HTFS (1992) and the Heat Transfer Research Institute HTRI packages. These methods however, use large margins of uncertainty (in the order of 20 percent) for the prediction of flow-induced vibration. Because of the high replacement cost of heat exchangers, additional methods are required to predict and verify vibration problems and the extent thereof.

Numerous vibration experiments have been conducted under controlled conditions, using single tubes or ideal tube banks exposed to uniform cross-flow or parallel-flow velocities. Very few investigations have addressed the specific problems associated with industrial heat exchanger configurations. The application of results from ideal test conditions is often difficult, because of

differences in geometry, in the way the flow is coupled to the motion of the tubes, and in the non-uniformity of the velocities throughout the bundle. Consequently, the ability to accurately predict the intensity of flow-induced vibration, or the probability of damage, is less than certain (Chenoweth, 1998).

1.2 Literature study: Flow-induced vibration

In the literature study the tube bundle vibration and natural frequencies will be described, followed by the mechanisms that cause tube vibration and the failures associated with excessive vibration. The literature study also includes a case study of a shell-and-tube heat exchanger that failed during operational conditions. Four heat exchanger vibration studies from Sasol are also included in the case study.

1.2.1 Tube bundle vibration

The natural frequency of a tube is dependent on the material properties, span length, geometry and supports.

Natural frequencies of straight tubes

In a shell-and-tube heat exchanger it is adequate to determine the lowest frequency only. If assuming that the tubes are fixed at the tubesheets and simply supported at the baffles with equal span length between the baffles, the following approach by Chenoweth (1998) can be used:

$$f_n = \frac{C_n}{2\pi}\left(\frac{EI}{M_e L^4}\right)^{0.5} \qquad 1.1$$

where the effective mass per unit length (M_e) can be determined as described by TEMA. Values for C_n are given in figure 1.1. E, I and L are the modulus of elasticity, second moment of area and unsupported tube length respectively. Most heat exchangers have their longest unsupported span length passing through the baffle window or in the entrance or exit zones. It is therefore necessary to determine the lowest natural frequency by considering all the possible combinations as described in figure 1.1.

A further aspect to consider is the effect of axial stresses, which may be caused by manufacturing procedures or operating conditions like thermal expansion. If

the axial force (P_a) is known, the natural frequency can be modified using the following relationship:

$$f_{ns} = f_n\left(1+\frac{P_a L^2}{EI\pi^2}\right)^{0.5} \qquad 1.2$$

If the axial force is compressive, the sign of P_a is negative and the natural frequency decreases. The variation in natural frequency due to axial forces may be as much as 40 percent, as described by Kissel (1972). Tube to baffle hole clearances have little effect on the natural frequency but are important when considering the amount of damping and tube wear.

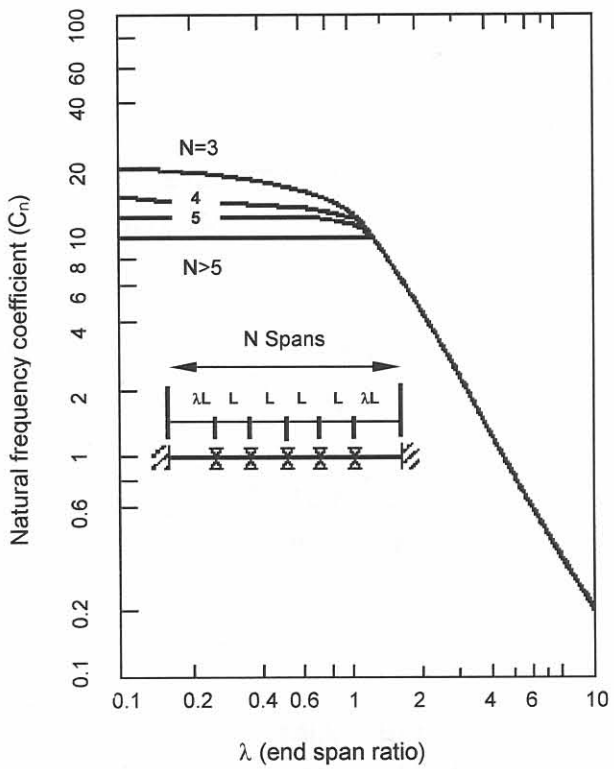

Figure 1.1: Straight tube natural frequency coefficients (Chenoweth, 1998)

Natural frequencies of U-tubes

TEMA uses equation 1.3 to obtain the lowest natural frequency:

$$f_{nu} = 59.55\frac{C_u}{R^2}\left(\frac{EI}{M_e}\right)^{0.5} \qquad 1.3$$

Where R is the U-tube radius. Values for C_u for different support configurations can be obtained, as described by the TEMA specifications.

Finned-tube natural frequencies

Finned-tube natural frequencies can be determined using equation 1.1, if the second moment of area (I) in the equation is calculated using an effective diameter and the mass per unit length is taken as the actual mass of the finned section. This is only true if the finned-tubes enter the baffles in such a manner that the assumption of simple supports is satisfied.

1.2.2 Damping

The amplitude of vibration is strongly dependent on the damping of the system. The following equations for logarithmic decrement, (δ) given by TEMA, are based on idealised models and experimental observations. For shell side liquids δ is equal to the greater of δ_1 or δ_2:

$$\delta_1 = \frac{3.41 d_o}{w_o f_n} \tag{1.4}$$

$$\delta_2 = \frac{0.012 d_o}{w_o}\left[\frac{\rho_o v}{f_n}\right]^{0.5} \tag{1.5}$$

For shell side vapours:

$$\delta = \frac{0.314(N-1)}{N}\left[\frac{t_b}{l}\right]^{0.5} \tag{1.6}$$

where w_o is the effective weight in lb, ρ_o is the density of the shell side fluid in lb/in^3 and d_o (inches) is the outside diameter of the tubes. For calculating the damping for vapours, the baffle plate thickness (t_b), length (l) and the number of spans (N) are used in equation 1.6. For two-phase flow cases see Kawamura *et al.* (1997) and Gidi *et al.* (1997).

1.2.3 Fluid forces

Fluid forces can be divided into fluid excitation forces (figure 1.2) and motion-dependent fluid forces (Chen, 1991 and 1992).

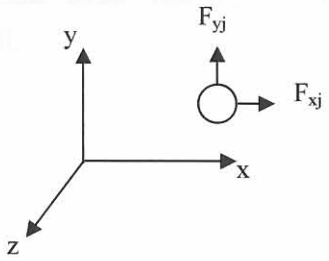

Figure 1.2: Tube force directions

Fluid excitation forces:

$$F_{xj} = \frac{1}{2}\rho U^2 DC_{Dj} + \frac{1}{2}\rho U^2 DC_{Dj}^{'} \sin(\Omega_{Dj} + \Phi_{Dj}) + g_j^{'} \qquad 1.7$$

$$F_{yj} = \frac{1}{2}\rho U^2 DC_{Lj} + \frac{1}{2}\rho U^2 DC_{Lj}^{'} \sin(\Omega_{Lj} + \Phi_{Lj}) + h_j^{'} \qquad 1.8$$

where D is the diameter of the cylinder and U is the flow velocity. C_D and C_L are the steady drag and lift coefficients with $C_D^{'}$ and $C_L^{'}$ the fluctuation of the coefficients. Ω is the circular frequency of periodic flow with Φ the corresponding phase angle with respect to a particular fluid-force component. $h^{'}$ and $g^{'}$ represent other fluctuating forces such as turbulent buffeting forces.

Motion-dependent fluid forces:

$$F_{xj} = -\sum_{k=1}^{N}\left[\left(\bar{\alpha}_{jk}\frac{\partial^2 u_k}{\partial t^2} + \bar{\alpha}_{jk}^{'}\frac{\partial u_k}{\partial t} + \bar{\alpha}_{jk}^{''}u_k\right) + \left(\bar{\sigma}_{jk}\frac{\partial^2 v_k}{\partial t^2} + \bar{\sigma}_{jk}^{'}\frac{\partial v_k}{\partial t} + \bar{\sigma}_{jk}^{''}v_k\right)\right] \qquad 1.9$$

$$F_{yj} = -\sum_{k=1}^{N}\left[\left(\bar{\tau}_{jk}\frac{\partial^2 u_k}{\partial t^2} + \bar{\tau}_{jk}^{'}\frac{\partial u_k}{\partial t} + \bar{\tau}_{jk}^{''}u_k\right) + \left(\bar{\beta}_{jk}\frac{\partial^2 v_k}{\partial t^2} + \bar{\beta}_{jk}^{'}\frac{\partial v_k}{\partial t} + \bar{\beta}_{jk}^{''}v_k\right)\right] \qquad 1.10$$

where $\bar{\alpha}_{jk}$, $\bar{\beta}_{jk}$, $\bar{\tau}_{jk}$ and $\bar{\sigma}_{jk}$ are added mass matrices; $\bar{\alpha}_{jk}^{'}$, $\bar{\beta}_{jk}^{'}$, $\bar{\tau}_{jk}^{'}$ and $\bar{\sigma}_{jk}^{'}$ are damping matrices, $\bar{\alpha}_{jk}^{''}$, $\bar{\beta}_{jk}^{''}$, $\bar{\tau}_{jk}^{''}$ and $\bar{\sigma}_{jk}^{''}$ are fluid stiffness matrices and subscript j and k indicates the tube position.

1.2.4 Excitation mechanisms for tube vibration

It is possible that vibration can be transmitted from an external source to the heat exchanger through foundations or supporting structures. This research, however, is limited to flow-induced tube vibration. The following mechanisms will be discussed in more detail:

- Fluid-elastic instability
- Vortex shedding
- Acoustic resonance
- Turbulence buffeting
- Flow pulsation
- Parallel-flow eddy formation

Fluid-elastic instability

Chenoweth (1998) characterises Fluid-Elastic Instability (FEI) as a whirling type of tube vibration with the tube deflection moving orbitally. Flow across the tubes produces a combination of drag and lift forces. Brenneman and Gurdal (1997) describes the fluid elastic mechanism in tube bundles as a simple first-order mechanism that is proportional to the dynamic pressure in the fluid flowing between the tubes and inversely proportional to the zero-crossing frequency of the relative tube responses. Fluid-elastic instability is important in both liquids and gasses. If the fluid velocity is above the critical velocity, a drastic increase in vibration amplitude will occur (figure 1.3).

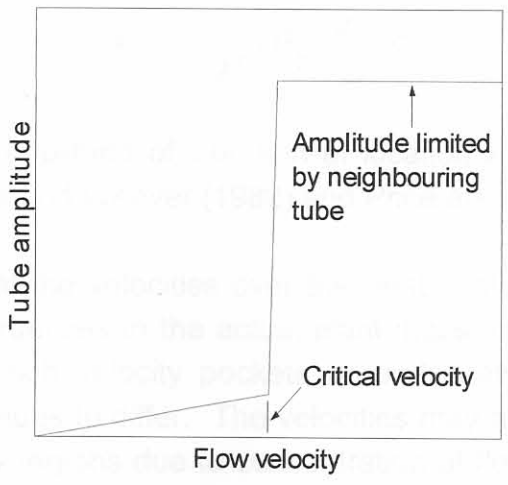

Figure 1.3: Variation of tube amplitude with flow velocity (HTFS).

Goyder (1997) examined the margins of uncertainty in which FEI in heat exchanger tube bundles can be predicted and the actual occurrence of damaging vibration. The following inequality for assessing the stability of a tube bundle is given by Goyder (1997):

$$\frac{2\pi\zeta_n m_n}{\rho_o D^2} > \int_0^L \frac{\rho(z)}{\rho_o}\left[\left(\frac{U_g}{f_n D}\right)^2 \frac{C}{8\pi}\right]\frac{\Phi_n^2(z)}{l_n}dz \qquad 1.11$$

The inequality must be satisfied for stability. C is the fluid force coefficient and Φ is the mode shape. ξ_n and m_n are the damping and mass at the nth natural frequency. The gap flow velocity (U_g) is defined by:

$$U_g = \frac{G}{\rho A}\left(\frac{P}{P-D}\right) \qquad 1.12$$

The mode shapes can broadly be classified in two categories. Firstly tubes with a relatively long end span where most of the vibration occurs. In this case the end spans may be treated as single span tube bundles and the mid-spans may be ignored. Alternatively the end spans may be relatively short. In this case the tube can be modelled as a set of equally spaced mid spans with an approximate mode shape. The end-span length is taken equal to the mid-span length.

$$\Phi(x) = \sin\left(\frac{\pi x}{NL_{mid}}\right)\sin\left(\frac{\pi x}{L_{mid}}\right) \qquad 1.13$$

The forces associated with the gap flow velocity are given in terms of the fluid force coefficient C, which relate the force to the amplitude of vibration.

$$F(x) = \frac{1}{2}\rho U_g^2 D\frac{a(x)}{D}C \qquad 1.14$$

where $a(x)$ is the amplitude of vibration at location x. Values for C have been developed by Lever and Weaver (1982) and Price and Paidoussis (1984).

The problem is that the velocities over the heat exchanger tube bundle are not well known. Uncertainties in the actual plant mass flow rate, gas density, cross flow fraction and high velocity pockets around sealing strips, may cause the nominal velocity values to differ. The velocities may also be different because of nozzle and window regions due to concentration of flow. The influencing factors have a typical uncertainty value of 20 percent. In a turbulence, stability and wear

analysis of a steam generator, Brenneman and Gurdal (1997) showed that the critical fluid-elastic velocity is only a weak function of the tube-to-baffle clearances.

Kassera (1997) analysed a single elastically mounted tube in cross flow with a three-dimensional Computational (CFD) code as shown in figure 1.4. Results were obtained for rigid and vibrating tubes. When the vibrations of the tubes are taken into account, much better correlation with experimental data is obtained.

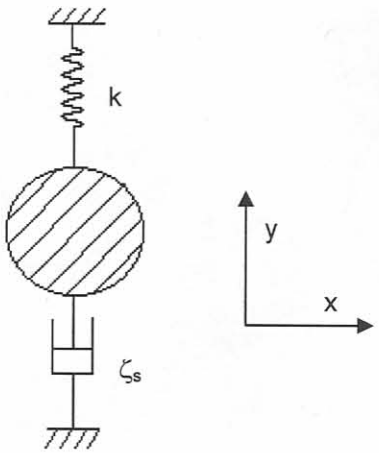

Figure 1.4: Spring and dashpot system used by Kassera (1997)

To calculate the flow-induced vibration (vibrating tubes) first, the flow field is calculated using a CFX (Reynolds-stress model). The drag and lift loads can then be determined and used to calculate the velocity and displacement of the tube. The grid is then recalculated because of the displacement of the tube and the tube velocity is taken as a new boundary condition for the next time step.

Chen *et al.* (1997) describe a direct-measurement technique for determining the fluid damping and fluid stiffness coefficients that are given in section 1.2.3. Chen *et al.* concluded that fluid-damping-controlled instability is most likely associated with the motion in the lift direction because in many cases $\vec{\alpha}$ is positive while $\vec{\beta}$ is negative (equations 1.9 and 1.10).

Vortex shedding

Vortex shedding is the principal excitation mechanism for flow-induced vibration in cross flow, producing alternating forces, which occur more frequently if the flow

velocity is increased (figure 1.5). Vortex shedding is fluid-mechanical in nature and does not depend on the movement of the tubes.

If the vortex shedding frequency (equation 1.15) and one of the tube's natural frequencies differ by less than 20 percent, 'lock in' may occur. 'Lock in' is a phenomenon whereby the vortex shedding frequency changes to become exactly equal to one of the tube's natural frequencies. The vortex shedding frequency is a function of the Strouhal number (Sr), velocity and the diameter (D_o) of the tubes as shown in equation 1.15

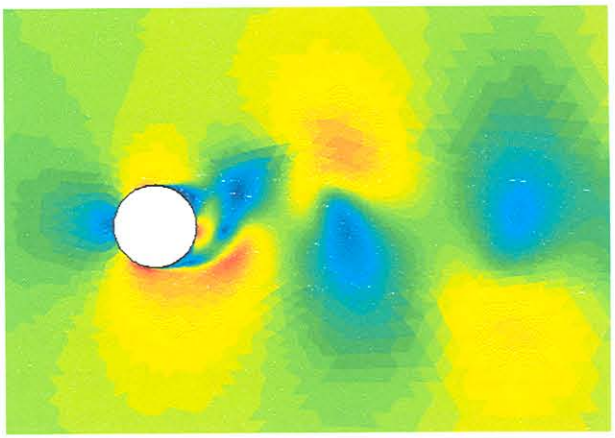

Figure 1.5: Vortex shedding: Single cylinder in cross flow

$$f_{vs} = \frac{S_r u}{D_o} \qquad 1.15$$

Studies showed that the Strouhal numbers in tube arrays are functions of Reynolds number and that there are multiple Strouhal numbers at a given Reynolds number. Chen (1968) and Fitz-Hugh (1973) developed Strouhal number correlations. These correlations contain some inconsistencies. Oengören and Ziada (1997) showed that Strouhal number data grouped mainly around different Strouhal number lines (see figure 1.6). Xp is the tube pitch to diameter ratio.

Vortex shedding forces in liquids are usually sufficiently large (if the natural frequency of tubes is close to the vortex shedding frequency) to produce tube vibration. In gases, vortex shedding is only important if the tube damping is small or the gas has a high density or large velocity (Chen, 1992).

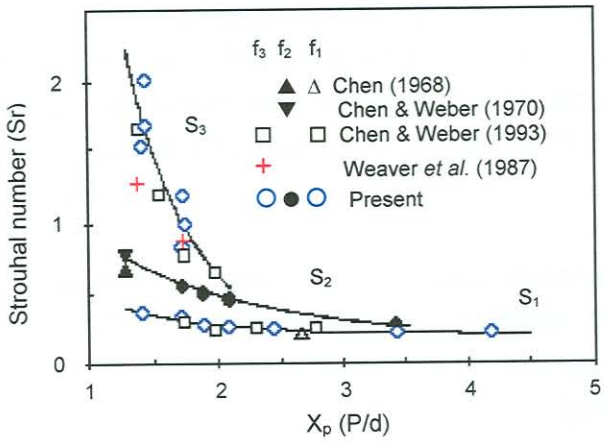

Figure 1.6: Strouhal number chart (Oengören and Ziada, 1997).

Acoustic resonance

Acoustic vibration only occurs when the shell-side fluid is a vapour or a gas. Two types of frequencies can be associated with acoustic vibration: Acoustic frequency (f_a) of the heat exchanger and the acoustic wake-shedding frequency of the tube bundles (f_s). When these two frequencies coincide, acoustic resonance can occur. Acoustic resonance can only lead to vessel and vessel support damage if this resonance frequency matches the natural frequency of the tubes. HTFS suggests the following criteria:

For a cylindrical geometry, if the frequency ratio is within 20 percent (equation 1.16)

$$0.8 < \frac{f_a}{f_s} < 1.2 \qquad 1.16$$

then acoustic resonance may be generated (where f_a is the acoustic frequency and f_s is the acoustic wake-shedding frequency).

If acoustic resonance 'lock in' occurs and if the natural frequency is within 20 percent of the shedding frequency (eq. 1.17)

$$0.8 < \frac{f_n}{f_s} < 1.2 \qquad 1.17$$

then tube vibration may occur (where f_n is the fundamental frequency of the tube). HTFS (1992) gives a more detailed discussion on how to determine the frequencies described above. The problem is that the speed of sound and the acoustic Strouhal number, which are used in these calculations, are difficult to obtain. Strouhal number maps can be used, but the errors may be in the order of 25 percent (HTFS, 1992).

Oengören and Ziada (1997) investigated acoustic resonance in triangular tube bundles and developed an acoustic Strouhal number chart. This chart was developed using measurements obtained in wind tunnel tests, as well as data from the literature (see figure 1.7). Their study further showed that the mechanism of acoustic resonance in parallel triangle arrays are similar to that of in-line arrays because of the similar free flow lanes between the tubes through which the flow proceed.

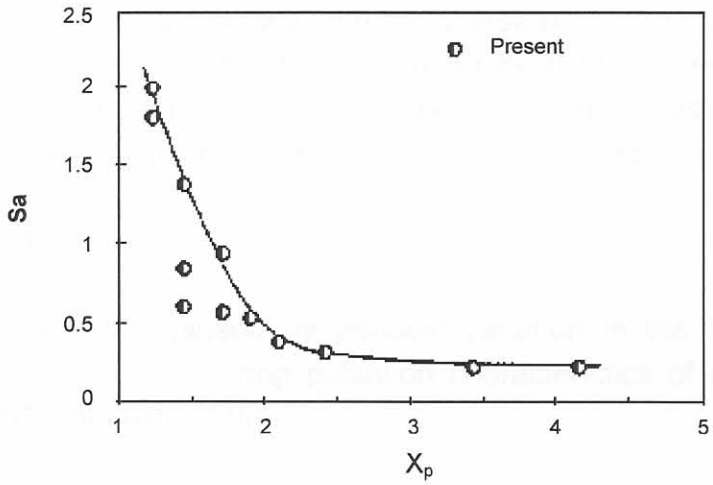

Figure 1.7: Acoustic Strouhal number chart (Oengören and Ziada).
(S_a-acoustic Strouhal number, X_p-tube pitch)

Turbulence buffeting

Turbulent flow contains a wide spectrum of frequencies distributed around a central dominant frequency (see figure 1.8). This frequency increases as the cross flow velocity increases.

Energy dissipation in turbulent flow occurs both because of molecular viscosity and 'turbulent viscosity'. The tube responds easily to an oscillation force at one of its natural frequencies. Chenoweth (1998) gives the following equation (equation 1.18) for determining the turbulent buffeting frequency (f_{tb}):

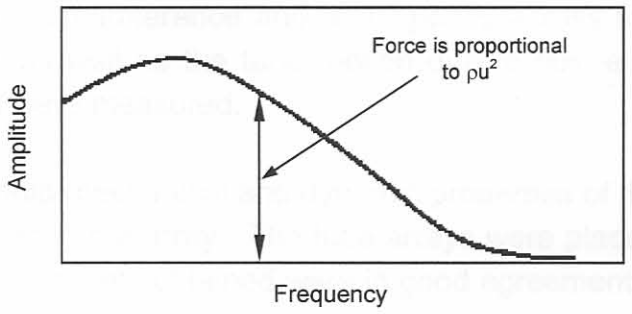

Figure 1.8: Frequency spectrum of the excitation force (HTFS)

$$f_{tb} = \frac{u_c D_o}{p_l p_t}\left[3.05\left(1-\frac{D_o}{p_t}\right)^2 + 0.28\right] \qquad 1.18$$

where p_l and p_t are the longitudinal and transverse pitch of the tube bundle. This equation can only be applied when the shell side fluid is gaseous. The forces associated with turbulent buffeting can be obtained by using fluid structure interaction programs. This process is very time consuming.

Flow pulsation

Tube vibration can be caused by periodic variation in the flow, for example reciprocating machines or strong pulsation characteristics of certain two-phase flow patterns (Chenoweth, 1998).

Parallel-flow eddy formation

Eddies developing along the tube due to parallel-flow can cause vibration. Nuclear reactors and associated heat exchangers have experienced this type of vibration. They typically have very high axial velocities and long unsupported tube spans. Vibration occurs when the velocity reaches a critical value. Methods for determining the critical value are described by Chen and Weber (1970) and Kawamura *et al.* (1997).

1.2.5 Measurements and testing

Romberg and Popp (1997) used a pressure test tube (figure 1.9) to determine the forces acting on a single tube in a bundle subjected to cross-flow random

excitation. The tube provided non-stationary pressure distribution simultaneously at 30 points on the circumference and at 15 points across the tube span. The acting fluid forces as well as the tube motion due to fluid-elastic instability and turbulent buffeting were measured.

The geometrical, fluid-mechanical and dynamic properties of the test tube are the same as other tubes in the array. The tube arrays were placed in a wind tunnel. Some of the measurements obtained were in good agreement with the calculated values.

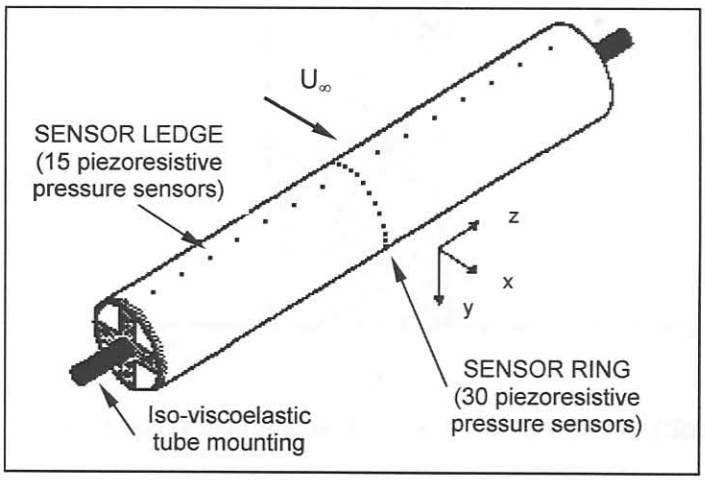

Figure 1.9: Test tube (Romberg and Popp, 1997)

Soper (1980) measured the amplitude of selected tubes (see figure 1.10) using resistance strain gauges bonded to the tube at the maximum bending strain position. These tests were done for four tube configurations. The tests showed that the rotated triangular configuration was the most prone to fluid elastic instability, while the rotated square geometry exhibited the greatest resistance. Intense acoustic standing waves were present in the rotated square geometry, making them unsuitable for applications with gas as a shell-side fluid.

Oengören and Ziada (1997) measured sound pressure levels by condenser microphones located in the tube bundle, subjected to a wind tunnel test. Inada *et al.* (1997) determined the motion-dependent fluid forces by using a tube excitation mechanism and measuring the response of the surrounding tubes.

Hartlen and Anderson (1980) used pre-operational vibration measurements to determine whether or not flow-induced vibration will occur. The tests were conducted with the tubesheet exposed for probe access. A microphone-in-tube technique was used to determine a zone of impacting along with a bi-axial accelerometer probe, which identified the tubes with the highest levels of impacting-accelerations at the baffle and mid-span locations. The vibratory displacement as a function of position, was also measured using the probe.

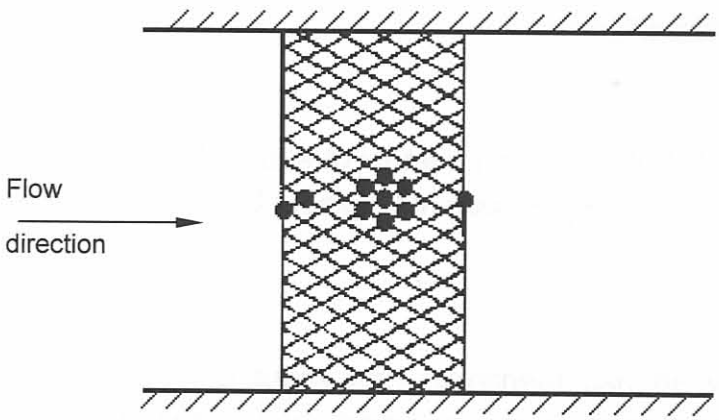

Figure 1.10: Position of instrumented tubes in the tube bundle (Soper, 1980).

1.2.6 Failure and wear

Failure and/or wear in heat exchangers can be caused by:

- Vibration
- Thermal expansion
- Environmental effects

Vibration failure

Mechanical failure of tubes is usually the result of one of the following (as discussed in HEDH (1998)):

a) Collision damage

When the amplitude of vibration is sufficiently large, adjacent tubes collide with one another or with the shell. Collision damage produces a diamond-shape wear

pattern (usually in the mid-span between baffles) where the tube wears thin and eventually splits open.

b) Baffle damage

Baffle hole clearances as given by TEMA, are used to facilitate exchanger bundle assembly. The tubes are therefore not rigidly fixed but can move relative to the baffle. The movement wears the vibrating tubes thin, particularly when the baffles are thin and made of a harder material than the tube.

c) Fatigue

Repeated bending of the tubes due to vibration can lead to failure if the stresses are high enough. Corrosion and erosion can accelerate this process.

d) Tube joint leakage

The tube joints between the tubes and tubesheet can be welded or rolled, causing stress concentrations where the tubes emerge from the tubesheet. Flow-induced vibration may cause leakage between the joints, particularly in fixed shell-and-tube designs where thermal stresses are also induced in the joints.

Thermal expansion

In fixed tubesheet exchangers the tubes are restrained from free thermal expansion. These exchangers are designed so that no expansion joints are needed at normal operating conditions. Problems most often occur during startup, shutdown or some process upset. Floating-head exchangers are not inherently immune to differential expansion problems. In multiple tube passes the temperature difference between adjacent tube passes can cause destructive stresses.

Environmental effects

Corrosion, erosion and fretting reduce the thickness of the tube material. It is therefore necessary to design heat exchangers with a corrosion allowance. Raj *et al.* (1999) examined two cases where corrosion caused failure in heat exchangers.

1.2.7 Case studies

Literature

Hartlen and Anderson (1980) examined heat exchanger failures in a large electricity generating utility, over a period of ten years. The initial failures appear over a widely varying time scale from commissioning up to 15 years of service. In most cases the same failure recurred within a few years. Four cases showed that the failure was caused by fatigue due to high velocities at inlet or outlet regions. In seven cases baffle damage occurred because of acoustic vibration, flow pulsation and maldistribution of shell-side flow. One case of collision damage, corrosion failure and faulty manufacturing occurred. Hartlen and Anderson also describe a pre-operational vibration test that provide commissioning and maintenance information.

Escoe (1997) studied an inadequate flow-induced vibration design of a steam condenser. The condenser exchanger experienced both fluid-elastic instability and turbulence buffeting. The first failure occurred within six months of operation caused by FEI. After fixing this problem, the exchanger failed (tube-to-tube collision) due to low cycle fatigue after 12 years when the shell-side velocity was increased. The exchanger was replaced by a RODbaffle exchanger.

Frick (1997) introduced an empirical Wear Projection Technology (WPT) which relies on data from two or more time independent wear related measurements at a wear site. The WPT method is independent of the wear mechanism and the assessment of ongoing wear is based on projection using constant volume-wear-rate assumptions. The fretting wear damage of an exchanger is proportional to the work-rate (dynamic interaction between the vibrating tube and its supports). Yetiser *et al.* (1997) derived an estimated work-rate formula to predict fretting wear, using turbulence as excitation only. Rao *et al.* (1997) suggested a wear methodology to predict tube wear at scheduled inspections by determining a set of wear parameters from a non-linear finite element simulation, using both FEI and flow induced turbulence as excitation mechanisms. In most operating conditions the range of values for these parameters can vary to quite an extent, therefore deterministic methods were developed to determine the work-rate (Sauvé *et al.*, 1997).

Heat exchangers at Sasol

The heat exchanger that was selected, analysed and measured in Chapters 2, 3, and 4 was from Sasol Synthetic Fuels (SSF). It was therefore also necessary to obtain vibration and failure information from SSF. Four case studies were received from SSF and in all four cases the heat exchangers were TEMA class R.

- 1st Stage raw gas exchanger (12 ES 101)
- Circulating methanol cooler (212 ES 106)
- Main wash methanol cooler (212 ES 158)
- CEU 1000/5600 Horizontal type exchanger (ES 103)

a) 1st Stage raw gas exchanger (12 ES 101)

The raw gas exchanger is a BEM type exchanger with pure gas as shell-side fluid and raw gas as tube-side fluid. A vibration analysis was done to determine whether the shell-side fluid velocity could be increased. Although the analyses from LURGI and SASTECH differed in some respects, the general conclusion was that the probability of acoustic resonance was very high. It was therefore suggested that the exchanger should not be operated at increased flow.

b) Circulating methanol cooler (212 ES 106)

The exchanger is classified as an AKL (tube length 10360 mm) fixed tubesheet exchanger with 2 tube passes, with refrigerant as shell side fluid and loaded methanol as tube side fluid. A vibration analysis with increased load on the shell side was done by LURGI, concluding that there was no risk of acoustic vibration and that vortex shedding was unlikely to occur. LURGI further suggested that the number of baffles be increased from 6 to 7 to shorten the unsupported tube length. Since major repairs would have had to be done to access the bundle, Sasol increased the load without increasing the number of baffles. Vibration measurement on the exchanger was done while operating at higher load which indicated possible vibration of the tubes. The vibration, however, decreased with increased load.

c) Main wash methanol cooler (212 ES 158)

The main wash methanol cooler is also an AKL fixed tubesheet exchanger, with a tube length of 9145 mm. At increased loads, a vibration analysis showed a center vortex shedding ratio of 1.415, which was outside the HTFS range. The

concern was that the shedding frequency passed through the natural tube frequency and that the vibration was not damped out at 1.4 times the natural frequency. Vibration measurements were taken at the increased load condition, without any modifications made to the exchangers and the results were satisfactory.

d) CEU 1000/5600 Horizontal type exchanger (ES 103)

This single pass U-tube exchanger with a rotated square tube array was analysed with increased shell-side flow, using HTFS. The analysis predicted turbulence buffeting and vortex shedding. As rotated square arrays are prone to acoustic resonance, an alternative layout was recommended. The design was changed from having 10 double segmental baffles (21 percent cut) to 6 single segmental (15 percent cut) baffles. This could easily be done, because the exchanger had a floating head tubesheet.

1.3 Scope of the work

The problem of flow-induced vibration in shell-and-tube heat exchangers can be divided into two parts. Firstly, will vibration occur at the increased flow rate? And secondly, will that vibration be sufficiently large to cause failure? The literature study gives an overview of both these problems. Only the first question will be addressed in this research. It is after all more important to first determine whether vibration will occur at increased capacity. Once this question is answered, the amplitude of the vibration and the associated failure modes can be addressed. This second part is therefore not included in the scope of this research.

In the literature study (paragraph 1.2.4) the different mechanisms associated with flow-induced vibration and the corresponding margins of uncertainty, were described. The HTFS software that is used by SASOL, makes use of a 20 percent margin of uncertainty. If a vibration calculation is done on a heat exchanger and the results indicate that the frequencies are just within the 20 percent uncertainty range, does the heat exchanger need to be replaced or are there other methods to determine if vibration will actually occur? The fluid-elastic instability, vortex shedding and turbulence buffeting frequencies are all functions of the flow velocity through the heat exchanger. The margins of uncertainty can therefore be reduced if a more accurate prediction of the flow velocity through the heat exchanger can be obtained. One such method is using a CFD analysis to simulate the flow patterns. CFD analyses are expensive and methods for

reducing the number of analyses are also investigated. This, however, is of no use if the natural frequencies of the tubes are not accurately predicted. The natural frequencies of the tubes (paragraph 1.2.2) can vary with as much as 40 percent, depending on the axial forces in the tube. Additional measurements to determine the natural frequencies of the tubes are also needed.

The objective of this research is to verify existing flow-induced vibration prediction methods by using CFD analyses and experimental work and to obtain a more accurate prediction of flow-induced vibration when the heat exchangers is within the uncertainty range to determine if the heat exchanger life can be extended .

1.4 Research Methodology

To combine the methods for the prediction of flow-induced vibration, the following steps were taken as shown in figure 1.11.

First a HTRI or HTFS analysis on the heat exchanger is performed. If the vibration frequencies obtained from the analysis are within the 20 percent uncertainty range, CFD analyses and experimental vibration measurement are required. The HTRI calculated frequency is then compared to the experimentally measured frequency where vibration in the heat exchanger occurred. The measured velocities at which vibration occurred in the heat exchanger, are also compared to the HTRI and CFD predicted values. If the mass flow rate falls within the predicted frequency range where vibration will occur, additional methods such as fluid structure analyses are required. If the increased mass flow rate falls outside the frequency range, the heat exchanger can be operated successfully at increased mass flow rates.

1.5 Layout

In Chapter 2 a heat exchanger at SSF is selected that complied with the specified criteria. The flow rates at which vibration problems are likely to occur, are determined using HTRI software. FEM analyses are also performed to confirm the natural frequencies, as calculated by the HTRI analyses. Additional higher natural frequencies are also obtained from this process. The flow through the heat exchanger is analysed in Chapter 3 using Computational Fluid Dynamics

simulations (CFD). From these analyses the average cross-flow velocities and pressure drop through the selected heat exchanger are obtained.

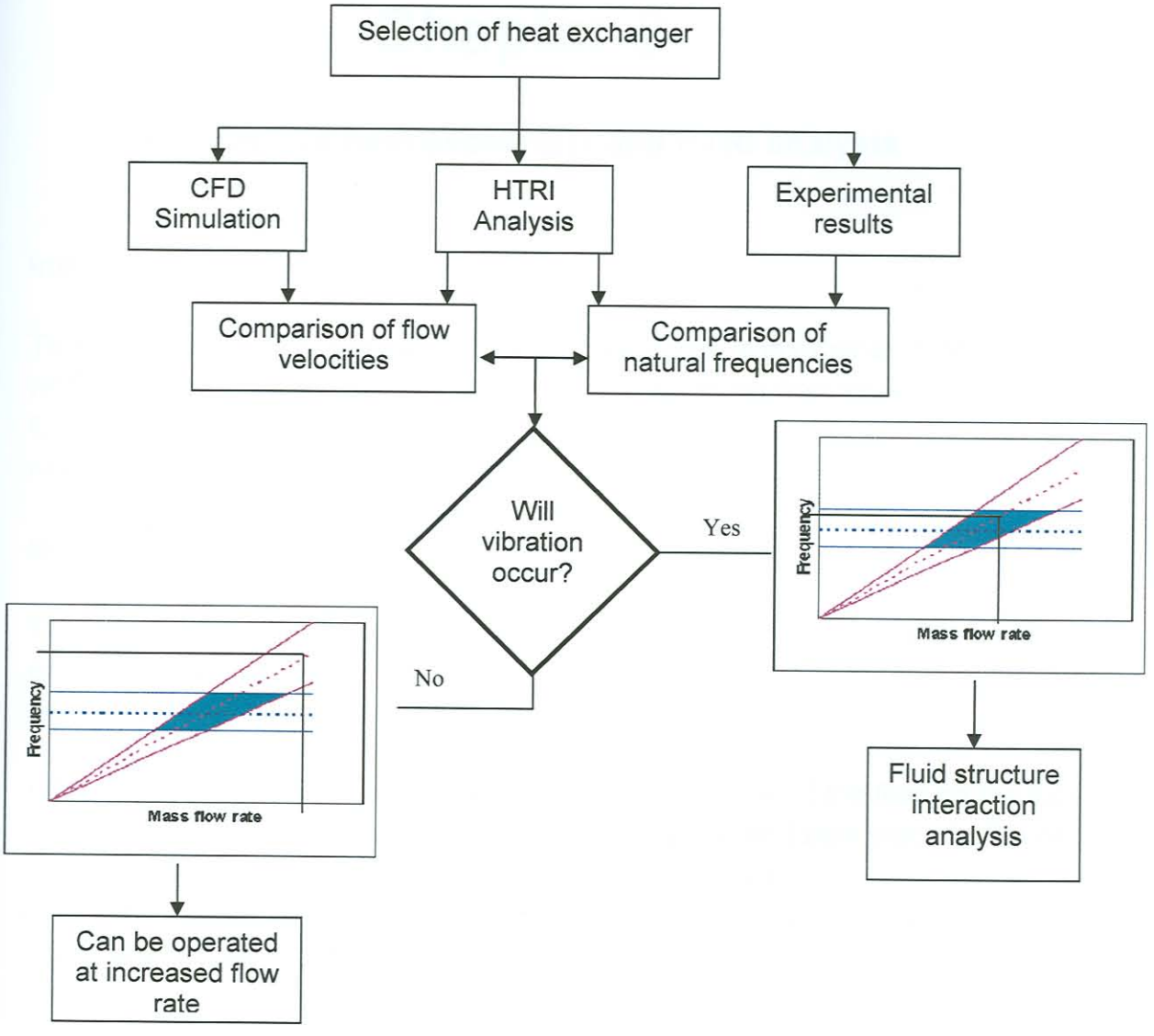

Figure 1.11: Research methodology diagram

Vibration measurements on the selected exchanger at normal loads and at increased loads were taken. The measuring procedure and experimental results are given in Chapter 4. In Chapter 5 the HTRI results, CFD results and experimental results are compared. The margins of uncertainty in the predicted values are also described. Chapter 6 contains the conclusion and recommendations from the research study.

Chapter 2

Selection of heat exchanger and HTRI analysis

2.1 Introduction

To determine at which flow rates vibration may occur, a number of HTRI analyses were done on the selected heat exchanger. The natural frequency equation from Chapter 1 (eq. 1.1), as well as FEM analyses, were used to determine additional natural frequencies of the tube.

2.2 Selection criteria

To select a heat exchanger from the approximately 2000 shell-and-tube heat exchangers at Sasol Synthetic Fuels (SSF), the following criteria were used to select a suitable heat exchanger to analyse.

- The shell- and tube-side flow must be single-phase flow. If the fluid on the tube- or shell-side is a gas and condensation or evaporation takes place in the heat exchanger, solving the problem becomes more complex.
- The shell-side fluid must be a gas with temperature not exceeding 100°C. The temperature range of equipment available to measure vibration on the heat exchanger is limited. If shell-side flow is a gas, all six mechanisms that can cause tube vibration (see paragraph 1.2.4) are present. Acoustic resonance only occurs if the fluid is a gas or vapour.
- The heat exchanger should not be covered with thermal insulation. For the experimental investigation, free access to the shell was needed for accelerometers and strain gauges.
- It must be possible to vary the load through the heat exchanger. Vibration measurements at different load conditions need to be taken to compare these values with predicted values.
- The flow rates, operating pressure and temperature at the inlet and outlet, should be known. The flow rate, pressure and temperature through the heat exchanger changes, depending on the process. When comparing the results, it is important to compare results with the same flow velocities, temperatures and

pressures. It is furthermore important to measure the flow velocities to see if the inlet flow velocity changes are causing any vibration in the heat exchanger.

The heat exchanger should also have a history of vibration-related problems. From the list of possible heat exchangers provided by SSF, the following two exchangers were examined in more detail:

- ES X06 Trim cooler
- ES 208 Tail gas heat exchanger

2.2.1 ES X06 Trim cooler

The ES X06 heat exchanger was a good candidate for vibration measurements, because it had serious vibration problems. The gas that passes through the shell-side of the heat exchanger consists of 224 components, which can be divided into three categories: Tail gas, reaction water and unstabilised light oil. Condensation of some of these components takes place, making this a two-phase problem. The heat exchanger also had unconventional baffles that could not be analysed with Heat Transfer Research Institute (HTRI) or Heat Transfer and Fluid flow Service (HTFS). The ES 208 Tail gas heat exchanger was therefore analysed, for it did not pose any such problems.

2.2.2 ES 208 Tail gas shell-and-tube heat exchanger

The heat exchanger is a CEN 1020-6100 type (figure 2.1) shell-and-tube heat exchanger with a square tube configuration and triple segmental baffles. A HTRI analysis was used to obtain vibration information because of its triple segmental baffle capabilities (figure 2.2).

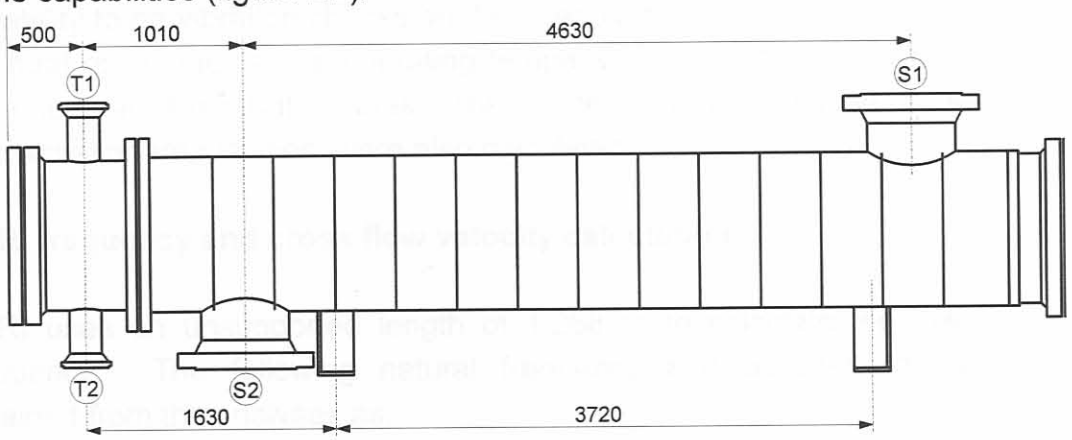

Figure 2.1: CEN type heat exchanger

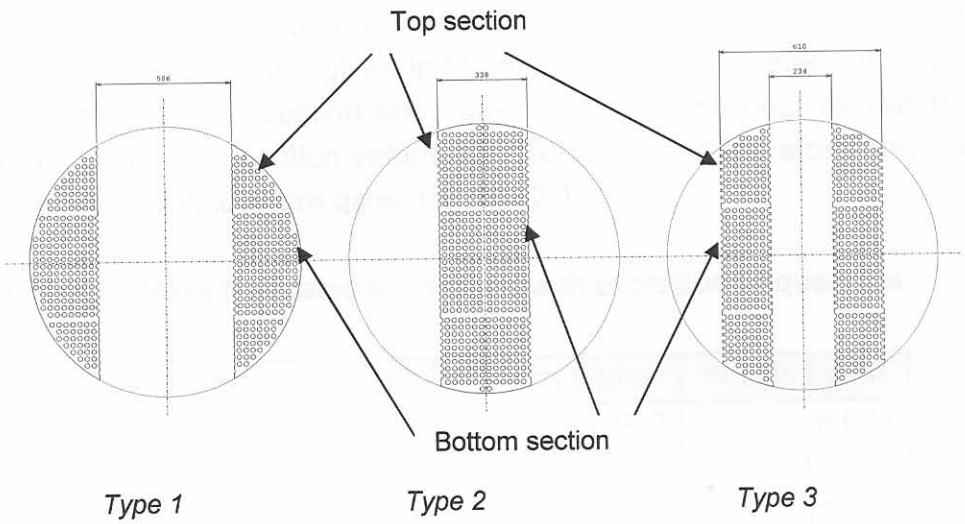

Figure 2.2: Triple segmental baffles

The heat exchanger has one shell-side pass with an inside diameter of 1.02m and six tube-side passes with 1100 tubes each 6.1m long with an outside diameter of 19mm. Tail gas with a density of *21 kg/m*^{3} (Appendix A) enters the shell-side of the heat exchanger at S1 (see figure 2.1) with a temperature of 55°C and exits the heat exchanger at S2 with a temperature of 47°C. On the tube-side, water enters the heat exchanger at T1 with a temperature of 30°C and exits at T2 after six tube passes with a temperature of 43°C. The operating pressure on the shell-side of the heat exchanger is 3.225 MPa and 0.35 MPa on the tube-side.

2.3 HTRI Analysis

The HTRI software is mainly used to design heat exchangers, but it also has the capability to do vibration checks on the heat exchanger tubes. HTRI analyses on the heat exchanger at the operating temperature and pressure, were performed for a number of mass flow rates. The temperature and pressure dependence of the excitation frequencies, were also calculated.

2.3.1 HTRI frequency and cross flow velocity calculation

HTRI uses an unsupported length of 1.268 m to calculate the lowest natural frequency. The following natural frequency and acoustic frequency were obtained from the analyses as:

$$f_n = 28.58Hz$$
$$f_a = 174.75Hz \qquad 2.1$$

The mass flow rates at which the excitation frequencies equal the natural frequencies of the tubes, are given in table 2.1. HTRI calculated these values at the inlet section, middle section and outlet section of the heat exchanger. The inlet section and outlet section values are the same and therefore only the inlet- and middle section values are given in table 2.1.

Table 2.1: Mass flow rates associated with excitation frequencies.

Mass flow rate associated with:	Inlet (kg/s)	Middle (kg/s)
Vortex shedding (f_{vs})	7.950	8.004
Turbulence buffeting (f_{tb})	9.982	10.054
Acoustic vortex shedding (f_{vsa})	46.713	47.073
Acoustic turbulence buffeting (f_{tba})	66.134	66.601

The acoustic frequency of the heat exchanger is not within a range of 20 percent of the natural frequency of the tubes. This means that no tube vibration due to acoustic excitation, will take place. For this reason only the vortex shedding frequency and turbulence buffeting frequency will be looked at in more detail.

The maximum vibration amplitude of the tubes, as calculated by the HTRI analyses for a mass flow range between 5 kg/s and 100 kg/s, is 0.3 mm. Figure 2.3 a) shows the amplitude of vibration for the inlet section (blue) and outlet section (red) as functions of the mass flow rate.

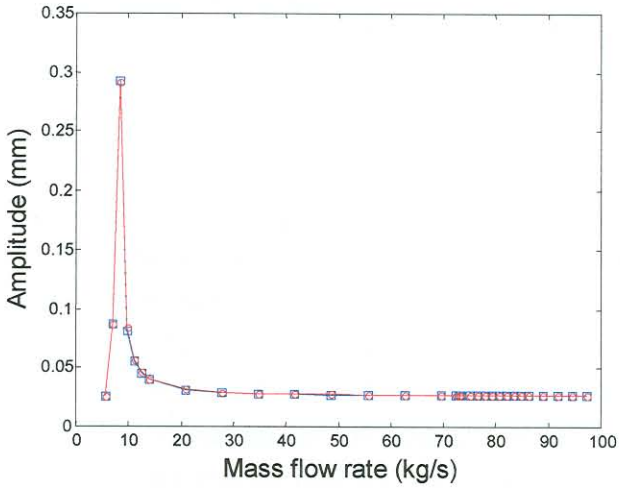

Figure 2.3 a): Vibration amplitude.
(blue – inlet section, red – outlet section)

The vibration amplitude is relatively small and no collision damage will occur because the minimum clearance between adjacent tubes is 7 mm. The vibration may cause fatigue and baffle damage (refer to paragraph 1.2.6) as well as tube sheet damage, especially if there are thermal stresses involved.

In the close-up view of the vibration amplitude graph (figure 2.3 b), the maximum amplitude is at the mass flow rate where the vortex shedding frequency coincides with the tube's natural frequency.

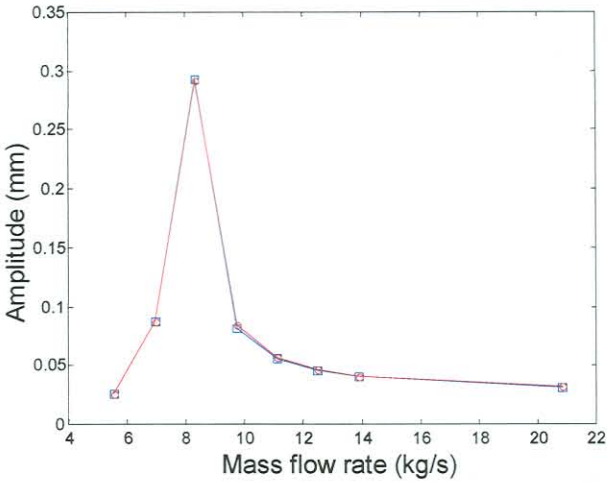

Figure 2.3 b): Close-up view of vibration amplitude.
(blue – inlet section, red – outlet section)

At a mass flow rate of about 14.234 kg/s the HTRI average cross flow velocity is equal to the HTRI calculated fluid-elastic instability critical velocity.

$$c_r = 2.89 m/s \qquad 2.2$$

No vibration amplitude calculation is given for fluid-elastic instability, but the tube vibration is assumed to increase as the cross flow velocity increases beyond the critical value, until the neighbouring tubes limit the amplitude, causing collision damage (refer to figure 1.3). If the fluid-elastic instability vibration curve published by HTFS is superimposed on to the vibration curve given by the HTRI analysis, (figure 2.3), the vibration amplitude curve shown in figure 2.4 is obtained. It is important to remember that the assumption is made that the entire unsupported tube length is subjected to the single average cross flow velocity. This is hardly ever the case in shell-and-tube heat exchangers, as the average

cross flow velocity is also a function of the flow patterns through the heat exchanger, as caused by the baffle plates.

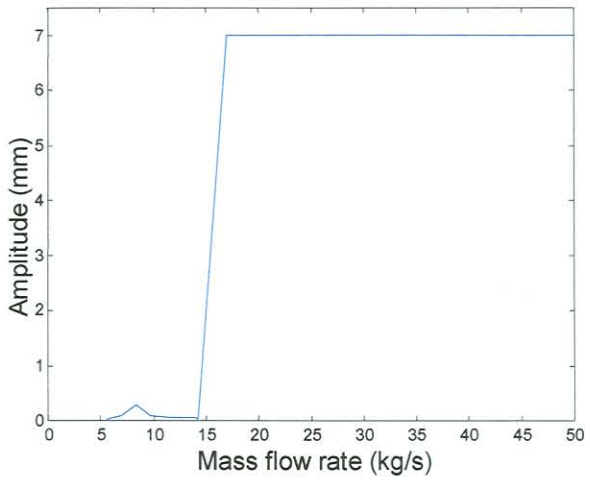

Figure 2.4: Vibration curve including FEI

2.3.2 Pressure and temperature dependence

The pressure and temperature dependence of the excitation frequencies, were obtained at a mass flow rate of 73 kg/s. Figures 2.5 and 2.6 give the inlet temperature dependence of the vortex shedding and turbulence buffeting frequencies respectively. These two frequencies are not functions of the inlet pressure. The acoustic vortex shedding and turbulence buffeting frequency on the other hand are only dependent on the inlet pressure and not the temperature.

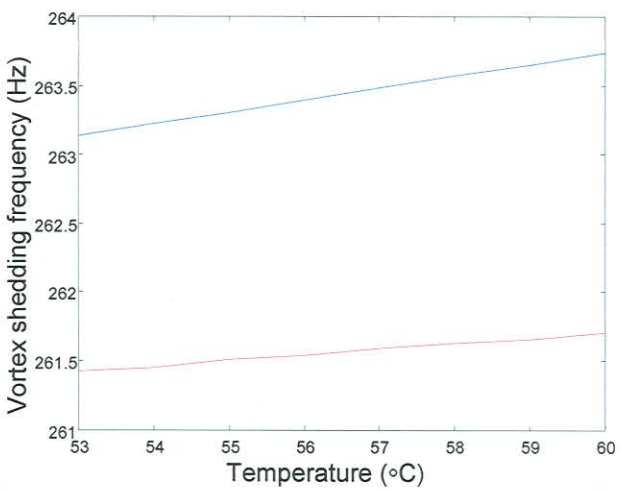

Figure 2.5: Temperature dependence of the vortex shedding frequency (blue – inlet section, red – middle section)

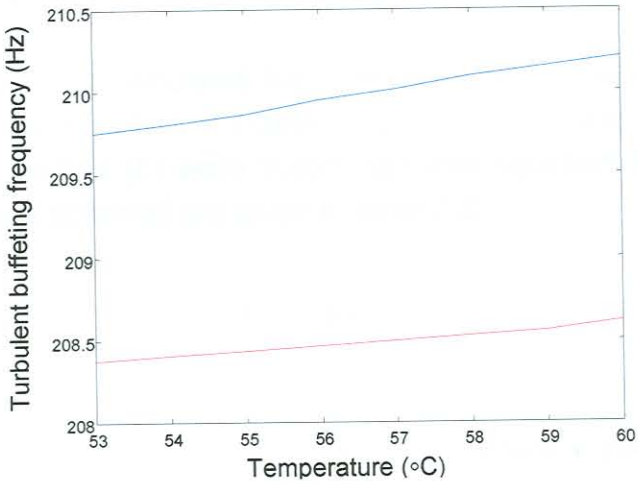

Figure 2.6: Temperature dependence of the turbulence buffeting frequency (blue – inlet section, red – middle section)

The difference in vortex shedding and turbulence buffeting frequency over the given temperature range, is less than 0.4 percent and can therefore be neglected when working in the specified temperature range.

2.3.3 Pressure drop through the heat exchanger

The HTRI-calculated pressure drop through the heat exchanger, is given in figure 2.7 for a range of mass flow rates. These values will be compared with CFD results (Chapter 3) to obtain the mass flow rates through the heat exchanger for measuring purposes (Chapter 4).

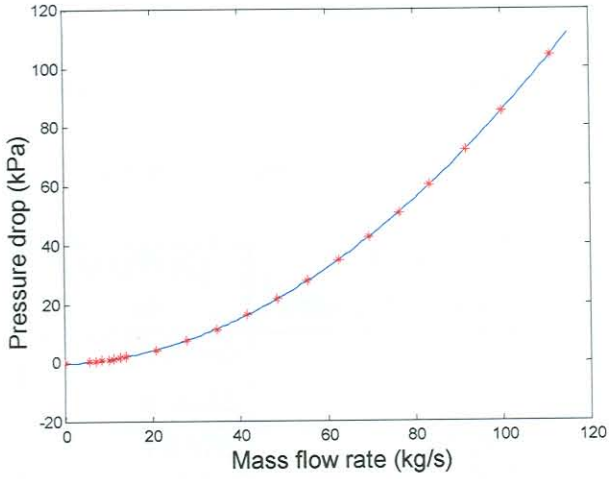

Figure 2.7: HTRI calculated pressure drop through the heat exchanger

2.4 Additional natural frequency calculations

The HTRI analysis only calculated the lowest natural frequency. To obtain all the natural frequencies, equation 1.1 (repeated as eq. 2.3) was used. The different combinations of lengths (L) were substituted into equation 2.3 and the different natural frequencies obtained are given in table 2.2.

$$f_n = \frac{C_n}{2\pi}\left(\frac{EI}{M_e L^4}\right)^{0.5} \qquad 2.3$$

C_n = 10 from figure 1.1 and E = 210 GPa. The moment of inertia (eq. 2.4) and the equivalent mass (eq. 2.5) were calculated as follows:

$$I = \frac{\pi\left(D_o^4 - D_i^4\right)}{64} = 3.415\times10^{-9} \qquad 2.4$$

$$M_e = M_m + M_t + M_s = 0.916 kg/m \qquad 2.5$$

The equivalent mass per unit length (M_e) is the sum of the fluid inside the tube per unit length (M_t), the tube material per unit length (M_m) and the virtual mass per unit length (M_s) of the tube for shell-side fluid displaced by the tube (equation 2.6).

$$M_s = \frac{k\rho_s \pi D_o^2}{4} = 1.393\times10^{-2}\, kg/m \qquad 2.6$$

The added mass coefficient (k) is a function of the tube pitch to diameter ratio as well as the tube layout as given by the TEMA standards (1988).

Table 2.2: Natural frequencies of unsupported tube lengths

Length (L) (m)	Natural frequency (Hz)
0.8450	62.45
0.8635	59.80*
1.2675	27.76
1.2860	26.96*

* Value calculated using equation 2.3 with assumption that both ends of the tube are pinned.

If the above-calculated natural frequency for an unsupported length of 1.2675 m is compared to the value given by the HTRI analyses, it differs by 0.82 Hz or 3 percent. This is due to variations in added mass and natural frequency coefficients.

This is not the longest unsupported length. There are a small number of tubes that have an unsupported length of 1.286 m at the inlet and outlet section of the heat exchanger, because of the 0.441 m spacing between the tubesheet and baffles.

The natural frequency calculation in table 2.2 was done using equation 2.3. This equation was formulated with the assumption that the tube ends are pinned at the baffle plates. At the tubesheets this is not the case and the natural frequencies need to be calculated using fixed constraints at the one end (tubesheet) and pinned constraints at the other end (baffle plate).

A Finite Element Method Analysis (FEA) was used to determine the mode shapes and natural frequencies with pinned-pinned and fixed-pinned supports for the four different tube lengths.

In all the FEA's an equivalent density was used to compensate for the tube-side fluid mass and virtual shell-side fluid mass.

Figure 2.7 shows a tube between baffle plates and this was analysed using pinned supports at both ends. It represents the mode shape of the first natural frequency (61.64 Hz) of the tube. This value compares well to the TEMA calculated value (62.45 Hz) in table 2.2.

Figure 2.7: Mode shape of tube with length 0.845 m

In figure 2.8 a) the natural frequency associated with pinned supports is 59.023 Hz which is very close to the TEMA calculated value (59.8 Hz) in table 2.2.

This frequency is inaccurate because of the assumption of pinned-pinned supports mentioned earlier. If the tube is analysed with the correct constraints (fixed-pinned) as shown in figure 2.8 b) a natural frequency of 92.21 Hz is obtained.

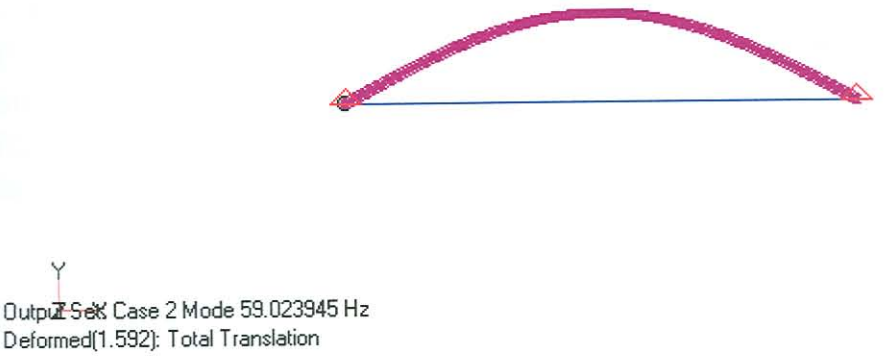

Figure 2.8 a) Mode shape of tube with length 0.8635 m with pinned supports

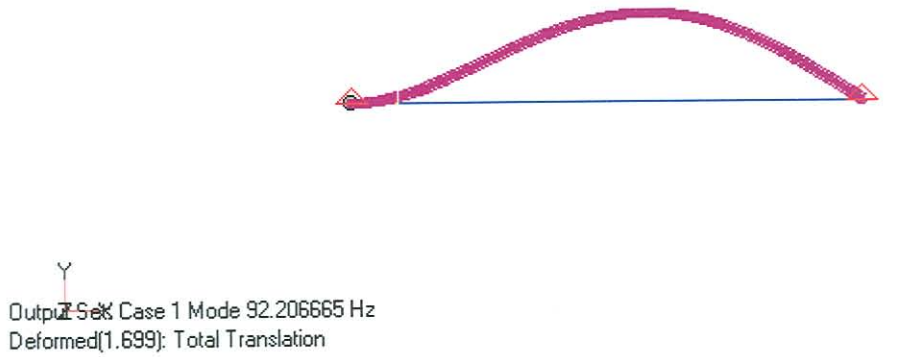

Figure 2.8 b) Mode shape of tube with length 0.8635 m with fixed-pinned supports

For the tube section in figure 2.9, the tube is again between two baffle plates and the assumption used to calculate the natural frequency holds. The natural frequency given by TEMA is 27.76 Hz which compares well with the FEA value of 27.39 Hz.

Figure 2.9: Mode shape of tube with length 1.2675 m with pinned supports

Figures 2.10 a) and b) give the mode shapes for pinned-pinned and fixed-pinned supports respectively. In the actual heat exchanger, the one end of the tube is fixed at the tubesheet and the associated natural frequency that should be used, is 41.57 Hz.

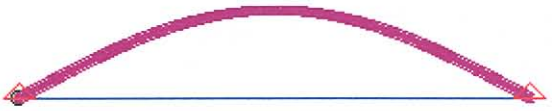

Figure 2.10 a) Mode shape of tube with length 1.286 m with pinned supports

Figure 2.10 b) Mode shape of tube with length 1.286 m with fixed-pinned supports

This implies that the lowest natural frequency calculated by the HTRI analysis, is correct. The problem is that if the heat exchanger is operated at a higher mass flow rate, which would not excite the tubes with an unsupported length of 1.2675 m at its lowest frequency, one of the other tubes (with a different unsupported length) may be excited. With this in mind, the mass flow rate associated with the first mode of excitation of the four different unsupported lengths was obtained (table 2.3). In the case of the 0.8635 m and 1.285 m unsupported lengths, the corrected natural frequencies were used as obtained from the FEA.

Only the first natural frequencies for the four different unsupported lengths were used, because the other natural frequencies were above 100 Hz and the vibration amplitudes related to those frequencies, were assumed to be small relative to the amplitudes of the first natural frequency.

Table 2.3: Mass flow rates associated with tube vibration

		Associated mass flow rate (kg/s)			
Natural frequency		27.76Hz	41.57Hz	59.80Hz	92.21Hz
Vortex shedding frequency	Inlet	7.75	11.61	16.70	25.69
	Middle	7.80	11.75	16.84	25.87
Turbulence buffeting frequency	Inlet	9.78	14.58	20.98	32.2
	Middle	9.85	14.68	21.12	32.42

2.5 Comparison of natural frequencies and associated mass flow rates

In table 2.4 the lowest natural frequency value obtained from TEMA equation (table 2.3) and the finite element analysis are compared to values obtained in the HTRI analyses (equation 2.3) of 28.58 Hz.

Table 2.4: Comparison of natural frequencies to HTRI values

	Frequency	Difference (%)
TEMA	27.76	2.869
FEM	27.39	4.164

In table 2.5, the mass flow rates associated with vortex shedding and turbulence buffeting for the lowest natural frequencies obtain from the TEMA calculation, (table 2.3) are compared to the HTRI calculated value (table 2.1).

Table 2.5: Comparison of mass flow rates

		Associated mass flow rate (kg/s)		
		HTRI	TEMA	% difference
Vortex shedding frequency	Inlet	7.95	7.75	2.52
	Middle	8.00	7.80	2.50
Turbulence buffeting frequency	Inlet	9.98	9.78	2.00
	Middle	10.50	9.85	1.99

There are only small differences between the HTRI and TEMA natural frequencies and associated mass flow rate values as shown in tables 2.4 and 2.5. The difference between the HTRI and TEMA natural frequencies is due to a small difference in the calculation of the effective mass per unit length (M_e) in equation 2.5.

The HTRI results compare well with the TEMA results and can therefore be used for comparison purposes with the CFD results in Chapter 3 as well as the experimental results in Chapter 4.

If the above-calculated natural frequency for an unsupported length of 1.2675 m is compared to the value given by the HTRI analyses, it differs by 0.82 Hz or 3 percent. This is due to variations in added mass and natural frequency coefficients.

This is not the longest unsupported length. There are a small number of tubes that have an unsupported length of 1.286 m at the inlet and outlet section of the heat exchanger, because of the 0.441 m spacing between the tubesheet and baffles.

The natural frequency calculation in table 2.2 was done using equation 2.3. This equation was formulated with the assumption that the tube ends are pinned at the baffle plates. At the tubesheets this is not the case and the natural frequencies need to be calculated using fixed constraints at the one end (tubesheet) and pinned constraints at the other end (baffle plate).

A Finite Element Method Analysis (FEA) was used to determine the mode shapes and natural frequencies with pinned-pinned and fixed-pinned supports for the four different tube lengths.

In all the FEA's an equivalent density was used to compensate for the tube-side fluid mass and virtual shell-side fluid mass.

Figure 2.7 shows a tube between baffle plates and this was analysed using pinned supports at both ends. It represents the mode shape of the first natural frequency (61.64 Hz) of the tube. This value compares well to the TEMA calculated value (62.45 Hz) in table 2.2.

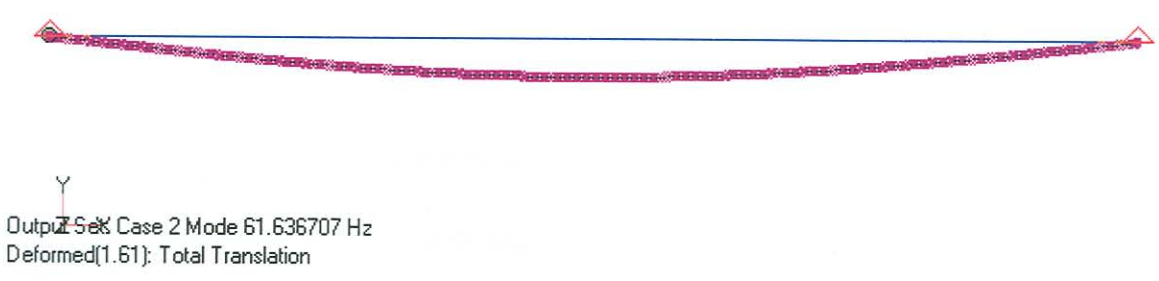

Figure 2.7: Mode shape of tube with length 0.845 m

In figure 2.8 a) the natural frequency associated with pinned supports is 59.023 Hz which is very close to the TEMA calculated value (59.8 Hz) in table 2.2.

This frequency is inaccurate because of the assumption of pinned-pinned supports mentioned earlier. If the tube is analysed with the correct constraints (fixed-pinned) as shown in figure 2.8 b) a natural frequency of 92.21 Hz is obtained.

Figure 2.8 a) Mode shape of tube with length 0.8635 m with pinned supports

Figure 2.8 b) Mode shape of tube with length 0.8635 m with fixed-pinned supports

For the tube section in figure 2.9, the tube is again between two baffle plates and the assumption used to calculate the natural frequency holds. The natural frequency given by TEMA is 27.76 Hz which compares well with the FEA value of 27.39 Hz.

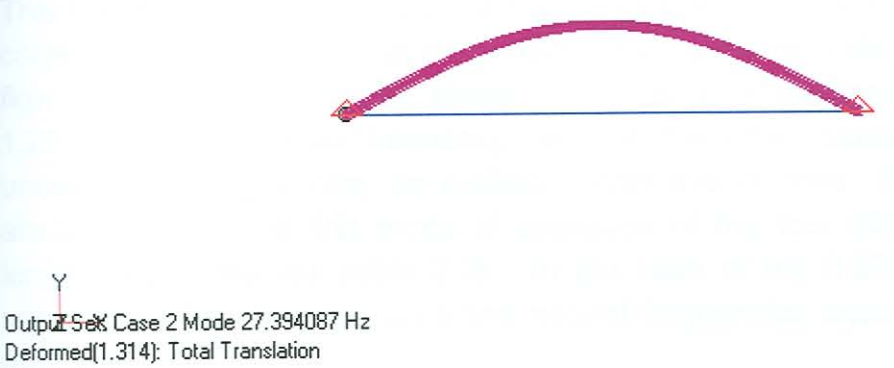

Figure 2.9: Mode shape of tube with length 1.2675 m with pinned supports

Figures 2.10 a) and b) give the mode shapes for pinned-pinned and fixed-pinned supports respectively. In the actual heat exchanger, the one end of the tube is fixed at the tubesheet and the associated natural frequency that should be used, is 41.57 Hz.

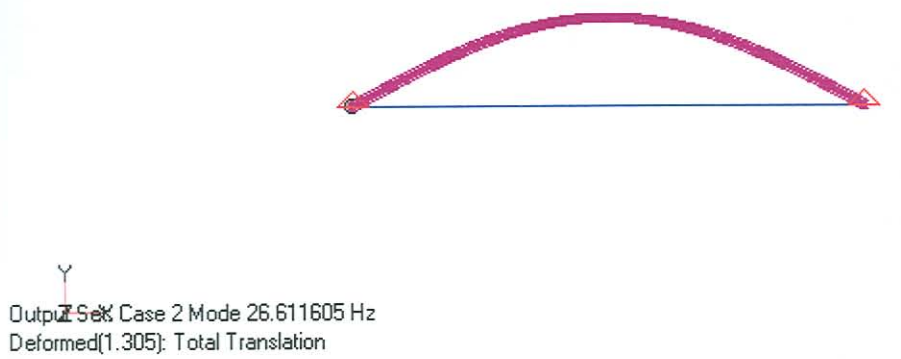

Figure 2.10 a) Mode shape of tube with length 1.286 m with pinned supports

Figure 2.10 b) Mode shape of tube with length 1.286 m with fixed-pinned supports

This implies that the lowest natural frequency calculated by the HTRI analysis, is correct. The problem is that if the heat exchanger is operated at a higher mass flow rate, which would not excite the tubes with an unsupported length of 1.2675 m at its lowest frequency, one of the other tubes (with a different unsupported length) may be excited. With this in mind, the mass flow rate associated with the first mode of excitation of the four different unsupported lengths was obtained (table 2.3). In the case of the 0.8635 m and 1.285 m unsupported lengths, the corrected natural frequencies were used as obtained from the FEA.

Only the first natural frequencies for the four different unsupported lengths were used, because the other natural frequencies were above 100 Hz and the vibration amplitudes related to those frequencies, were assumed to be small relative to the amplitudes of the first natural frequency.

Table 2.3: Mass flow rates associated with tube vibration

		Associated mass flow rate (kg/s)			
Natural frequency		27.76Hz	41.57Hz	59.80Hz	92.21Hz
Vortex shedding frequency	Inlet	7.75	11.61	16.70	25.69
	Middle	7.80	11.75	16.84	25.87
Turbulence buffeting frequency	Inlet	9.78	14.58	20.98	32.2
	Middle	9.85	14.68	21.12	32.42

2.5 Comparison of natural frequencies and associated mass flow rates

In table 2.4 the lowest natural frequency value obtained from TEMA equation (table 2.3) and the finite element analysis are compared to values obtained in the HTRI analyses (equation 2.3) of 28.58 Hz.

Table 2.4: Comparison of natural frequencies to HTRI values

	Frequency	Difference (%)
TEMA	27.76	2.869
FEM	27.39	4.164

In table 2.5, the mass flow rates associated with vortex shedding and turbulence buffeting for the lowest natural frequencies obtain from the TEMA calculation, (table 2.3) are compared to the HTRI calculated value (table 2.1).

Table 2.5: Comparison of mass flow rates

		Associated mass flow rate (kg/s)		
		HTRI	TEMA	% difference
Vortex shedding frequency	Inlet	7.95	7.75	2.52
	Middle	8.00	7.80	2.50
Turbulence buffeting frequency	Inlet	9.98	9.78	2.00
	Middle	10.50	9.85	1.99

There are only small differences between the HTRI and TEMA natural frequencies and associated mass flow rate values as shown in tables 2.4 and 2.5. The difference between the HTRI and TEMA natural frequencies is due to a small difference in the calculation of the effective mass per unit length (M_e) in equation 2.5.

The HTRI results compare well with the TEMA results and can therefore be used for comparison purposes with the CFD results in Chapter 3 as well as the experimental results in Chapter 4.

Chapter 3

Computational fluid dynamics analyses

3.1 Introduction

In this chapter the ES 208 Tail gas heat exchanger that was selected in the previous chapter, is used in a number of Computational Fluid Dynamics (CFD) analyses. The complete heat exchanger could not be simulated, because of a limitation in computational power and therefore only small representative sections of the heat exchanger were analysed. First a repeating section of the middle part of the heat exchanger was analysed and then an equivalent porous model was obtained. The second part was to analyse the inlet section together with the porous model to obtain the necessary boundary conditions for the model. GAMBIT (1999) was used to generate and mesh the models and FLUENT (1999) was used to solve the models.

3.2 CFD analyses: Middle section of heat exchanger

Since the baffle pattern is repeated 4 times, only one of the repeating sections was used to obtain the pressure drop, flow patterns and velocities through the heat exchanger section. The heat exchanger section is symmetric about the x- and y-axes, therefore only a quarter section was simulated (see figure 3.1).

A mesh of 657 104 cells was generated in GAMBIT. This mesh was adapted and solved in FLUENT using a two-equation turbulent energy and dissipation (k-ε) model, using periodic boundaries to satisfy the boundary conditions. A periodic boundary is defined as a boundary where the inlet and outlet velocity distributions are forced to be equal. The magnitude of the velocity, pressure drop and y^+ values were calculated and the mesh was adapted using the maximum y^+ value (for more information refer to Appendix C).

The K-ε turbulence model neglects molecular viscosity and sublayer damping effects, and can only be used in the outer and overlap layers where the log-law

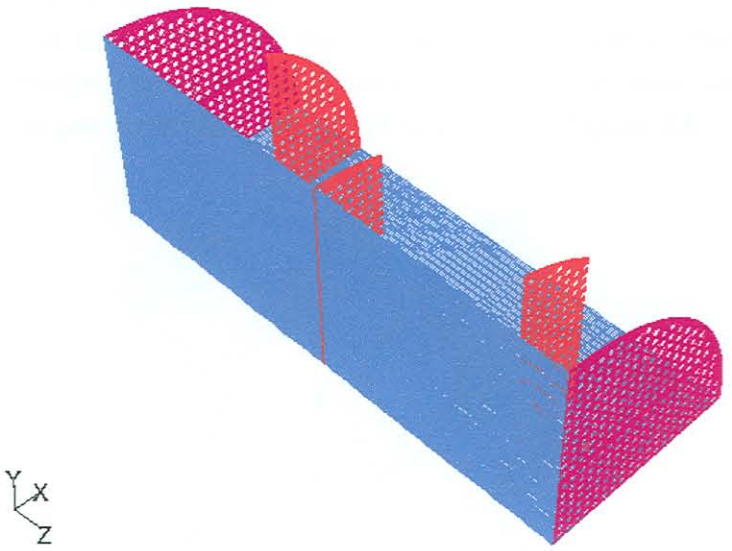

Figure 3.1: Schematic representation of the middle section of the heat exchanger (purple - periodic boundaries, red – baffles and blue – symmetry planes)

holds. The y^+ values on the wall therefore need to be between 35 and 350 according to White (1991) and between 50 and 500 according to FLUENT. The maximum y^+ value for the mesh that was used (1 193 906 cells) was 1 882, which is outside the acceptable region. However, very few cells exceeded a y^+ value of 500 and they were localised at the baffles.

3.2.1 Inertial resistance

To obtain the inertial resistance of the section in the z-direction (refer to figure 3.1 for axes) the pressure drop per meter was calculated at different mass flow rates, as indicated in figure 3.2.

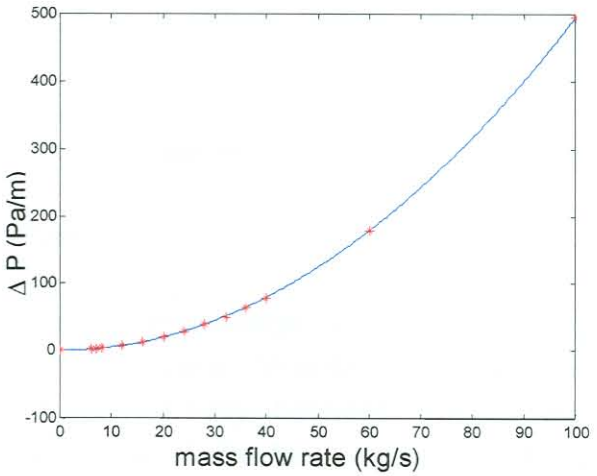

Figure 3.2: Pressure drop per meter through the section in the z-direction

The inertial resistance in the x- and y-directions also needed to be calculated, because the porous part of the inlet section was solved without baffles. For this a more simplified model, consisting of 4 tubes in cross-flow, was used (figure 3.3). The pressure drop per meter for this model is shown in figure 3.4.

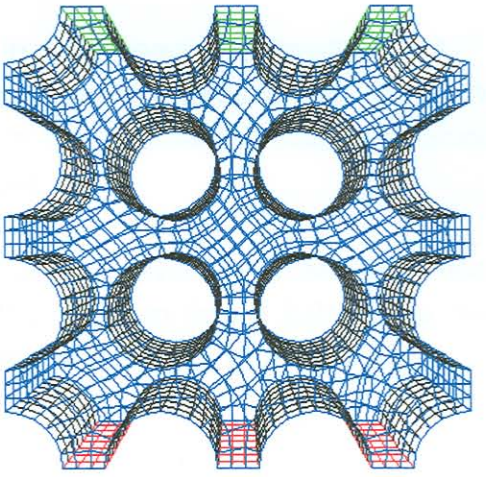

Figure 3.3: FLUENT model of tubes in cross-flow

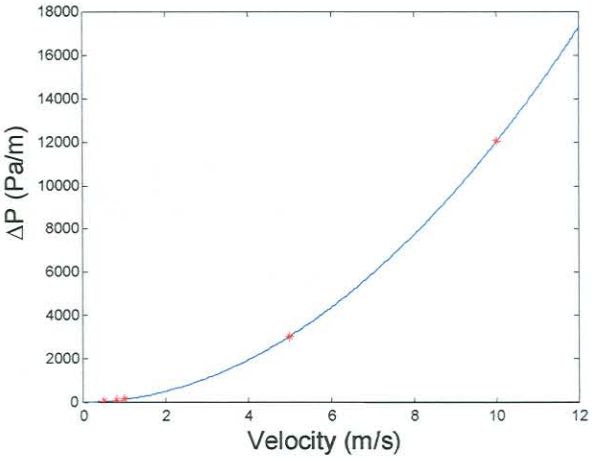

Figure 3.4: Pressure drop per meter in the x and y-direction.

3.2.2 Cross-flow velocities

The HTRI analysis used an average cross-flow velocity value in almost all the excitation frequency calculations. In order to compare the CFD and HTRI results, the average cross-flow velocity between baffles was calculated. Varying distances from the centre of the heat exchanger were used to take the flow patterns into account.

The baffles force the flow in the x-direction, causing much larger cross-flow velocity in the x-direction than in the y-direction. Because of this, the surfaces used to calculate the magnitude of velocity, were chosen in the x-direction. The average cross-flow velocities in the x- and y-directions on the surfaces, were calculated and combined to obtain an average cross-flow velocity magnitude.

Because of the offset in tube spacing between the 12th and 13th tube row (see figure 2.2) the average cross-flow velocity was calculated separately for the two parts. This ensured that the approach cross-flow velocities were calculated and not the gap flow velocities.

Figure 3.5 shows the change in average cross-flow velocity magnitude between a type 3 and type 1 baffle (refer to figure 2.2) in the middle section of the heat exchanger for mass flow rates of 6, 8, 12 and 16 kg/s.

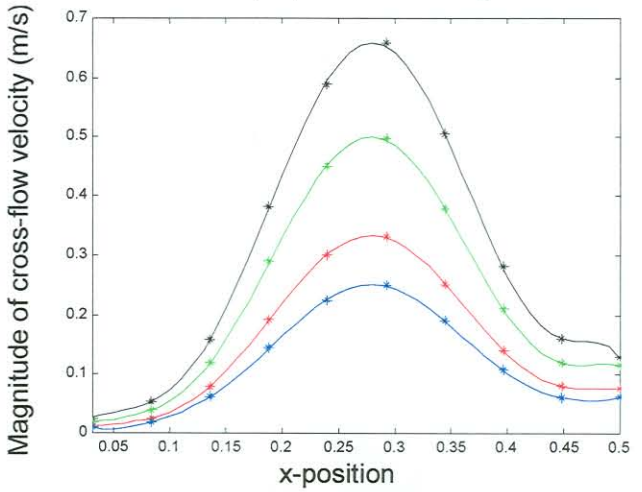

a) bottom section

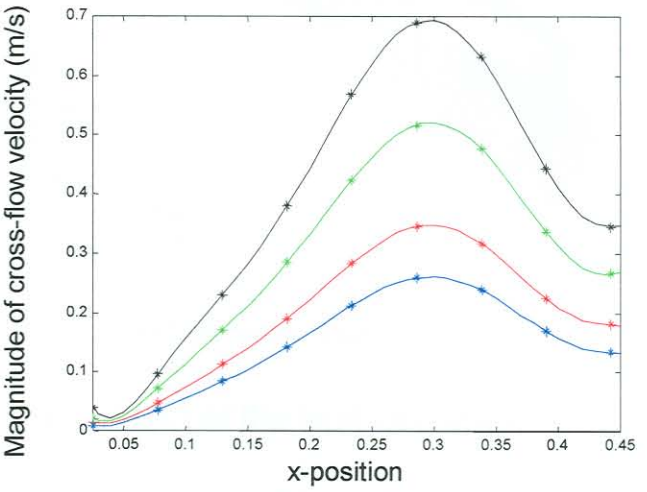

b) top section

Figure 3.5: Velocity magnitude as a function of the x position between baffle type 3 and 1 (blue – 6 kg/s, red – 8kg/s, green – 12kg/s and black – 16 kg/s)

Eighth-order polynomials were fitted through the four sets of data points (figures 3.5 a and b). These polynomials were used to obtain a single equation (for the top and bottom sections respectively) to calculate the magnitude of the cross-flow velocity at any given position (x) and mass flow rate ($\dot{m}$) within the specified range. Only a quarter of the heat exchanger was analysed and the mass flow rate was therefore divided by 4 to obtain the correct velocities through the section.

$$v_{bottom} = 14656.1\frac{\dot{m}}{4}x^8 - 33836.3\frac{\dot{m}}{4}x^7 + 30566.5\frac{\dot{m}}{4}x^6 - 13615.9\frac{\dot{m}}{4}x^5 + 3105.82\frac{\dot{m}}{4}x^4 - 354.814\frac{\dot{m}}{4}x^3 + 22.3272\frac{\dot{m}}{4}x^2 - 0.654188\frac{\dot{m}}{4}x^1 + 0.0132422 \quad 3.1$$

$$v_{top} = -5517.75\frac{\dot{m}}{4}x^8 + 697.8\frac{\dot{m}}{4}x^7 + 8938.07\frac{\dot{m}}{4}x^6 - 8303.33\frac{\dot{m}}{4}x^5 + 3173.48\frac{\dot{m}}{4}x^4 - 615.0\frac{\dot{m}}{4}x^3 + 63.3456\frac{\dot{m}}{4}x^2 - 2.6675\frac{\dot{m}}{4}x^1 + 0.042957 \quad 3.2$$

The same procedure was followed to obtain equations for the cross-flow velocities between baffles type 1 and type 2 and baffles type 2 and type 3 (Appendix C). In figure 3.6 the flow patterns through a section of the heat exchangers are shown with maximum velocity magnitudes (indicated with red) at the baffle plates.

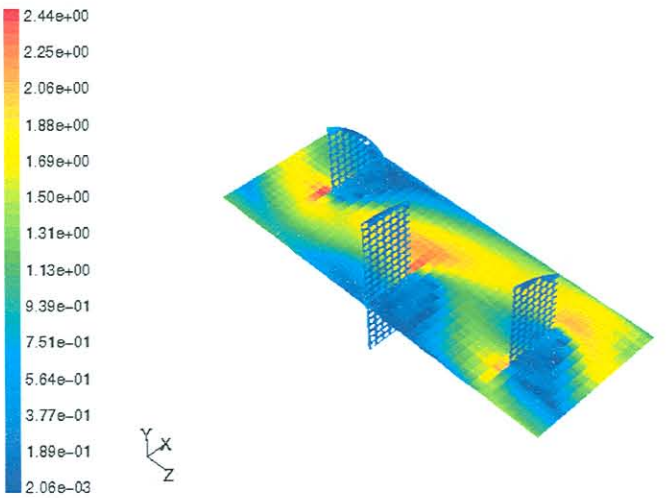

Figure 3.6: Velocity magnitude contour plot through a section of the heat exchanger

3.3 CFD analyses: Inlet section of the heat exchanger

The flow through the inlet section of the heat exchanger was simulated using the porous medium obtained from the previous section, to represent the remaining part of the heat exchanger at the outlet boundary of the inlet section (figure 3.7).

Figure 3.7: Schematic representation of the inlet section

This was done to ensure the necessary back pressure and flow pattern at the outlet boundary.

The adapted mesh consisted of approximately 1.4 million cells. The pressure drop per meter for a mass flow rate of 8 kg/s, was calculated and compared to the value obtained in the previous section and the inertial resistance was adjusted accordingly. This was necessary because the porous section was solved without baffles and the flow could therefore not be forced into the x- or y-directions. The model was then solved for a range of mass flow rates (with a fixed inertial resistance) and the results were again compared with the results of the previous section, as shown in figure 3.8.

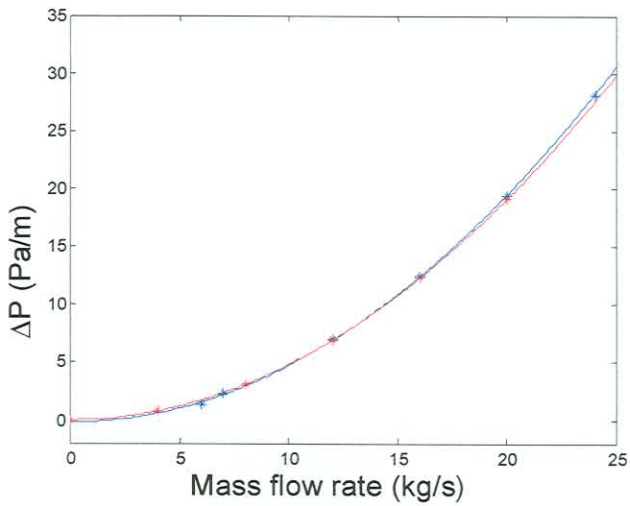

Figure 3.8: Pressure drop per meter
(blue – CFD analyses of repeating section, red – Equivalent porous model)

3.3.1 Cross-flow velocities

For the inlet section, the flow in the y-direction between the tubesheet and the first baffle, as well as the first and second baffle, will be larger, because of the orientation of the inlet. For this reason the surfaces that were used to calculate the average cross-flow velocities in both the x- and y-direction, were chosen in the y-direction. The surfaces between the second and third baffles are the same as for the middle section (see section 3.2.2). Figures 3.9 a) and b) show the average cross-flow velocities between baffle types 1 and 2, as well as between the tubesheet and baffle type 1.

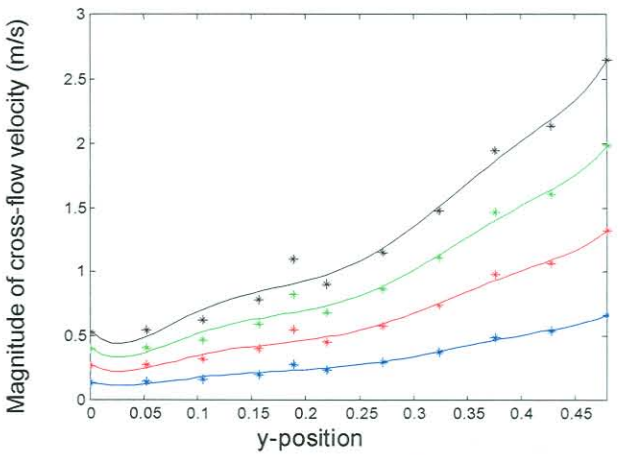

a) Baffles 1 and 2

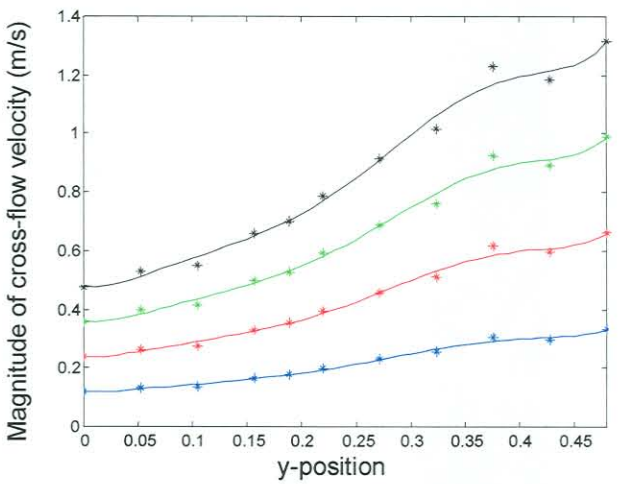

b) Tubesheet and baffle 1

Figure 3.9: Magnitude of average cross-flow velocity (blue-4 kg/s, red – 8 kg/s, green – 12 kg/s and black 16 kg/s)

Sixth-order polynomials were fitted through the data points in figures 3.9 a) and b). In figure 3.9 a) the magnitude of the cross-flow velocities between y-positions 0.15 and 0.2 is higher than the polynomial values due to the larger tube spacing between 12th and 13th tube row. Figure 3.9 b) shows the larger magnitude of

cross-flow velocity at the second tube row (between y-positions 0.35 and 0.4). These polynomials were again used to obtain a single equation to calculate the magnitude of the cross-flow velocity at any given position and mass flow rate within the specified range. Only half of the inlet section was simulated and the mass flow rate was therefore divided by 2, to obtain the correct velocity at the inlet of the heat exchanger.

$$v_{tsbl1} = 333.082\frac{\dot{m}}{2}y^6 - 441.899\frac{\dot{m}}{2}y^5 + 212.266\frac{\dot{m}}{2}y^4 - 45.5719\frac{\dot{m}}{2}y^3 + 4.7624\frac{\dot{m}}{2}y^2 - 0.072717\frac{\dot{m}}{2}y^1 + 0.059951 \quad 3.3$$

$$v_{bl12} = 1034.07\frac{\dot{m}}{2}y^6 - 1548.67\frac{\dot{m}}{2}y^5 + 875.218\frac{\dot{m}}{2}y^4 - 229.245\frac{\dot{m}}{2}y^3 + 28.1241\frac{\dot{m}}{2}y^2 - 1.06629\frac{\dot{m}}{2}y^1 + 0.067350 \quad 3.4$$

Figure 3.10 shows the velocity distribution through the inlet section of the heat exchanger. A small part of the porous section is included in figure 3.10.

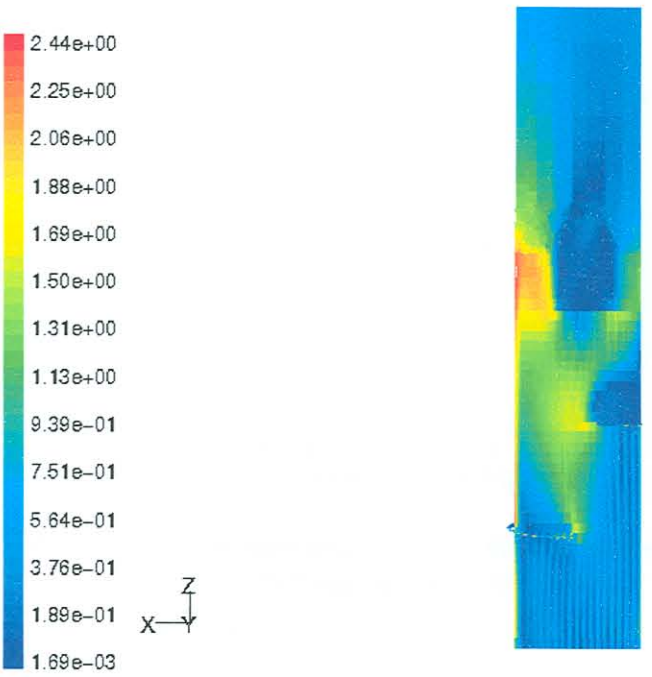

Figure 3.10: Magnitude of velocity over a section of the heat exchanger ($m.s^{-1}$)

3.4 Conclusion

In this chapter, detailed CDF analyses of the heat exchanger were performed to determine the pressure drop, flow patterns and average cross-flow velocities. The average cross-flow velocity values were used to obtain equations that can be used to calculate the magnitude of the cross-flow velocity at any given mass flow rate and position within the specified range. This reduced the computational time to only two simulations, one at the lowest and one at the highest mass flow rate of the range. In figure 3.11, the CFD pressure drop values are compared to the HTRI calculated values. At lower mass flow rates, the pressure drop values for the two methods are the same, but at higher mass flow rates, the CFD pressure drop value is slightly higher than the HTRI value. This is due to the limit in cells used for the analyses as desired in Section 3.2 and Appendix C. Using these pressure drop values to obtain the correct back pressure for the inlet section where the flow velocities are the highest, can further reduce the computational time. The middle-section of the heat exchanger with periodic boundaries need therefore only be analysed at the lowest and highest mass flow rates of the specified range.

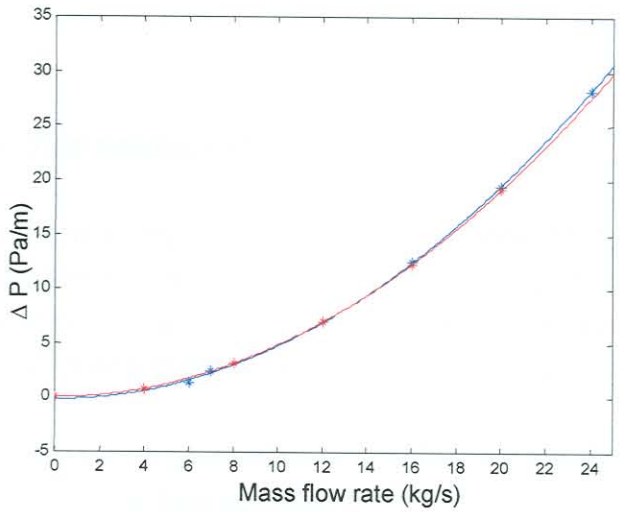

Figure 3.11: Pressure drop per meter through heat exchanger (blue – CFD results, red – HTRI results)

Chapter 4

Experimental results

4.1 Introduction

The HTRI analyses predicted vibration problems at certain mass flow rates. Some additional calculations were also done to determine a number of other important mass flow rates at which vibration may occur (Chapter 2). In Chapter 3, CFD analyses were performed to determine if the velocities used by the HTRI analyses were correct and also to get a better understanding of the flow patterns through the heat exchanger. All the above methods can be used to predict whether or not the shell-and-tube heat exchanger may experience vibration problems at a specific operating mass flow rate. To test whether this predicted vibration actually occurred, vibration measurements on the ES 208 Tail gas shell-and-tube heat exchanger were done at different operational flow rates. Figure 4.1 shows the ES 208 Tail gas heat exchanger at Sasol Synthetic Fuels (SSF).

Figure 4.1 ES 208 Tail gas shell-and-tube heat exchanger

4.2 Measuring procedure

To verify the HTRI and CFD results, it is necessary to do vibration measurements on the heat exchanger. It is not always practical to measure on the inside of the heat exchanger:

- Because of the pressure at which the heat exchanger operates;
- The gas on the shell-side is very corrosive and poisonous; and
- The clearances between the tubes are very small and this makes it inaccessible to vibration equipment.

The vibration measurements were therefore taken on the supports and the shell of the heat exchanger. The operational measurements are covered below, followed by the non-operational measurements.

4.2.1 Operational measurements

The following operational measurements were taken on the ES 208 Tail gas heat exchanger (figure 4.2) at SSF.

- The response of the shell at different flow velocities (positions 1, figure 4.2).
- The response of the supports at different flow velocities (position 2)
- Strain gauge measurements at different flow velocities (position 3).

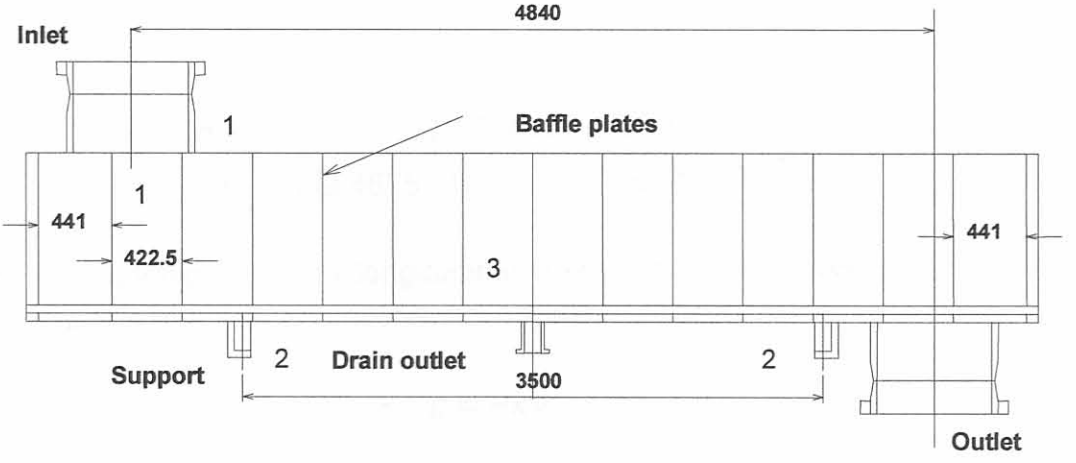

Figure 4.2: Heat exchanger layout

a) Shell and support response measurements

The process of determining tube vibration can be simplified by establishing the relationship between the shell and support vibration and the tube vibration. For this purpose, strain gauges and accelerometers were used. Strain calculations were made to determine the number of strain gauges needed per position to sufficiently measure strain. To obtain the shell bending in the x- and y- directions, at least three strain gauge positions (90 ° apart) are needed, but four positions are preferred, especially if poor contact between the gauge and shell exists.

Strain calculations:

The deflection curve equation (equation 4.1) was obtained using the maximum deflection given by the HTRI results.

$$y = \left(-7.4694 \times 10^{-4}\right)x^2 + \left(9.4675 \times 10^{-4}\right)x \qquad 4.1$$

By differentiating equation 4.1 the angle of rotation of the beam (θ) can be obtained.

$$\theta(x) = \arctan\left(2\left(-7.4694 \times 10^{-4}\right)x + 9.4675 \times 10^{-4}\right) \qquad 4.2$$

The curvature (κ) is the reciprocal of the radius of curvature. For small beam deflections, the distance (*ds*) along the curve may be taken as its horizontal projection (*dx*).

$$\kappa = \frac{d\theta}{dx} = \frac{2\left(-7.4694 \times 10^{-4}\right)}{1 + \left(9.4675 \times 10^{-4} + 2\left(-7.4694 \times 10^{-4}\right)x\right)^2} \qquad 4.3$$

The relationship between longitudinal normal strain and curvature is given by equation 4.4 (Gere and Timoshenko, 1995).

$$\varepsilon = -\kappa y \qquad 4.4$$

where *y* equals the distance between the centre line of the tube and the outside diameter of the tube.

By using equations 4.3 and 4.4, the maximum strain is calculated at 14.2 $\mu\varepsilon$ (micro strain). The strain gauge may be able to measure 14 micro strain but the noise of the associated electronic equipment is in the order of 20 micro strain making accurate measurement with only one strain gauge per position impossible. Four strain gauges were used to amplify the strain measured and were configured as shown in figure 4.3. Two strain gauges in series were connected in parallel to another two strain gauges in series (figure 4.3). This was done to balance the resistance of the Weatstone-bridge.

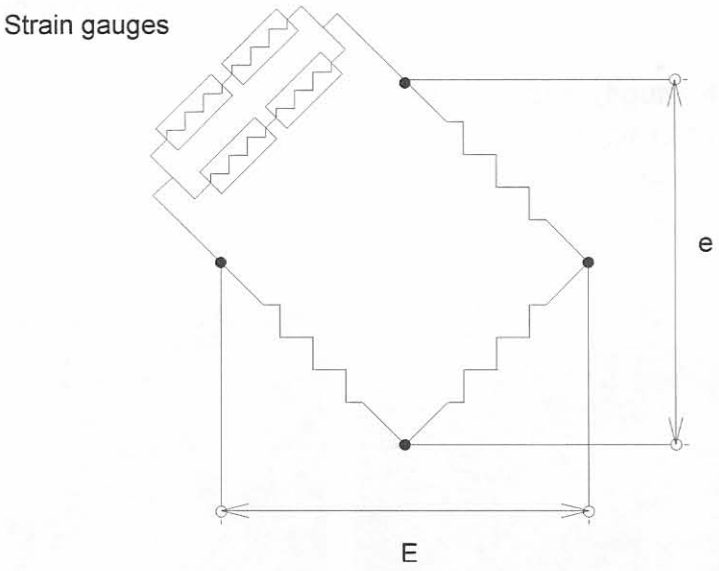

Figure 4.3: Strain gauge configuration

4.2.2 Non-operational measurements

For normal tube-to-baffle clearances, it can be assumed that the tubes are simply supported at the baffle plates, the tolerances of the fitting of the tube may influence the natural frequencies of the tubes. The baffle cut divides some of the tube holes (see figure 2.2), causing those tubes to be supported in one dimension only. Other factors such as corrosion damage, vibration damage and thermal expansion can also influence the natural frequencies.

With non-operational measurements other factors such as external sources of vibration can also be obtained. These include vibration transmitted to the heat exchanger via the foundations and supports of the heat exchanger, as well as the piping connected to the heat exchanger. This is an important part of the measuring procedure, especially if the measurements are taken on a plant where various other sources may cause external vibration.

4.3 Results

Vibration measurements on the heat exchanger were taken on three occasions. In the section that follows, as well as in Appendix E, the results of the vibration measurements will be covered in detail and in Chapter 5 these results will be compared to the predicted values of the HTRI analyses (Chapter 2) as well as the CFD results (Chapter 3).

4.3.1 Shell and support response

Vibration measurements on the shell and supports (figure 4.4) were taken by using three 500 mV/g accelerometers (Entek E326A02), one 100 mV/g accelerometer (Entek E327A01), four 2 V/g accelerometers (PCB 393A11) and 16 KFW-5-120-C1-16L5M2R strain gauges (four at each position).

a) Measuring position at inlet of heat exchanger (A4) (Position 1 from figure 4.2) *b) Measuring position 90° to outlet (A2)*

c) Measuring position at outlet support (B1 & B2) (Position 2 from figure 4.2) *d) Measuring position at inlet support (B3 & B4)*

e) Measuring position at centre of HE *f) Strain gauge measurements (R4)*

Fig. 4.4: Vibration measurement positions

Some of the measuring positions, accelerometers and strain gauges that were used are shown in figure 4.4 (refer to Appendix D for more information on measuring positions).

The flow rate through the heat exchanger was varied by first opening the bypass valve in 100 mm increments. After the bypass valve was fully opened, the heat exchanger inlet valve was closed with 100mm increments (figures 4.5 and 4.6).

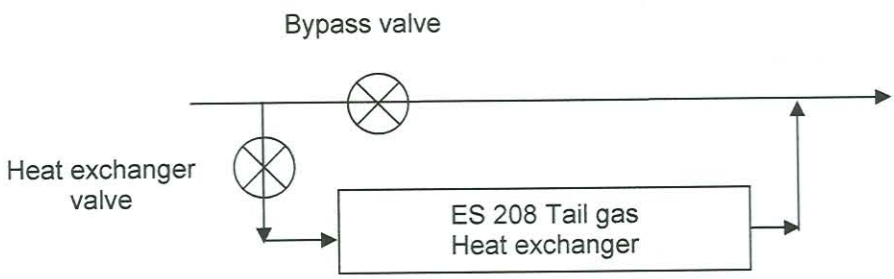

Figure 4.5: Valve configuration

The losses through the two loops were calculated using the pressure drop curve obtained by the HTRI analyses (figure 2.7). (Refer to Appendix B for more detail). The HTRI pressure drop curve was first compared to the CFD pressure drop results through the heat exchanger, as shown in figure 3.11.

The CFD pressure drop was only obtained for lower flow rates because of the limit of y^+ values. The two pressure drop curves compare very well over the flow velocity range and was therefore suitable to be used for the flow rate calculations.

Figure 4.6: 24" Wedge gate valve being closed

The time at which each measurement was taken, was recorded. Logged flow rates at other points in the piping system (upstream) was used to determine the specific flow rate for each measurement. This data was also used for a Power Spectrum Density (PSD) curve, to determine the frequency of pressure fluctuation in the supplied tail gas. The flow rates in normal cubic meters per hour (km^3n/h) are given in figure 4.7 for the two ES 208 Tail gas heat exchangers that are in parallel, as well as the combined flow rate. The PSD curve confirmed randomly fluctuating flow before entering the heat exchanger. The heat exchanger that was used for the measurements is indicated with "B".

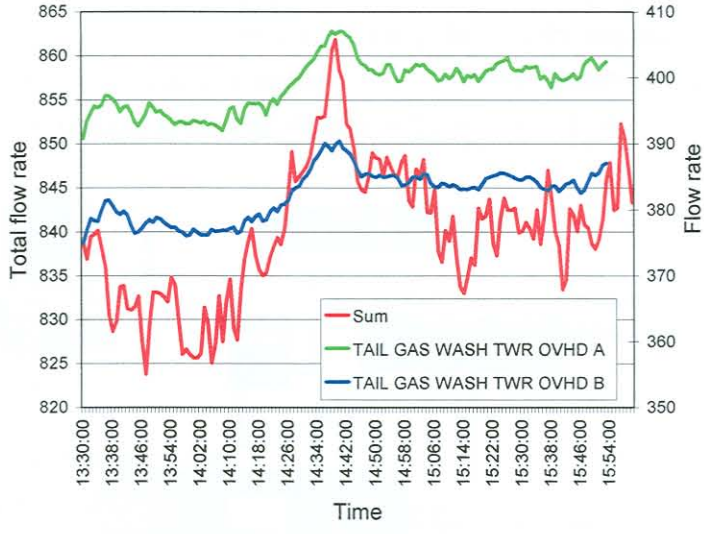

Figure 4.7: Flow rate in km^3n/h for the two tail gas heat exchangers.

The flow rates in figure 4.7 are given at normal temperature and pressure (273 K and 101kPa). The density of the gas at normal temperature and pressure were calculated (Appendix A) and used to convert the volumetric flow rates to mass flow rates. Table 4.1 gives the mass flow rates as calculated in Appendix B. The wedge gate valve average loss coefficients from White (1994) were used to obtain the losses across the valves.

Table 4.1: Mass flow rates through the heat exchanger

Set	Velocity (m/s)	Mass flow rate (kg/s)
1	14.7797	83.42325
2	3.4873	19.68374
3	2.1131	11.92732
4	1.402	7.913393
5	1.1158	6.297841
6	0.9699	5.474317
7	0.9194	5.189442
8	0.8735	4.930306
9	0.7931	4.476549
10	0.6087	3.435545
11	0 (non operational)	0
12	0 (non operational)	0

A record length of 1024 samples was used and twenty averages were taken for every set of measurements. The sampling frequency was 256 Hz and a Hanning window was used. PSDs were calculated for each measurement set, using Siglab 20-42 data acquisitioning equipment. For the strain gauge measurements a KWS 3073 strain gauge amplifier was used (see figure. 4.8).

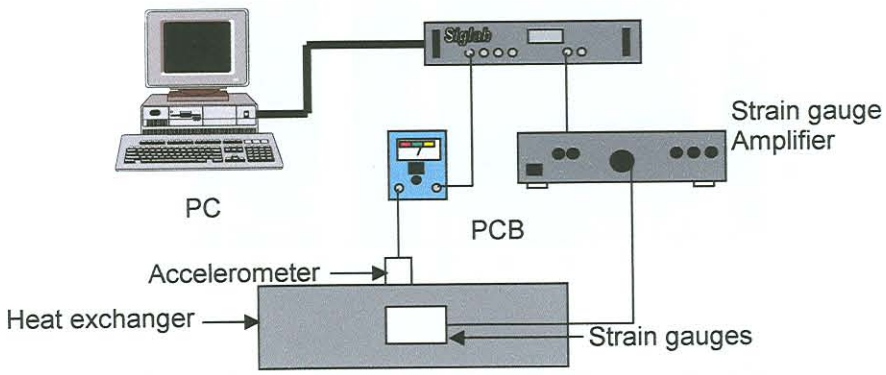

Figure. 4.8: Measuring equipment configuration

Waterfall plots for the strain gauge measurements for the 12 measuring sets are shown in figure 4.9, as well as a contour plot in figure 4.10. From figure 4.10 an increase in strain amplitude at 12.5 Hz, 20 Hz and 28 Hz can be detected. The 28 Hz line coincides with one of the predicted natural frequencies. A slight increase in amplitude is visible at a mass flow rate of 5.5 kg/s (set 6). Above 30 Hz no other frequencies are detected. This may be due to rigid body vibration or small displacement associated with the vibration frequency which results in strain measurements that are smaller than the electronic noise of the equipment. (Appendix E, figures E.1 to E.6)

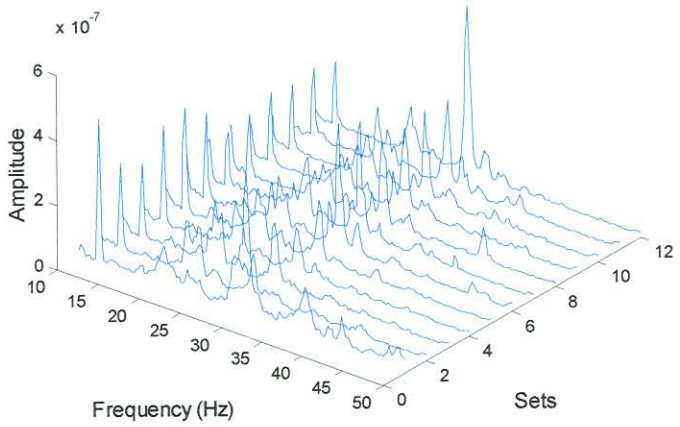

Figure 4.9: Waterfall plot of strain gauge measurements

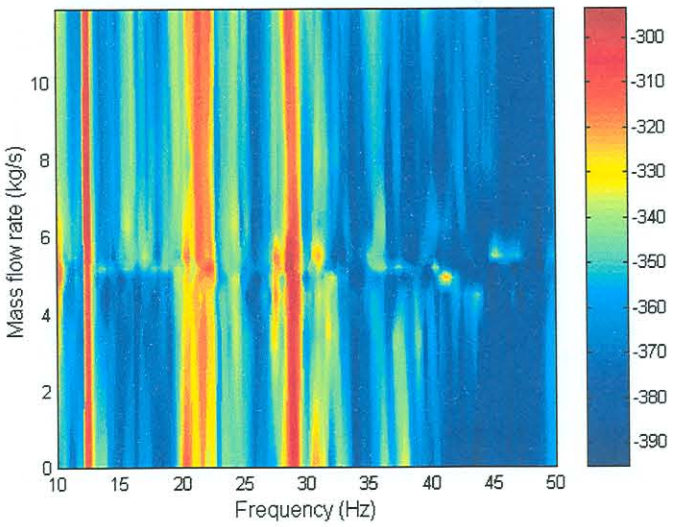

Figure 4.10: Contour plot of strain gauge measurements

The support measurements as shown in figures 4.11 and 4.12, as well as in Appendix E (figures E.7 to E.14), indicated vibration between 27.5 Hz and 28.5 Hz. These values are similar to the HTRI and FEM predicted values of 28.56 Hz and 27.76 Hz respectively. Vibration bands between 35 Hz and 43 Hz, as well as between 53 Hz and 56 Hz were observed. Large vibration amplitudes were also measured at 80 Hz.

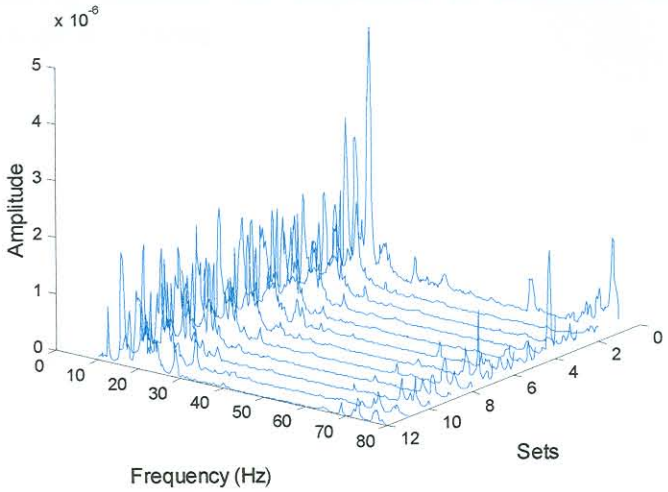

Figure 4.11: Acceleration measurement at support

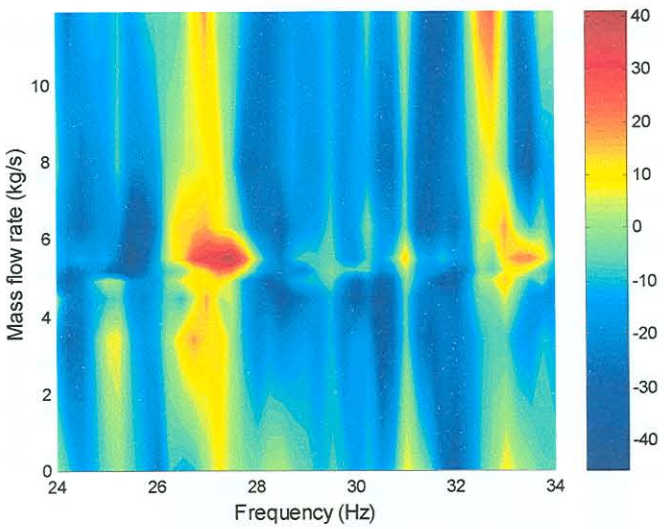

Figure 4.12: Contour plot of difference in support measurements

Measurements at the shell of the heat exchanger indicated vibration throughout the heat exchanger at 24 Hz, 28.5 Hz and 36 Hz (figures 4.13, 4.14 and Appendix E figures E.15 to E.22). Frequency bands between 50 Hz and 60 Hz, and 70 Hz and 80 Hz were also observed.

In both the shell and support measurements an increase in vibration amplitude at a mass flow rate of about 6 kg/s and frequencies of 27.5 Hz of 28.5 Hz, were visible. At some measuring position the amplitude of vibration, at these frequencies, decreased at higher flow rates.

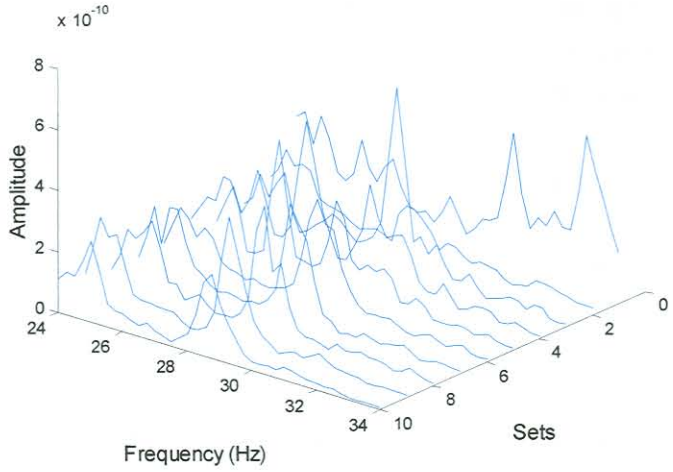

Figure 4.13: Waterfall plot of acceleration measurements at the outlet

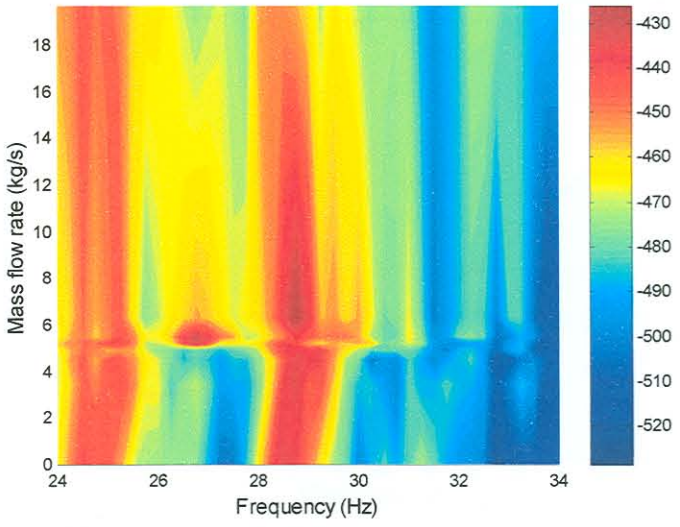

Figure 4.14: Contour plot of acceleration measurements

Chapter 5

Comparison of results

5.1 Introduction

In Chapter 2 a number of HTRI analyses were done to determine at which mass flow rates the ES 208 Tail gas heat exchanger may experience vibration. CFD analyses were done in Chapter 3 to determine the pressure drop and cross-flow velocity distributions through the heat exchanger to compare with the values obtained from the HTRI results. The results of the vibration measurements are described in Chapter 4 and Appendix E. In this chapter, the results of the previous three chapters will be compared to determine the accuracy of the HTRI predictions, as well as the margins of uncertainty associated with these predictions.

5.2 Comparison of pressure drop values through the heat exchanger

In Chapter 3 (figure 3.11 repeated as figure 5.1) the HTRI and CFD pressure drop values per meter were compared. This was done to calculate the mass flow rate through the heat exchanger for the measured results. At lower mass flow

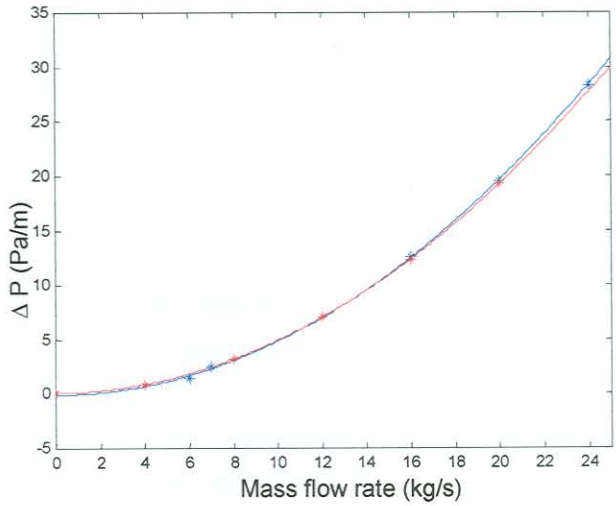

Figure 5.1: Pressure drop per meter through heat exchanger (blue – CFD results, red – HTRI results)

rates the pressure drop values for the two methods are the same, but at higher mass flow rates the CFD pressure drop value is slightly higher than the HTRI value. This is due to the limitations in the number of cells used for the CFD analyses as described in Section 3.2 and Appendix C.

5.3 Excitation frequencies and critical velocity.

The CFD analyses calculated the flow velocities and pressure distributions inside the heat exchanger. To determine the excitation frequencies, these velocity values obtained from the analyses can be substituted into equations 1.15 to 1.18. In Section 5.3.1 to 5.3.3 the CFD calculated average cross-flow velocities (Chapter 3) are compared to the HTRI calculated values (Chapter 2). The excitation frequencies associated with these average cross-velocities are compared to the measurements from Chapter 4 in Section 5.3.4.

5.3.1 Vortex shedding average cross-flow velocity

In Chapter 2 the HTRI analysis used the average cross-flow velocity to calculate the excitation frequency values. HTRI uses one average velocity value for a specific mass flow rate, and that particular velocity was compared to the velocities calculated with the CFD analyses. The problem with the CFD velocities is that due to the flow patterns through the heat exchanger, a different average cross-flow velocity is obtained at each cell.

If the cell velocity values at a specified plane between two baffles are averaged, as was done in Chapter 3, the cross-flow velocities between the different baffles can be represented by a single equation (red line in figure 5.2). This equation is a function of the position of the plane from the centre of the heat exchanger, as well as the mass flow rate (as described is Chapter 3 and Appendix C). The HTRI analyses only calculated the lowest natural frequency of the tube, therefore only the average cross-flow velocity associated with excitation at the lowest natural frequency of the tube was compared.

In figure 5.2 the HTRI average cross-flow velocity and baffle tip velocity, as well as the CFD average cross-flow velocity in the y-direction is shown.

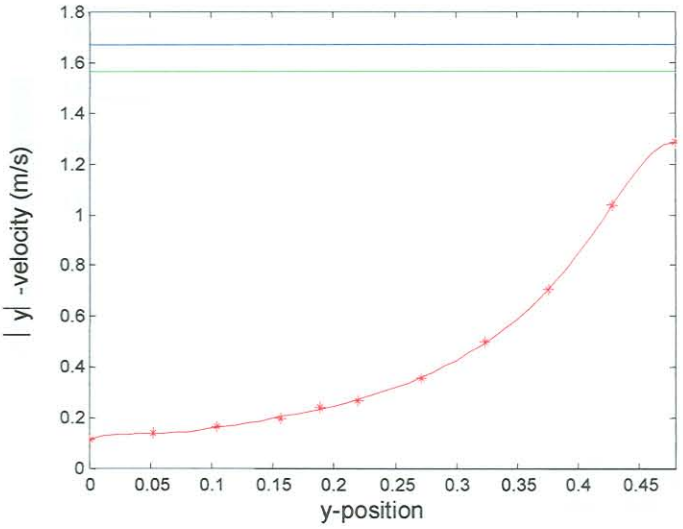

Figure 5.2: Cross-flow velocity between baffle type 1 and 2 (at inlet section) in the y-direction for a mass flow rate of 8 kg/s.
(red – CFD results, blue – HTRI average cross-flow velocity, green – HTRI baffle tip velocity)

In the section directly underneath the inlet of the heat exchanger (figure 5.2), the flow is mainly in the y-direction, but in figure 5.3 the cross-flow velocity in the x-direction was taken into account and slightly more accurate results were obtained.

Figures 5.2 and 5.3 both indicate that the maximum average cross-flow velocity is at the inlet opening of the shell (at y=0.5). This maximum value compares fairly well with the predicted HTRI cross-flow velocity and baffles tip velocity, although HTRI predicted an average cross-flow velocity value that is 20 percent higher than the maximum CFD value.

The tubes below the inlet nozzle of the heat exchanger are only supported at every third baffle (figure 2.2). These tubes are more likely to vibrate, because their natural frequency of 28.56 Hz will match the excitation frequency due to vortex shedding. The CFD average cross-flow velocity in figure 5.3 is only for the tube section between baffle type 1 and 2. The velocities between baffle type 2 and 3, and type 3 and 1 also need to be taken into account.

Figures 5.4 and 5.5 show the velocities between baffle type 2 and 3, and 3 and 1 together with the HTRI predicted velocities. The CFD calculated velocity values are considerably lower than at the section directly below the inlet (between baffle type 1 and 2) as well as the HTRI average cross-flow velocity and baffle tip velocity.

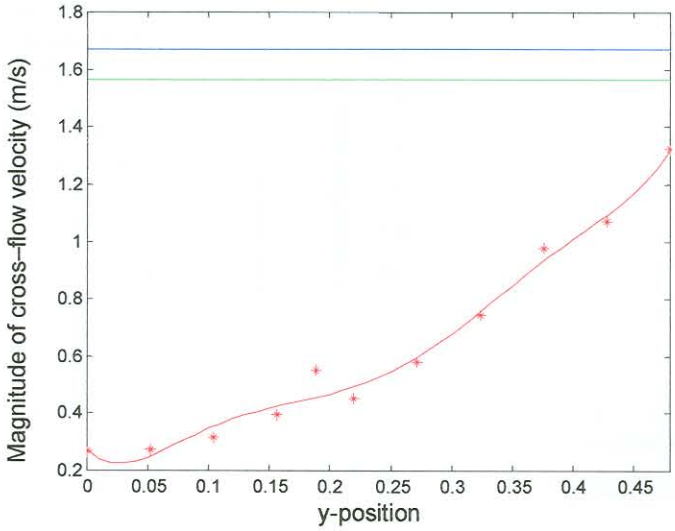

Figure 5.3: Magnitude of cross-flow velocity between baffle type 1 and 2 (at inlet section) for a mass flow rate of 8 kg/s. (red – CFD results, blue – HTRI average cross-flow velocity, green – HTRI baffle tip velocity)

The unsupported tube length at the shell wall section does not experience the predicted HTRI average cross-flow velocity over the whole length, but only across the first section between baffle type 1 and 2. If a 20 percent margin of uncertainty on the HTRI average cross-flow velocity is used, only 1.3 percent of the tubes are subjected to a vortex shedding frequency that equals their natural frequency across a third of the tubes unsupported length. The vortex shedding frequency across the remaining tubes is well below the natural frequency of the tubes.

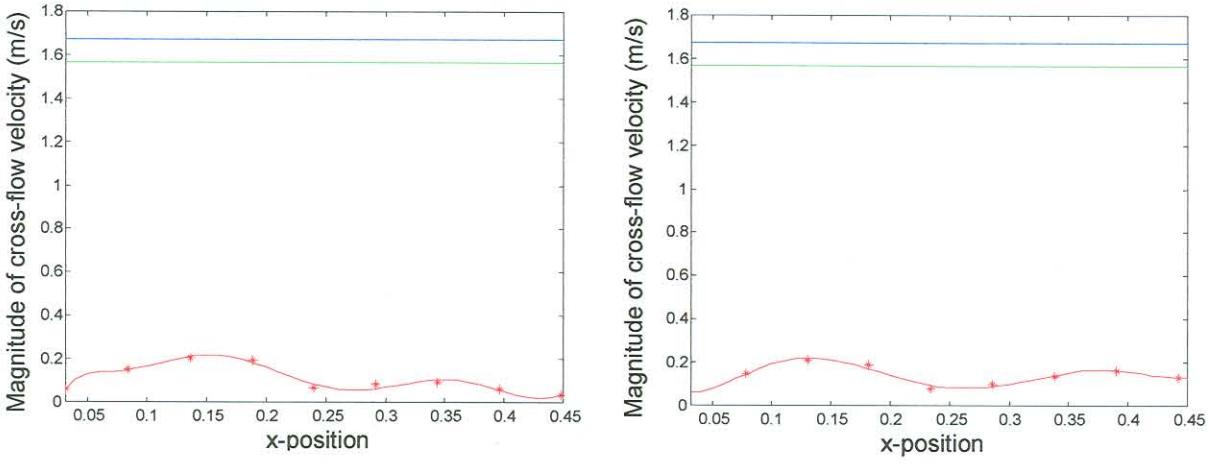

a) Bottom section *b) top section*

Figure 5.4: Magnitude of cross-flow velocity between baffle type 2 and 3 for a mass flow rate of 8 kg/s. (red – CFD results, blue – HTRI average cross-flow velocity, green – HTRI baffle tip velocity)

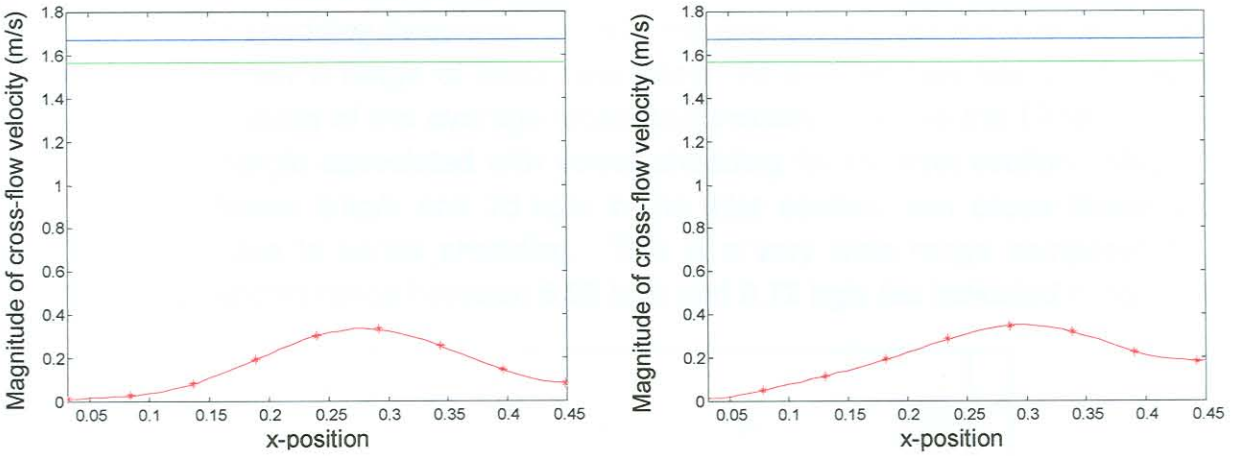

a) Bottom section *b) top section*

Figure 5.5: Magnitude of cross-flow velocity between baffle type 3 and 1 for a mass flow rate of 8 kg/s.
(red – CFD results, blue – HTRI average cross-flow velocity, green – HTRI baffle tip velocity)

The predicted HTRI mass flow rate at which vibration due to vortex shedding will occur for the inlet and middle sections is 7.95 kg/s and 8.004 kg/s respectively (table 2.1). These mass flow rates differ by less than 0.7 percent and only the 7.95 kg/s value will therefore be used in the following section. If the predicted HTRI average cross-flow velocity and baffle tip velocity associated with mass flow rate of 7.95 kg/s is compared to CFD average cross-flow velocities over a range of mass flow rates, different tubes at different positions in the heat exchanger, will be excited (figure 5.6).

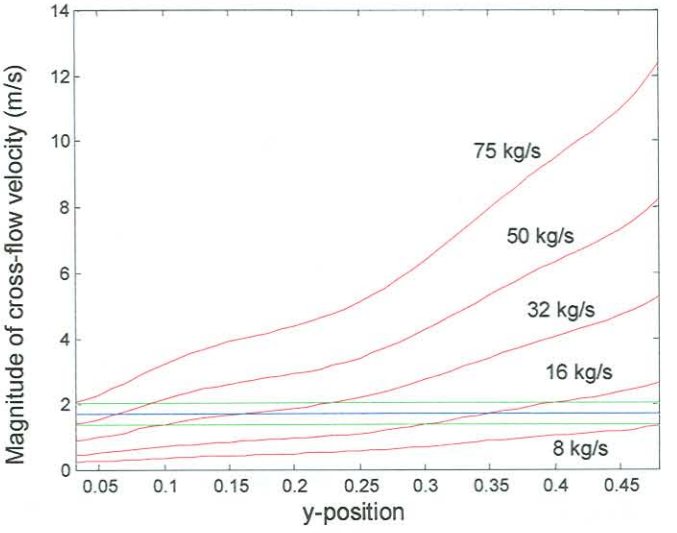

Figure 5.6: Magnitude of cross-flow velocity between baffle type 1 and 2 for a range of mass flow rates.
(red – CFD results, blue – HTRI average cross-flow velocity, green – 20 percent margin)

This implies that there is not a single mass flow rate that can be associated with the vortex shedding frequency, but that the heat exchanger is subjected to vortex shedding over a range of mass flow rates. At a mass flow rate of 75 kg/s, the CFD magnitude of the average cross-flow velocity is above the HTRI cross-flow velocity margin associated with vortex shedding for the inlet section. Mass flow rates between 8 kg/s and 75 kg/s in the inlet section, can cause flow-induced vibration due to vortex shedding. This is a very wide range compared to the HTRI predicted range between 6.95 kg/s and 9.72 kg/s (as indicated in figure 5.7)

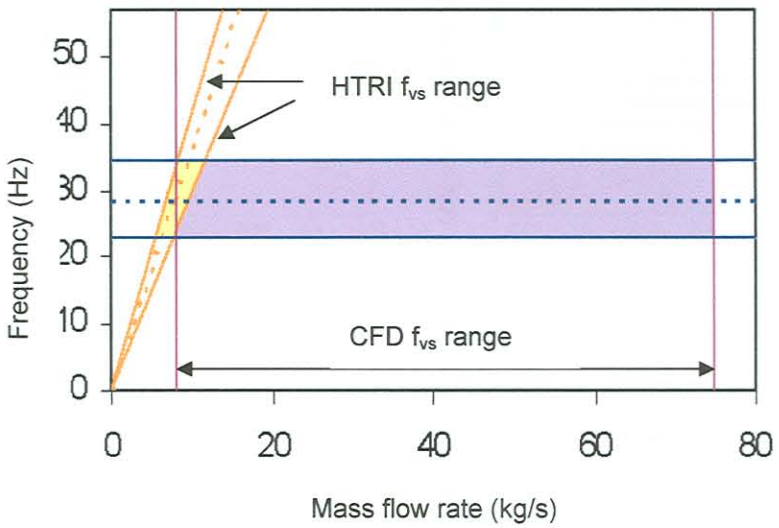

Figure 5.7: HTRI and CFD vortex shedding range

In the middle section of the heat exchanger, flow-induced vibration due to vortex shedding can occur from a mass flow rate of 32 kg/s and upwards. (Figures 5.8 a) and b), and 5.9 a) and b)).

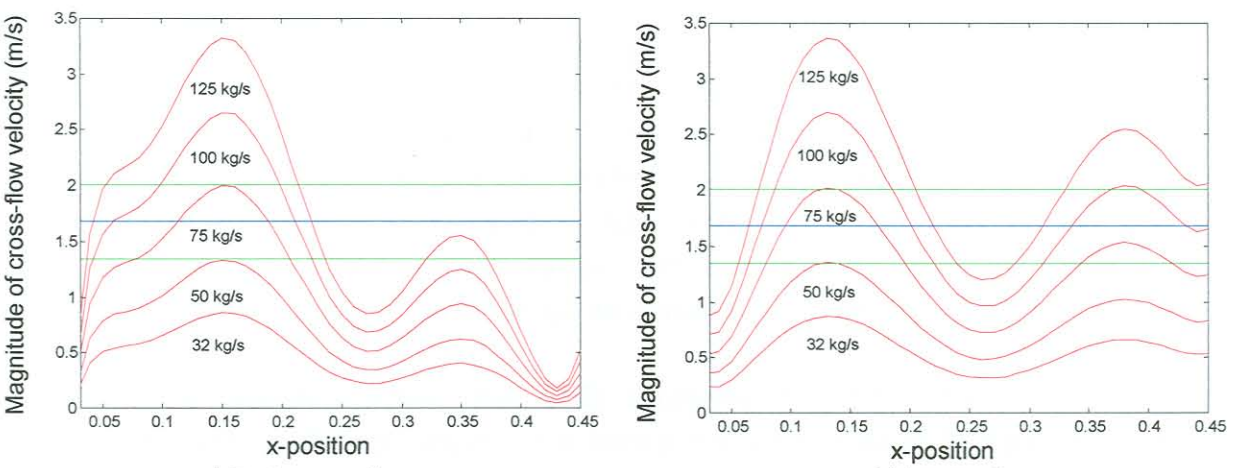

a) Bottom section *b) top section*

Figure 5.8: Magnitude of cross-flow velocity between baffle type 2 and 3 for a range of mass flow rates.
(red – CFD results, blue – HTRI average cross-flow velocity, green – 20 percent margin)

The CFD analyses indicated that the triple segmental baffle directs the flow more parallel to the tubes and the cross-flow velocity is therefore not so high as in a double segmental baffle configuration.

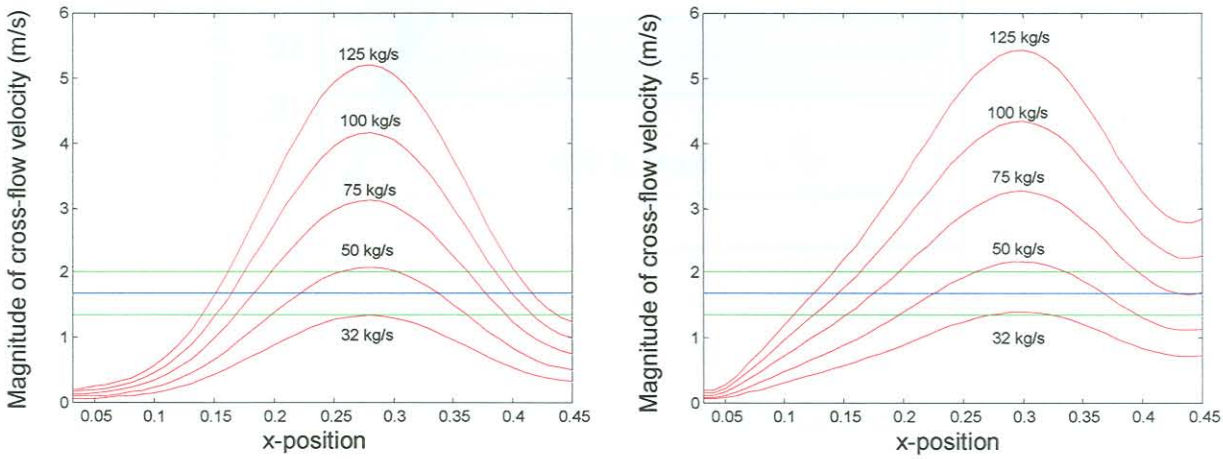

a) Bottom section *b) top section*

Figure 5.9: Magnitude of cross-flow velocity between baffle type 3 and 1 for a range of mass flow rates.
(red – CFD results, blue – HTRI average cross-flow velocity, green – 20 percent margin)

5.3.2 Turbulence buffeting

The HTRI predicted mass flow rate at which fluid-induced vibration due to turbulence buffeting will occur is 9.982 kg/s and 10.054 kg/s for the inlet and middle sections respectively. The associated HTRI average cross-flow velocity for the inlet section mass flow rate of 9.982 kg/s is 1.93 m/s. The CFD magnitudes of the average cross-flow velocities were compared to the HTRI value of 1.93 m/s. A margin of 20 percent was used for the HTRI average cross flow velocity value. At the inlet section, the CFD analyses predicted a mass flow range between 9.3 kg/s and 77 kg/s where vibration may occur. The HTRI analyses predicted a flow range between 8.7 kg/s and 11.3 kg/s (using a 20 percent margin of uncertainty) as indicated in figure 5.10.

At the middle section the CFD analyses predicted that vibration, due to turbulence buffeting, would occur from a mass flow rate of 37 kg/s and upwards.

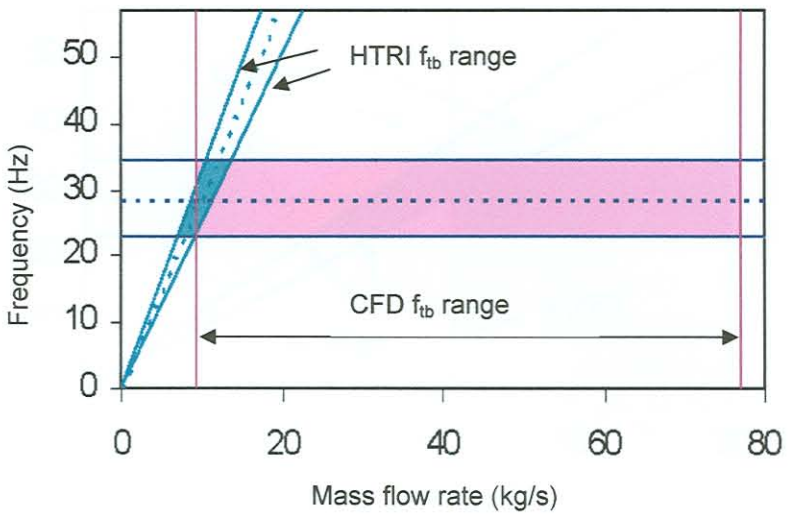

Figure 5.10: HTRI and CFD turbulence buffeting range

5.3.3 Fluid-elastic instability

The HTRI predicted critical velocity of 2.89 m/s (equation 2.2) was also compared to the CFD average cross-flow velocity values. The mass flow rate associated with the velocity of 2.89 m/s as 14.22 kg/s, as predicted by HTRI. If a 20 percent margin of uncertainty is used, the HTRI analyses predicts vibration due to fluid-elastic instability from a mass flow rate of 11.4 kg/s and upwards. The CFD analyses predicted a mass flow range from 14 kg/s and upwards.

If the CFD predicted mass flow ranges calculated for fluid-elastic instability, turbulence buffeting and vortex shedding are combined, flow induced vibration will occur from a mass flow rate of 8 kg/s and upwards. The HTRI analyses predicted what vibration will occur in the heat exchanger from a mass flow rate of 6.95 kg/s and upwards (as indicated in figure 5.11). The HTRI and CFD values compared well, only because in this specific case, the vortex shedding range overlapped with the turbulence buffeting range, which in turn overlapped with the fluid-elastic instability range.

If the vortex shedding, turbulence buffeting and fluid elastic-instability regions do not overlap (as shown in figure 5.12), safe operating zones are predicted by the HTRI analyses. The CFD analyses however do not predict safe operating zones after a certain minimum mass flow rate.

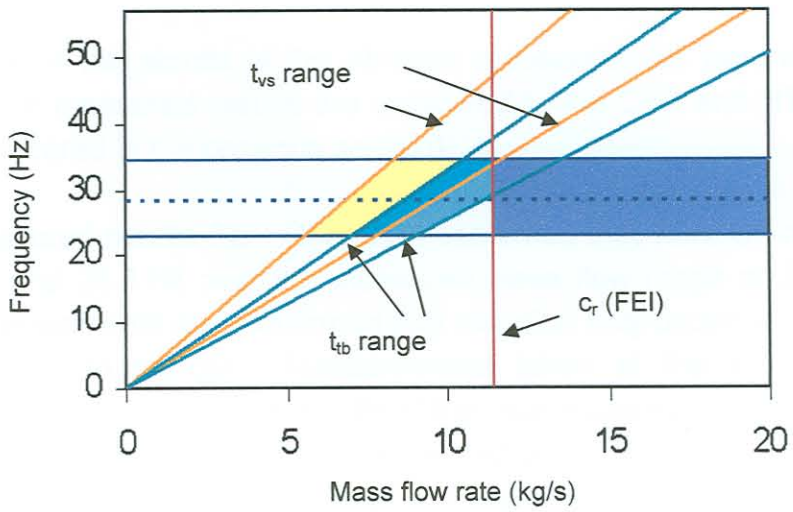

Figure 5.11: HTRI turbulence buffeting, vortex shedding and fluid-elastic instability range

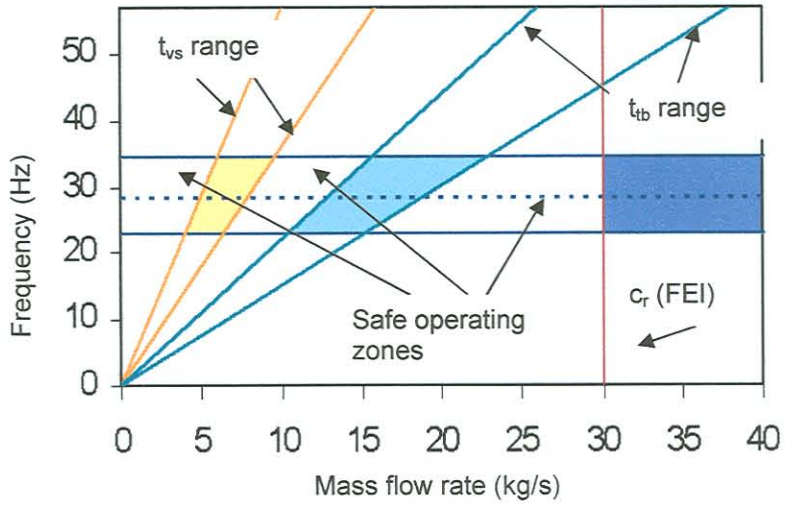

Figure 5.12: Turbulence buffeting, vortex shedding and fluid- elastic instability range

It is important to remember that only small sections of the tubes experience excitation at different mass flow rates. Even if the flow rate is within the above-mentioned range, vibration can only occur if the excitation forces on the sections of the tube are sufficiently large to cause the whole tube to vibrate.

The problem however, is that the unsupported tube length is not subjected to a constant average cross-flow velocity across the whole tube length, but the magnitude and direction of the cross-flow velocities differ over the tube length. The effect that this has on the tube's vibration, can only be obtained if a complete fluid-structure interaction analysis is done on the unsupported length.

5.3.4 Comparison of experimental results

In Chapter 4 the results of the vibration measurements were described. In this section the measured results are compared to the CFD and HTRI results (which were compared in the previous section).

The measured results from Chapter 4 confirmed that vibration did occur between 27.5 Hz and 28.5 Hz over the measured mass flow range of 3 kg/s to 100 kg/s. The measurements also confirmed that vibration only occurred in certain sections of the heat exchanger. Measurements taken at the supports of the heat exchanger, as well as at the middle of the heat exchanger shell (position B1 to B4 and R1 to R4), indicated vibration between 27.5 Hz and 28.5 Hz. The measurements at the inlet and outlet section of the heat exchanger did not detect vibration at the above mentioned frequency range.

The measured and HTRI predicted natural frequency, differs by less than 4 percent. The slight difference in the measured frequency, is because of differences in the way the tubes are supported at the baffle plates. The baffle hole clearances may differ due to manufacturing or corrosion of the tubes, or baffles. Corrosion can also cause the tubes' natural frequency to change due to a change in mass of the tube.

The measured flow range where vibration occurred, also compares well with the CFD predicted range (figure 5.13 and Appendix E). The amplitude of the vibration measurements on the shell and supports are very small. It was not possible to measure the actual tube vibration amplitude, but the HTRI analyses also predicted very small tube vibration amplitudes (0.3 mm) due to turbulence buffeting and vortex shedding. These analyses did not take the vibration amplitude due to fluid-elastic instability into account (figure 2.4). From the measured results, no increase in amplitude could be noticed if the mass flow rate was increased above the critical velocity.

Only vibration at the lowest natural frequency of the tubes was measured. No vibration at the other three natural frequencies, as described in Chapter 2, was detected. This may be because the amplitude of the vibration at the higher natural frequencies was too small and the strain gauge measurements only gave good results at lower frequencies.

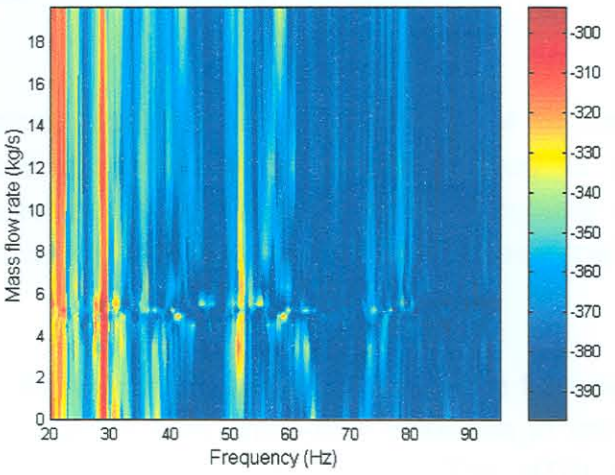

Figure 5.13: Contour plot of strain gauge measurements on the heat exchanger shell.

5.4 Margin of uncertainty

In Section 5.2 the HTRI average cross-flow velocities were compared to the CFD average cross-flow velocity values. Although the maximum CFD predicted velocity value differed by 20 percent, the remaining CFD predicted average cross-flow velocities varies between 20 percent to 99 percent from the HTRI predicted values at the predicted HTRI excitation mass flow rates. The following factors that influence the margin of uncertainty in the prediction of flow induced vibration were described in the previous chapters:

- The temperature and pressure variation at the shell-side inlet of the heat exchanger: In Chapter 2 a difference of less that 0.4 percent in vortex shedding and turbulence buffeting over the specified temperature range were calculated. The pressure variation at the inlet of the heat exchanger only affected the acoustic frequencies (174.75 Hz), which in this specific instance, could not lead to vibration because it did not coincide with the natural frequency of the tubes.

- The tube support assumptions that are used: FEM analyses in Chapter 2 calculated the difference in natural frequencies for different support configurations. If the wrong support configuration is used, a difference of 36 percent for this specific case was obtained.

- The clearance between the baffle hole and tube as well as tube and baffle corrosion: Corrosion in the heat exchanger influences the natural frequencies of

the tubes, because of the reduction of mass and difference in the support configuration.

- The correlation values used in calculating the natural frequencies of the tubes: In Chapters 1 and 2, correlation graphs are used to obtain the natural frequencies of the tubes. The TEMA and HTRI calculated natural frequencies differ by 3 percent due to the difference in added mass coefficient (k) that was used.

- The flow patterns through the heat exchanger: The flow patterns through the heat exchanger can cause high cross-flow velocities in certain regions of the heat exchanger as described in Chapter 3. The HTRI analyses predicted velocities that are up to 99 percent higher than the CFD predicted average cross-flow velocities.

To quantify the margin of uncertainty in the prediction of flow-induced vibration, a more detailed analysis of the factors that influence the natural frequency of the tube are needed. These include better correlation values for different tube configurations and heat exchanger configurations, as well as a better representation of flow velocities through the heat exchanger.

Chapter 6

Conclusion and recommendations

6.1 Conclusion

The cost associated with the replacement of heat exchangers is considerable. Therefore more intensified efforts are being made to predict flow-induced vibration. The literature study indicated that if the velocity through the heat exchanger could be predicted more accurately, the margin of uncertainty in predicting the vortex shedding, turbulence buffeting and fluid-elastic instability could be reduced. HTRI analyses can be used to determine if the heat exchanger will be within the 20 percent uncertainty range when the mass flow rate through the heat exchanger is increased. The problem with the HTRI analyses are the prediction of the mass flow rates associated with the excitation of the tubes due to vortex shedding, turbulence buffeting and fluid-elastic instability. The HTRI analyses do not take the flow patterns through the heat exchanger into account and the average cross-flow velocity that is used to calculate the excitation frequencies, is not representative of the velocities through the heat exchanger.

If the HTRI excitation frequency calculations at the increased load are between 0 and 80 percent of the natural frequency, the heat exchanger can be operated at the increased load without experiencing flow induced vibration. When the excitation frequency exceeds 80 percent of the natural frequency, additional methods are required to determine if vibration will occur.

The CFD analyses led to a better understanding of the flow velocities through the heat exchanger. The magnitude and direction of the cross-flow velocity, varies over the tube length. By using CFD analyses, more accurate cross-flow velocity values throughout the heat exchanger were obtained. In the case of the tail gas heat exchanger that was analysed, the HTRI results predicted the average cross-flow velocity 20 percent higher than the maximum average CFD cross-flow velocity (at the second tube row). By using CFD analyses, one can not only predict the flow velocities through the heat exchanger, but also predict where the velocities that could cause flow-induced vibration will occur. In the case of the tail

gas heat exchanger, only a very small portion of the tubes are subjected to flow-induced vibration conditions. Modifying only a small section of the heat exchanger could easily solve this problem.

CFD analyses are expensive and in order to reduce the computational time the average cross-flow velocity values were used to obtain velocity equations. These equations can be used to calculate the magnitude of the cross-flow velocity at any given mass flow rate and position within the specified range. This reduced the computations to only four simulations, one at the lowest and one at the highest mass flow rate of the range for the inlet and middle section of the heat exchanger. These velocities can be used to calculate the excitation frequencies needed for the force distribution on the heat exchanger tubes. The dynamic pressure also varies due to vortex shedding, which causes alternating forces. This also needs to be taken into account. The effect that the force distribution has on the tube's vibration, can only be obtained if a complete fluid-structure interaction analysis is done on the unsupported tube length.

To determine the vibration amplitudes without doing a fluid-structure interaction analysis, the vibration of the heat exchanger was measured at different flow rates. The experimental results that were described in Chapter 4, confirmed that vibration did occur at the lowest natural frequency as predicted by the HTRI analysis. The measurements indicated that vibration (at the lowest natural frequency) occurred over the entire mass flow range that was measured. This is also in good correlation with the CFD analyses, which predicted that vibration would occur over a range of mass flow rates, and not at a single value, as predicted by the HTRI analyses. The measured vibration amplitude was very small and may not cause premature failure of the heat exchanger. Failure can only be predicted once a fatigue analysis is performed on the heat exchanger.

6.2 Recommendations and future work

CFD work

By determining the correlation between the inlet velocity and the velocity distribution through the heat exchanger for different tube to pitch ratios, tube configurations, heat exchanger configurations and baffle configurations, more accurate vibration predictions can be made without the use of too many expensive CFD analyses.

In the CFD analyses, a problem was identified with flow over tubes in large structures. The number of cells that are needed to solve the problem and still obtain reasonable results became excessive. Due to limitations in computational power, only simulations with a mass flow rate lower than 25 kg/s could be solved. More computational power is needed if larger mass flow rates or structures need to be solved.

To determine if the forces on the tubes are sufficiently large to cause premature failure of the heat exchanger, fluid-structure interaction analyses and fatigue analyses should be performed.

Experimental work

The strain gauge measurements provided good results at lower frequencies, with the added advantage that strain gauges are inexpensive in comparison with accelerometers. Strain gauge measurements can therefore be used to monitor the vibration levels of a heat exchanger. These measurements are taken on the shell of the heat exchanger. Better measuring techniques are needed to determine the correlation between tube and shell, and tube and support vibration.

To quantify the margin of uncertainty in the prediction of flow-induced vibration, a more detailed analysis of the factors that influence the natural frequency of the tube, are needed. These include better correlation values for different tube configurations and heat exchanger configurations, as well as a better representation of flow velocities through the heat exchanger.

References

Brenneman, B., and Gurdal, R.J., 1997, A Time Domain Solution of Fluid-Elastic Instability in Steam Generator Tubes, *4th International Symposium on Fluid-Structure Interaction, Aeroelasticity, Flow-Induced Vibration and Noise ASME*, Fairfield, NJ, Vol. 2, pp. 145-151.

Chen S.S., 1991, Flow-Induced Vibration of and Array of Cylinders; Part 1, *The Shock and Vibration Digest*, Des. Vol. 23 No. 2, pp. 3-7.

Chen S.S., 1992, Flow-Induced Vibration of and Array of Cylinders; Part 2, *The Shock and Vibration Digest*, Des. Vol. 23 No. 1, pp. 3-7.

Chen, S.S., Cai, Y., and Srikantiah, G.S., 1997, Fluid-Damping-Controlled Instability of Tubes in Cross-Flow, *4th International Symposium on Fluid-Structure Interaction, Aeroelasticity, Flow-Induced Vibration and Noise ASME*, Fairfield, NJ, Vol. 2, pp. 153-162.

Chen, Y.N., 1968, Flow-Induced Vibration and Noise in Tube bank Heat exchangers due to von Karman streets, *Journal of Engineering for Industry*, Vol. 90, 134-146.

Chen, Y.N., and Weber, M., 1970, Flow-Induced Vibration in Tube Bundle Heat Exchangers with Cross and Parallel Flow, *Flow Induced Vibration in Heat Exchangers*, ed. D.D. Reiff, Vol. 6, pp. 55-77, ASME, New York.

Chenoweth, J.M., 1998, Flow-Induced Vibration, *Heat Exchanger Design Handbook (HEDH)*, pp. 4.6.1-4.6.6-4.

Escoe, A.K., 1997, Flow-Induced Vibration in a Steam Condenser and its Successful Redesign, *4th International Symposium on Fluid-Structure Interaction, Aeroelasticity, Flow-Induced Vibration and Noise ASME*, Fairfield, NJ, Vol. 2, pp. 239-247.

Fitz-Hugh, J.S., 1973, Flow-Induced Vibration in Heat Exchanger, *International Symposium on Vibration Problems in Industry, Keswick, England, UK, Atomic Energy Authority, Windscale and Natl. Physical Lab.,* Paper No. 427, pp. 1-17, Teddington.

FLUENT, 1999, Version 5.1, Fluent Inc., 10 Cavendish Court, Centerra Resource Park, Lebanon, NH, USA.

Frick, T.M., 1997, An Empirical Wear Projection Technology with Steam Generator Tube Applications and Relations to Work-Rate and Wear Simulations/Tests, *4th International Symposium on Fluid-Structure Interaction, Aeroelasticity, Flow-Induced Vibration and Noise ASME*, Fairfield, NJ, Vol. 2, pp. 275-282.

GAMBIT, 1999, Manuals, Version 1.1, Fluent Inc., 10 Cavendish Court, Centerra Resource Park, Lebanon, NH, USA.

Gere, J.M. and Timoshenko, S.P., 1995, Mechanics of materials, Third SI Edition, Chapmal & Hall.

Gidi, A., Weaver, D.S., and Judd, R.L., 1997, Two-Phase Flow Induced Vibration of Tube Bundles with Tube Surface Boiling, *4th International Symposium on Fluid-Structure Interaction, Aeroelasticity, Flow-Induced Vibration and Noise ASME*, Fairfield, NJ, Vol. 2, pp. 381-389.

Goyder, H.G.D., 1997, Margins of Uncertainty in the Prediction of Fluid-elastic Instability in Heat Exchanger Tube Bundles, *4th International Symposium on Fluid-Structure Interaction, Aeroelasticity, Flow-Induced Vibration and Noise ASME*, Fairfield, NJ, Vol. 2, pp. 127-136.

Haaland, S.E., 1983, Simple and Expliceit Formulas for the Fiction Factor in Turbulent Pipe Flow, *Fluids Eng.,* March, pp. 89-90.

Hartlen, R.T., and Anderson, H.L., 1980, Experience with Heat Exchanger Tube Vibration in a Large Utility, *Flow-Induced Heat Exchanger Tube Vibration presented at the winter annual meeting of the ASME Chicago, Illinois*, Vol. 9, pp. 35-42.

HTFS, 1992, Research Symposium, Handbook Items, Computer Code TASC.

Inada, F., Kawamura, K., and Yasuo, A., 1997, Fluid-Elastic Force Measurements on a Tube Bundle in Two Phase Cross-Flow, *4th International Symposium on Fluid-Structure Interaction, Aeroelasticity, Flow-Induced Vibration and Noise ASME*, Fairfield, NJ, Vol. 2, pp. 357-364.

Kassera, V., 1997, Three Dimensional CFD-Analyses of Tube Vibrations Induced by Cross Flow, *4th International Symposium on Fluid-Structure Interaction, Aeroelasticity, Flow-Induced Vibration and Noise ASME*, Fairfield, NJ, Vol. 2, pp. 137-143.

Kawamura, K., Yasuo, A., and Inada, F., 1997, Turbulence-Induced Tube Vibration in a Parallel Steam-Water Two-Phase Flow, *4th International Symposium on Fluid-Structure Interaction, Aeroelasticity, Flow-Induced Vibration and Noise ASME*, Fairfield, NJ, Vol. 2, pp. 83 -91.

Kissel, J.H., 1972, Flow Induced Vibration in Heat Exchangers – A practical Look, *AIChE Paper 8, 13th Natl. Heat transfer Conference*, Denver.

Lever, J.H., and Weaver, D.S., 1982, A Theoretical Model for Fluidelastic Instability in Heat Exchanger Tube Bundles, *Pressure Vessel Technology*. 104, pp. 147-196.

Mills, A.F., 1995, Basic Heat and Mass Transfer, IRWIN.

Oengören, A. and Ziada, S., 1997, Flow Periodicity and Acoustic Resonance in Parallel Triangle Tube Bundles, *4th International Symposium on Fluid-Structure Interaction, Aeroelasticity, Flow-Induced Vibration and Noise ASME*, Fairfield, NJ, Vol. 2, pp. 183-192.

Price, S.J., and Paidoussis, M.P., 1984, An Improved Mathematical Model for the Stability of Cylinder Rows Subject to Cross flow, *Journal of Sound and Vibration 97*, pp. 615-640.

Raj, B., Kasiviswanathan, K.V., Jayakumar, T., Muralidharan, N.G., and Raghu, N., 1999, Fresh Insight into the Technology of Heat Exchangers through Failure Analysis and Quality Management, *International Journal of COMADEM*, pp. 12-29.

Rao, M.S.M., Laskowski, L.J., Srikantiah, G.S., and Ahluwalia, K.S., 1997, Prediction of Tube Wear due to Flow-Induced Vibration in PWR Steam Generators, *4th International Symposium on Fluid-Structure Interaction, Aeroelasticity, Flow-Induced Vibration and Noise ASME*, Fairfield, NJ, Vol. 2, pp. 257-264.

Romberg, O., and Popp, K., 1997, Random Excitation by Fluid Forces Acting on a Single Flexible Tube in Bundles Subjected to Cross-Flow, *4th International Symposium on Fluid-Structure Interaction, Aeroelasticity, Flow-Induced Vibration and Noise ASME*, Fairfield, NJ, Vol. 2, pp. 173-181.

Sauvé, R.G., Morandin, G., and Savoia, D., 1997, Probabilistic Methods for the Prediction of Damage in Process Equipment Tubes Under Nonlinear Flow-Induced Vibration, *4th International Symposium on Fluid-Structure Interaction, Aeroelasticity, Flow-Induced Vibration and Noise ASME*, Fairfield, NJ, Vol. 2, pp. 283-289.

Soper, B.M.H., 1980, The Effect of Tube Layout on the Fluid-Elastic Instability of Tube Bundles in Cross-Flow, *Flow-Induced Heat Exchanger Tube Vibration presented at the winter annual meeting of the ASME Chicago, Illinois*, Vol. 9, pp. 1-9.

TEMA,1988, Standards of Tubular Exchanger Manufacturers Association, 7th edition, New York.

Van Wylen, G.J., Sonntag, R.E. and Borgnakke, C., 1993, Fundamentals of Classical Thermodynamics 4th ed., John Wiley & Sons, Inc, NJ

Weaver, D.S., Fitzpatrick, J.A. and ElKashlan, M., 1987, Strouhal numbers for heat exchanger tube arrays in cross-flow, *ASME Journal Pressure Vessel Technology,* Vol 109, pp. 219-223.

Weaver, D.S. and Groover, L.K., 1978, Cross-flow induced vibrations in a tube bank – Vortex shedding, *Journal of Sound and Vibration, Vol 59 (2), pp. 277-294.*

White, F.M, 1991,Viscous Fluid Flow, Second Edition, McGraw-Hill.

White, F.M, 1994, Fluid Mechanics, Third Edition, McGraw-Hill.

Yetisir, M., McKerrow, E., and Pettigrew, M.J., 1997, Fretting-Wear Damage of Heat Exchanger Tubes: A Proposed Damage Criterion Based on Tube Vibration Response, *4th International Symposium on Fluid-Structure Interaction, Aeroelasticity, Flow-Induced Vibration and Noise ASME*, Fairfield, NJ, Vol. 2, pp. 291-299.

Appendix A

Composition and density of Tail gas

A.1 Composition of tail gas

Table A.1 given the composition of tail gas as measured at SSF with molecular weight of 17.9 kg/kmol.

Table A.1: Composition of tail gas

	Volume %
CO_2	11.7
C_2H_4	2.15
C_2H_6	0.913
H_2	36.31
CH_4	37.55
CO	1.049
C_3H_6	3.3
C_3H_8	1.8
i-C_4H_{10}	2.2
n-C_4H_{10}	1
C_4H_8	0.6
cis-C_4H_8	1.4

A.2 Density of tail gas

The equation of state for gases at low density is given by the following equation (Van Wylen *et al.* 1993):

$$P\bar{v} = \bar{R}T \qquad \text{A.1}$$

Equation A.1 can be written in terms of the total volume:

$$PV = mRT \qquad \text{A.2}$$

R is the gas constant for the particular gas, and can be calculated as follows:

$$R = \frac{\overline{R}}{M} \qquad \text{A.3}$$

By substituting $\overline{R}$, the universal gas constant (8.3145 kN m/kmol K) and M, the molecular weight of tail gas (17.9 kg/kmol) into equation A.3, a gas constant of 0.464497 kN m/kmol K is obtained.

A.2.1 Normal conditions

The measured flow rates through the heat exchanger were measured at normal conditions (101 kPa and 273 K). If the pressure and temperature are substituted into equation A.2, a density of 0.796 kg/m^3 is obtained.

A.2.1 Operating conditions

By substituting the inlet temperature (328K) and pressure (3225 kPa) into equation A.2, a density of 21 kg/m^3 is obtained.

Appendix B

Flow velocity calculations

B. 1 Flow velocity calculations

The flow velocity through the heat exchanger was altered by first opening the bypass valve in 100 mm increments and then closing the heat exchanger valve also in increments of 100 mm. The losses in both the loops were calculated as follows:

B.1.1 Bypass loop

The total pipe length is 15.81 m with three 90° elbow fittings, one 24" gate valve, one branch flow tee and one line flow tee. The average loss coefficient K for the gate valve as a function of the fractional opening is given in figure B.1.

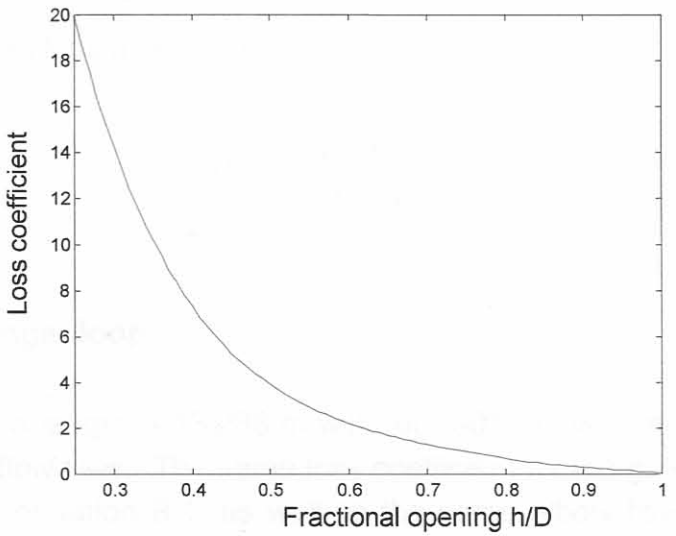

Figure B.1: Average loss coefficient for partially open gate valves (White, 1994)

Loss coefficient data from White (1994) was used to fit a 5^{th} order polynomial curve:

$$K_{gv} = -2.061\times10^{2}\left(\frac{h}{D}\right)^{5} + 8.533\times10^{2}\left(\frac{h}{D}\right)^{4} - 1.414\times10^{3}\left(\frac{h}{D}\right)^{3} + 1.183\times10^{3}\left(\frac{h}{D}\right)^{2} - 5.077\times10^{2}\left(\frac{h}{D}\right)^{1} + 91.86 \quad \text{B.1}$$

The 90° elbow fitting loss coefficient was calculated as 0.25, the line flow tee loss coefficient as 0.07 and the branch flow tee loss coefficient as 0.41, using data from White (1994).

This gives a total loss coefficient K_t of:

$$K_t = 1.23 + K_{gv} \quad \text{B.2}$$

The friction factor (f) was calculated using an explicit formula given by Haaland (1983) as

$$\frac{1}{f^{\frac{1}{2}}} \approx -1.8\log\left[\frac{6.9}{\mathrm{Re}_d} + \left(\frac{\frac{\varepsilon}{d}}{3.7}\right)^{1.11}\right] \quad \text{B.3}$$

The total head loss across the bypass is:

$$\Delta h_{bp} = \frac{V_{bp}}{2g}\left(\frac{f_{bp}L_{bp}}{d_{bp}} + K_t\right) \quad \text{B.4}$$

B.1.2 Heat exchanger loop

The total pipe length is 13.288 m with four 90° elbow fittings, one 24" gate valve, two branch flow tees. The same loss coefficient for the gate valve was used as in fig. B.1 and equation B.1, as well as the same elbow fitting loss coefficient and branch flow tee loss coefficient.

This gives a total loss coefficient of:

$$K_t = 1.82 + K_{gv} \quad \text{B.5}$$

Equation B.3 was used to calculate the friction factor (*f*).

The pressure drop across the heat exchanger is a function of the mass flow rate. A curve was fitted through the HTRI pressure values (see figure B.3 and equation B.6), using Matlab's `polyfit` function.

$$\Delta P = 7.828\times10^{-3}\dot{m}^2 + 7.008\times10^{-2}\dot{m} - 3.787\times10^{-1} \qquad \text{B.6}$$

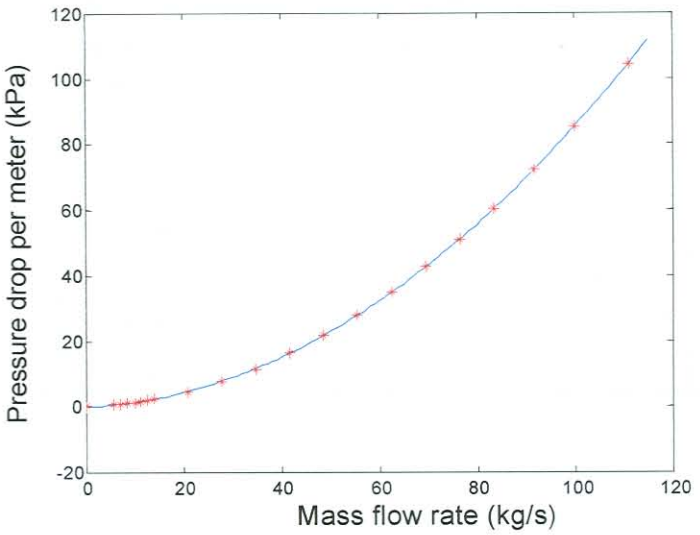

Figure B.2: Pressure drop per meter across the heat exchanger

The total head loss across the heat exchanger loop is:

$$\Delta h_{he} = \frac{V_{he}}{2g}\left(\frac{f_{he}L_{he}}{d_{he}} + K_t\right) + \frac{\Delta p_{he}}{\rho g} \qquad \text{B.7}$$

The heat exchanger and bypass loop is in parallel and therefore the loss is the same in each loop. By solving equation B.8 with Matlab's `fsolve` function, the flow velocities through the heat exchanger were calculated as shown in Table B.1.

$$\Delta h_{he} - \Delta h_{bp} = 0 \qquad \text{B.8}$$

Table B.1 Velocities associated with measuring sets

Set	Bypass valve pos.	Heat Exc. valve pos.	Total velocity	Bypass velocity	Heat Exc. velocity
1	Closed	open	14.77972	0.00000	14.77972
2	100mm	open	14.78307	11.29579	3.48728
3	200mm	open	14.8547	12.74159	2.11311
4	300mm	open	14.92133	13.51935	1.40198
5	400mm	open	15.09434	13.97858	1.11576
6	500mm	open	15.24324	14.27338	0.96986
7	560mm open	open	15.18231	14.26292	0.91939
8	open	100mm	15.08767	14.17513	0.91254
9	open	200mm	15.0557	14.15513	0.90057
10	open	300 mm	15.02711	14.15363	0.87348
11	open	400mm	15.03283	14.23974	0.79309
12	open	500mm	15.01238	14.40372	0.60866
13	open	590mm (closed)	15.11233	15.11233	0.00000

Appendix C

CFD results

C.1 Middle section: Mesh adaptation

The cross flow velocities, pressure drop and y^+ values were calculated and the mesh adapted using the maximum y^+ value (figures C.1, C.2 and C.3) for a mass flow rate of 28 kg/s.

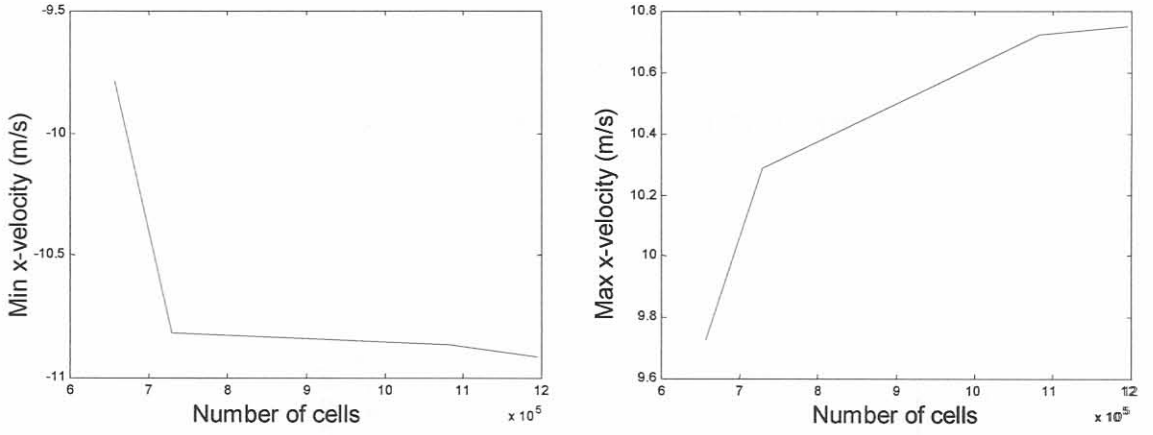

*a) **Minimum** x-velocity* *b) Maximum x-velocity*

Figure C.1: Minimum and maximum cross-flow velocity in the x-direction

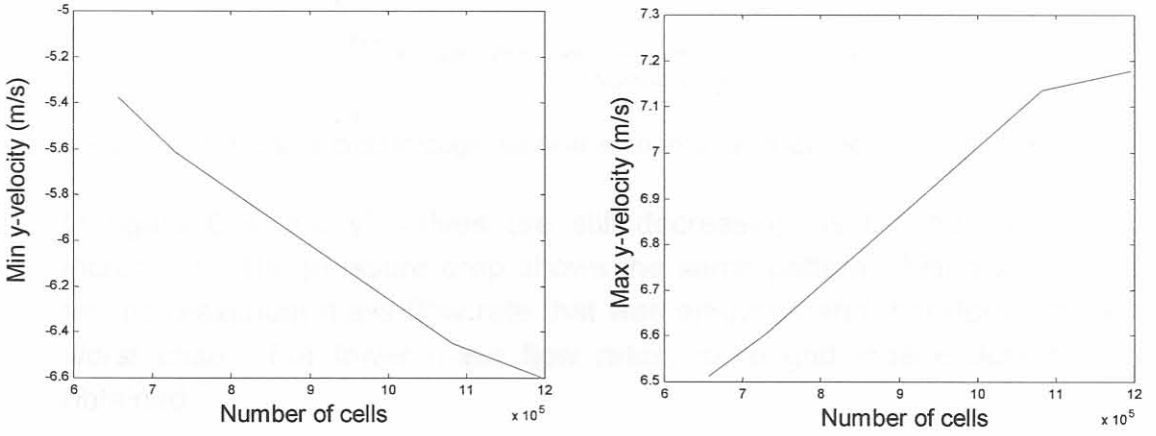

a) Minimum y-velocity *b) Maximum y-velocity*

Figure C.2: Minimum and maximum cross-flow velocity in the y-direction

Figures C.1 and C.2 show the cross-flow velocities as functions of the number of cells used in the FLUENT analysis. In most cases the velocities started to converge. Due to limitation in computational power, the mesh could not be adapted further.

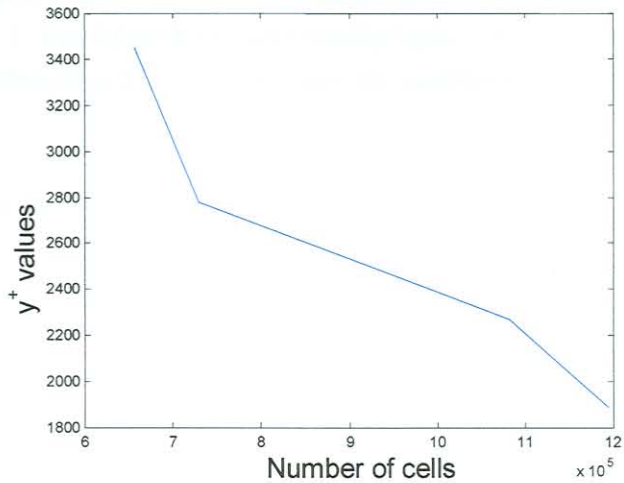

Figure C.3: y^+ values as a function of the number of cells used

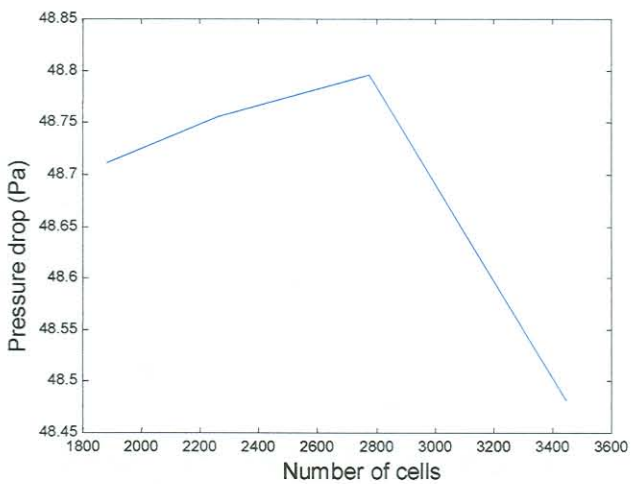

Figure C.4 Pressure drop through the heat exchanger as a function of the number of cells used

In figure C.3, the y^+ values are still decreasing as the number of cells are increased. The pressure drop shows the same pattern. Figures C.1 to C.4 are for the maximum mass flow rate that was analysed and therefore represents the worst case. For lower mass flow rates, more grid independent results were obtained.

C.2 Middle section: Average cross-flow velocity magnitude equations

The average cross-flow velocity between the baffles at different distances from the centre of the heat exchanger, was calculated as described in Chapter 3 (sections 3.2.2 and 3.3.1). The magnitude of the cross-flow velocities between baffle type 3 and 1, the tubesheet and baffle type 1 and between baffle type 1 and 2, are given in Chapter 3. The remaining sections of the heat exchanger are given below.

C.2.1 Baffle type 1 and 2

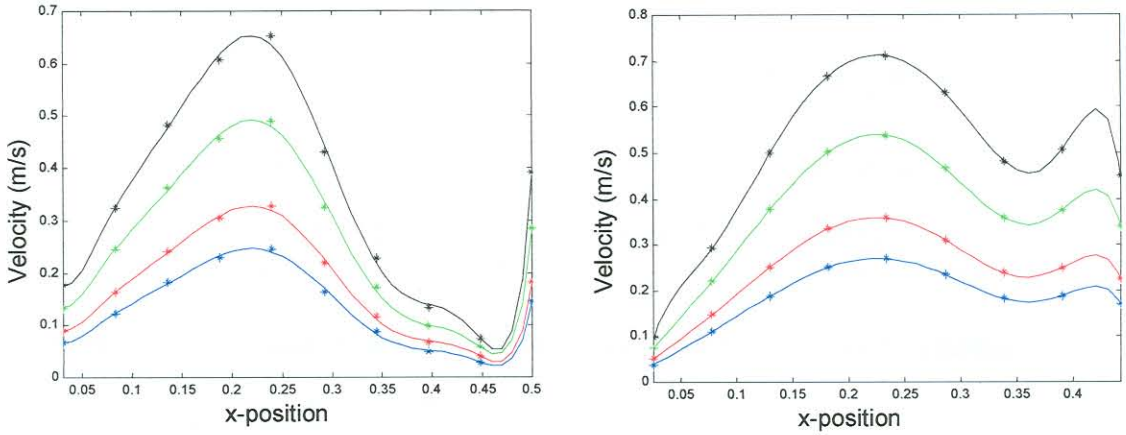

a) Bottom section *b) Top section*

Figure C.5: Velocity magnitude as a function of the x position (blue – 6 kg/s, red – 8kg/s, green – 12kg/s and black – 16 kg/s)

$$v_{bottom} = -397056\frac{\dot{m}}{4}x^8 + 600518\frac{\dot{m}}{4}x^7 - 376220\frac{\dot{m}}{4}x^6 + 130084\frac{\dot{m}}{4}x^5 - 27282.5\frac{\dot{m}}{4}x^4 + 3320.25\frac{\dot{m}}{4}x^3 - 209.832\frac{\dot{m}}{4}x^2 + 15.3587\frac{\dot{m}}{4}x^1 - 0.061492 \quad \text{C.1}$$

$$v_{top} = 10028.2\frac{\dot{m}}{4}x^8 - 19720.4\frac{\dot{m}}{4}x^7 + 15798.1\frac{\dot{m}}{4}x^6 - 6642.2\frac{\dot{m}}{4}x^5 + 1583.12\frac{\dot{m}}{4}x^4 - 217.95\frac{\dot{m}}{4}x^3 + 16.8099\frac{\dot{m}}{4}x^2 - 0.58031\frac{\dot{m}}{4}x^1 + 0.011452 \quad \text{C.2}$$

C.2.2 Baffle type 2 and 3

$$v_{bottom} = -196647\frac{\dot{m}}{4}x^8 + 412463\frac{\dot{m}}{4}x^7 - 354926\frac{\dot{m}}{4}x^6 + 161633\frac{\dot{m}}{4}x^5 - 41961\frac{\dot{m}}{4}x^4 + 6256.0\frac{\dot{m}}{4}x^3 - 518.73\frac{\dot{m}}{4}x^2 + 22.2633\frac{\dot{m}}{4}x^1 - 0.31878 \quad \text{C.3}$$

$$v_{top} = 4229.38\frac{\dot{m}}{4}x^6 - 6359.13\frac{\dot{m}}{4}x^5 + 3617.4\frac{\dot{m}}{4}x^4 - 956.5614\frac{\dot{m}}{4}x^3 + 114.8707\frac{\dot{m}}{4}x^2 - 4.972265\frac{\dot{m}}{4}x^1 + 0.096557 \quad \text{C.4}$$

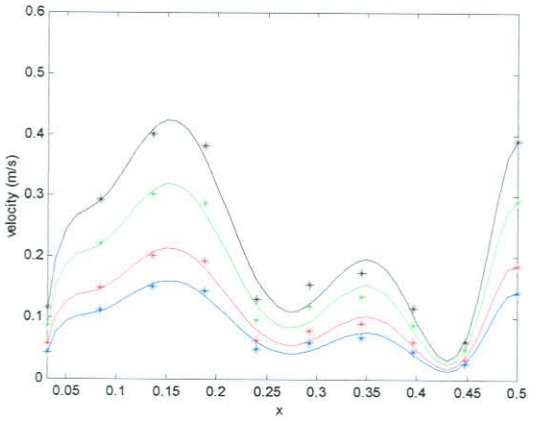

a) Bottom section

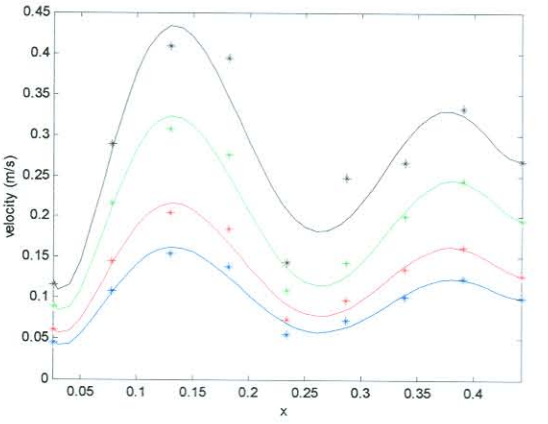

b) Top section

Figure C.6: Velocity magnitude as a function of the x position (blue – 6 kg/s, red – 8kg/s, green – 12kg/s and black – 16 kg/s)

C.3 Inlet section: Average cross-flow velocity magnitude equations

C.3.2 Baffle type 2 and 3

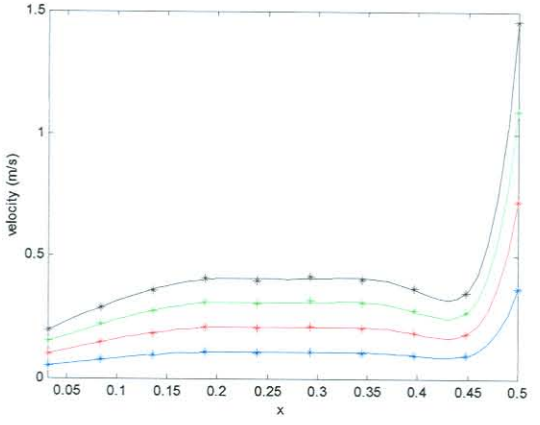

a) Bottom section

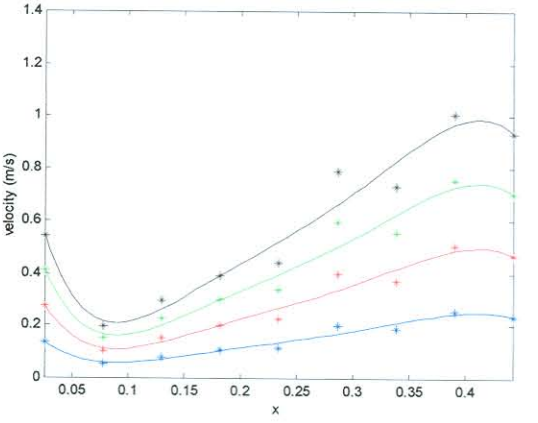

b) Top section

Figure C.7: Velocity magnitude as a function of the x position (blue – 6 kg/s, red – 8kg/s, green – 12kg/s and black – 16 kg/s)

$$v_{bottom} = 9058.91\frac{\dot{m}}{2}x^8 - 13489.6\frac{\dot{m}}{2}x^7 + 7792.74\frac{\dot{m}}{2}x^6 - 2200.15\frac{\dot{m}}{2}x^5 + 317.73\frac{\dot{m}}{2}x^4 - 23.209\frac{\dot{m}}{2}x^3 + 0.44214\frac{\dot{m}}{2}x^2 - 0.25877\frac{\dot{m}}{2}x^1 + 0.016375 \quad \text{C.5}$$

$$v_{top} = 244.577\frac{\dot{m}}{2}x^6 - 555.813\frac{\dot{m}}{2}x^5 + 447.075\frac{\dot{m}}{2}x^4 - 172.079\frac{\dot{m}}{2}x^3 + 34.402\frac{\dot{m}}{2}x^2 - 3.1311\frac{\dot{m}}{2}x^1 + 0.12839 \qquad \text{C.6}$$

Appendix D

Measuring positions

D.1 Measuring positions

D.1.1 Strain gauge positions

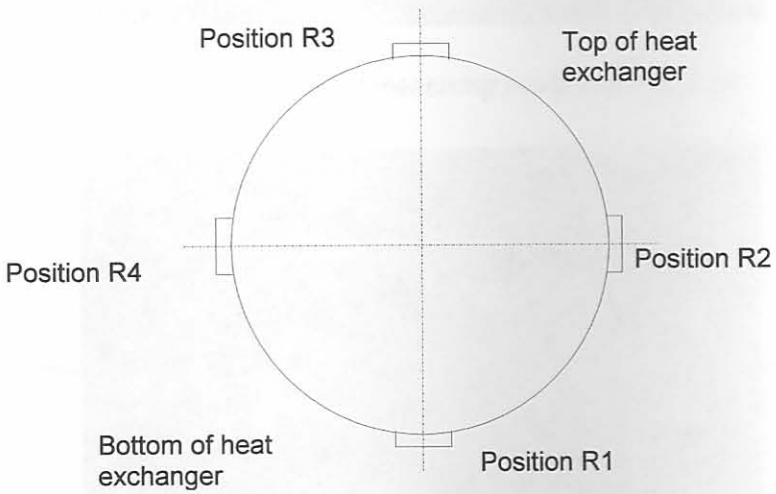

Figure D.1: Strain gauge positions

Measurements at R1 to R4 were taken with KFW-5-120-C1-16L5M2R strain gauges. The strain gauges at position R3 gave some problems and no measurements were taken at that position. Variation in strain was measured at the remaining positions

D.1.2 Support measurement positions

Measurements at B1 to B4 were taken with 2V/g accelerometers.

- B1 measuring acceleration in the negative x-direction
- B2 measuring acceleration in the negative z-direction
- B3 measuring acceleration in the positive y-direction
- B4 measuring acceleration in the negative x-direction

Figure D.2: Support measuring positions B1 and B2

Figure D.3: Supports measuring positions B3 and B4

D.1.3 Shell measurement positions

Measurements taken at A1, A3 and A4 were taken with 500mV/g accelerometers. The measurements as A2 were taken with a 100mV/g accelerometer.

- A1 measuring acceleration in the negative y-direction
- A2 and A3 measuring acceleration in the negative x-direction
- A4 measuring acceleration in the positive y-direction

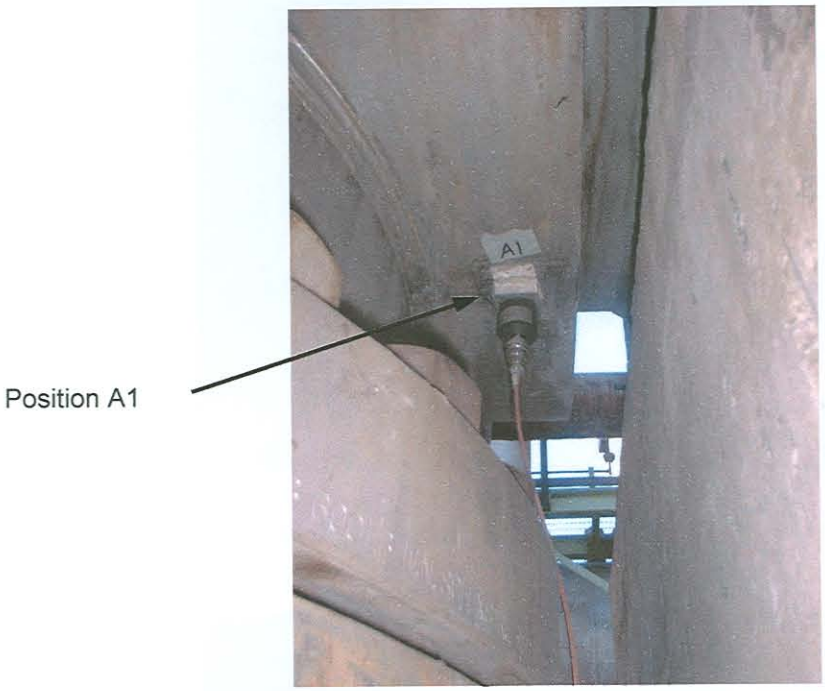

Figure D.4: Shell measuring position A1 (at outlet)

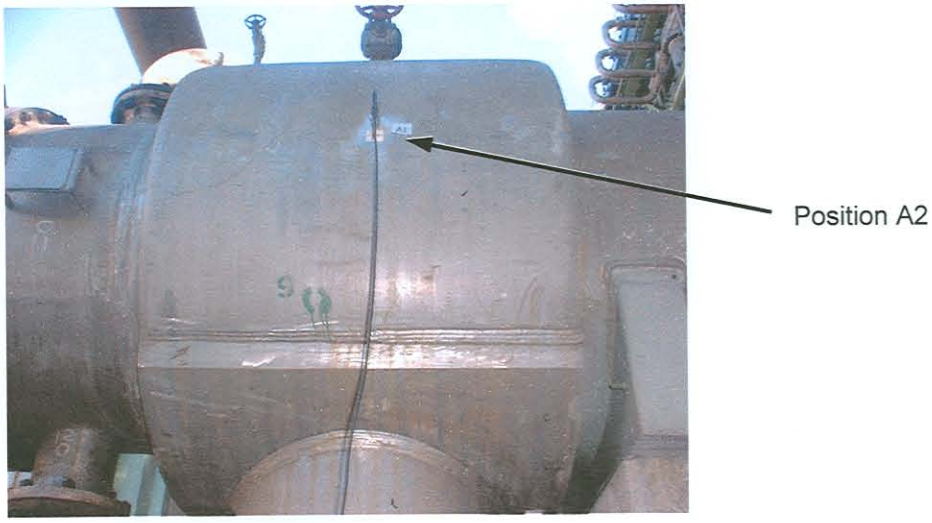

Figure D.5: Shell measuring position (A2) 90° from outlet

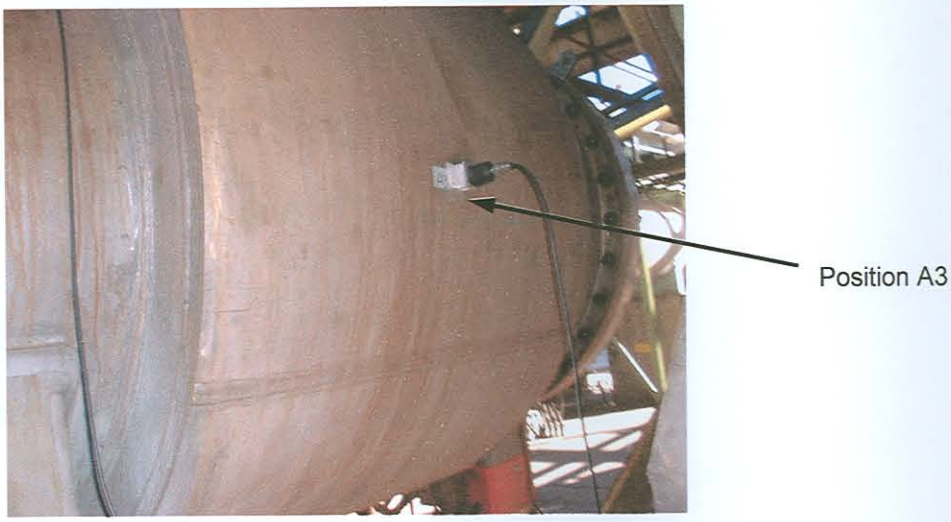

Figure D.6: Shell measuring position (A3) 90° from outlet

Figure D.7: Measuring position A1 at inlet

Appendix E

Experimental results

E.1 Experimental results

E.1.1 Strain gauge measurements

Position R1

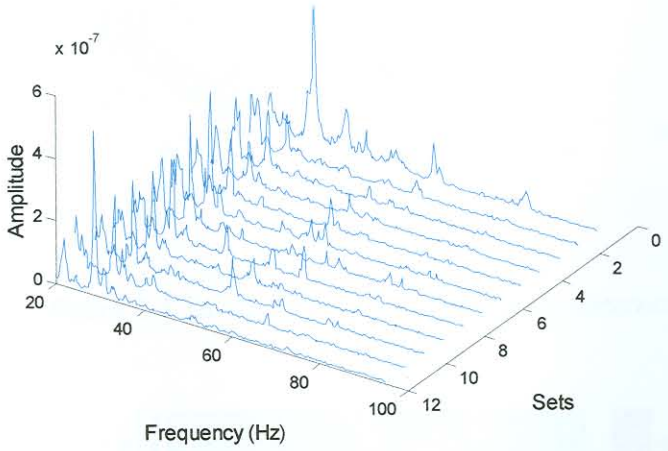

Figure E.1: Waterfall plot for strain gauge measurements

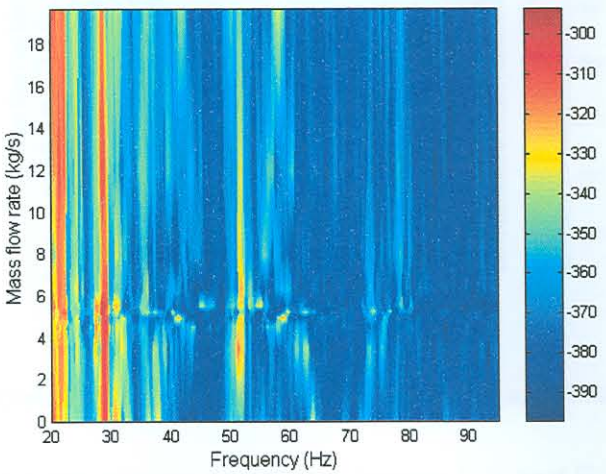

Figure E.2: Contour plot for strain gauge measurements

Increased strain amplitudes are visible at 28.5 Hz and a smaller peak 27.5 Hz, as well as at 52 Hz (figures E.1 and E.2). The 27.5 and 28.5 Hz peaks are similar to the predicted HTRI and FEM calculated values of 28.56 Hz and 27.76 Hz respectively.

Position R2

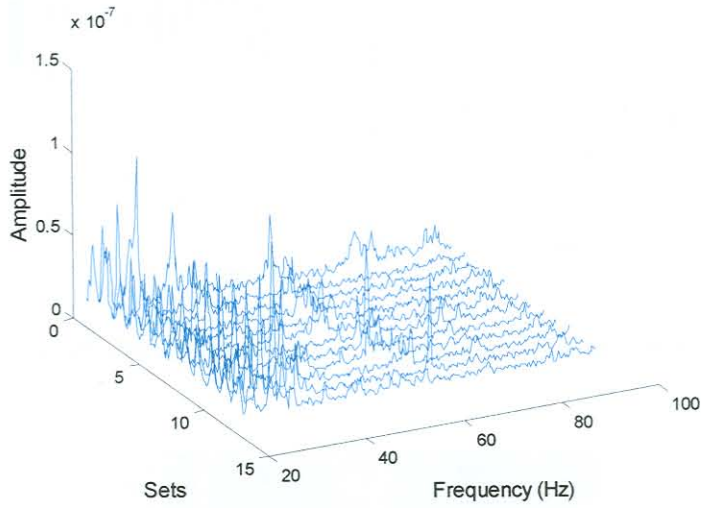

Figure E.3: Waterfall plot for strain gauge measurements

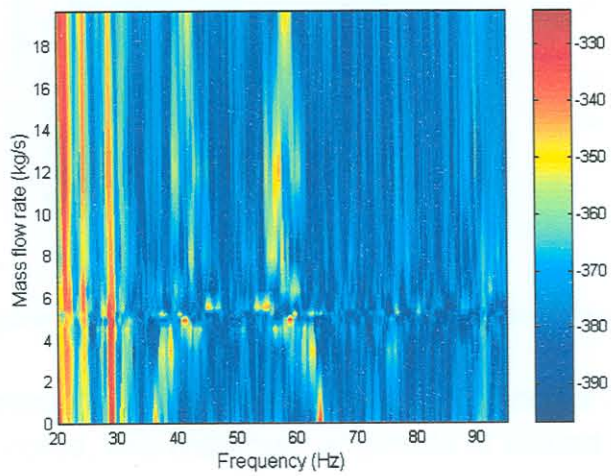

Figure E.4: Contour plot for strain gauge measurements

Figures E.3 and E.4 show similar results as figures E.1 and E.2, with an increase in strain amplitude at 29 Hz. This value is also similar to the predicted values.

Position R4

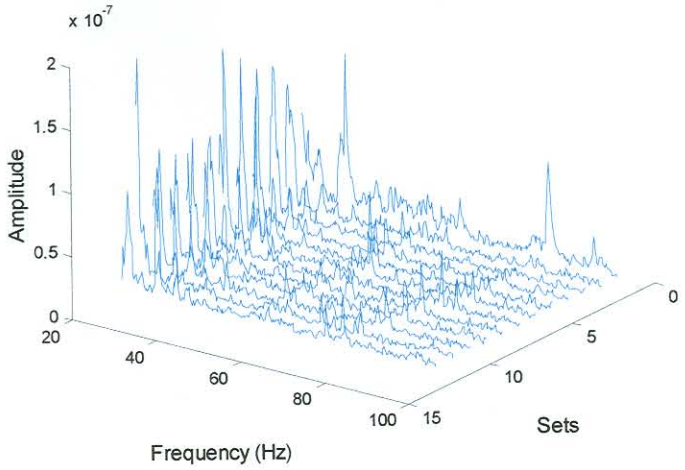

Figure E.5: Waterfall plot for strain gauge measurements

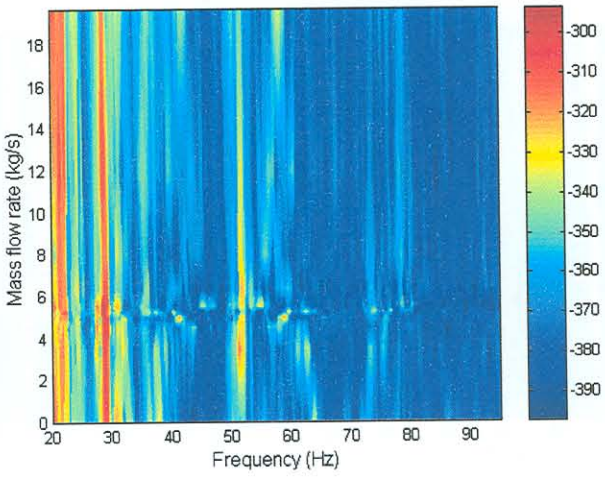

Figure E.6: Contour plot for strain gauge measurements

In figure E.6 an increase in strain amplitude at a frequency of 28.7 Hz through the flow ranges can be noted, with maximum amplitude at around 6 kg/s.

The strain gauge measurements at all three positions indicate vibration at a frequency between 28 Hz and 29 Hz. This corresponds well to the predicted values.

E.1.2 Support measurements

Position B1

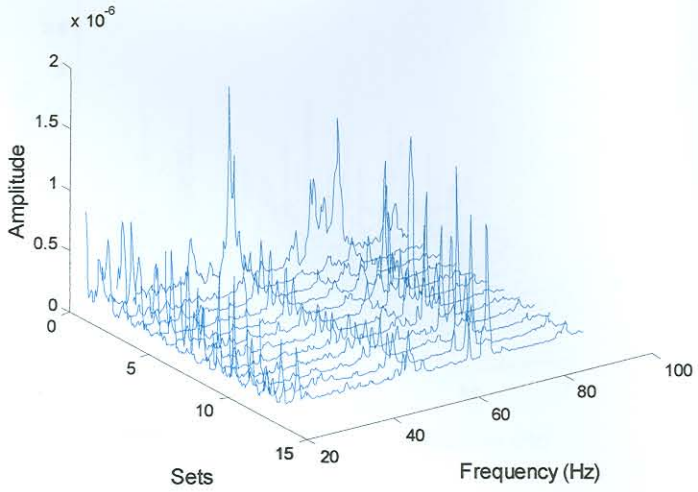

Figure E.7: Waterfall plot of support measurements

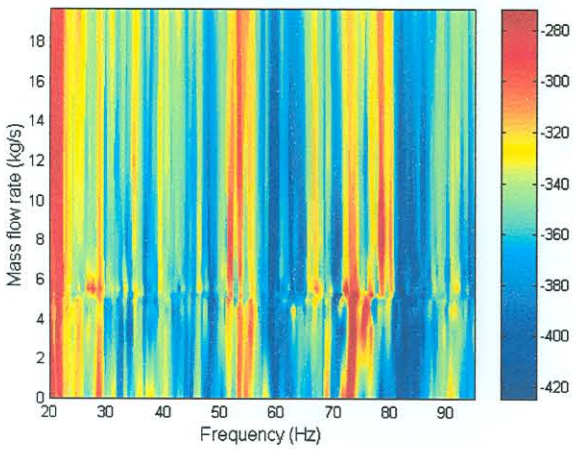

Figure E.8: a) Contour plot of support measurements

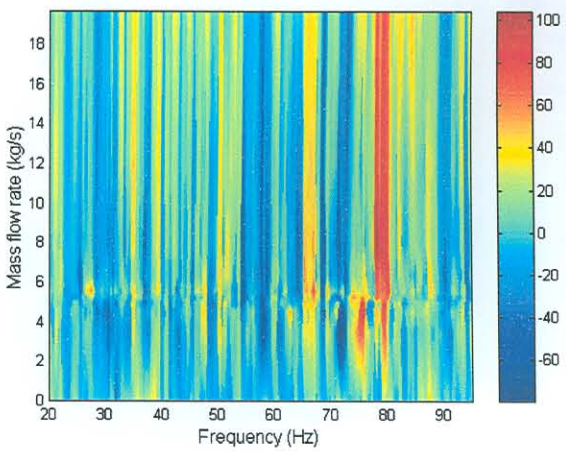

b) Contour plot of difference in support measurements

In figures E.7 and E.8a), a frequency at 28.5 Hz is visible up until 16 kg/s, after which it starts to decrease in amplitude. Other noticeable frequencies are at 52 Hz and 80 Hz. In figure E.15b) an increase in amplitude at a mass flow rate of 6 kg/s and 27.5 Hz is observed, as well as an increase in amplitude at 65 Hz between a mass flow rate of 6kg/s and 16 kg/s. Again there is a good correlation between the measured frequencies of 28.5 Hz and 27.5 Hz, and the predicted values.

Position B2

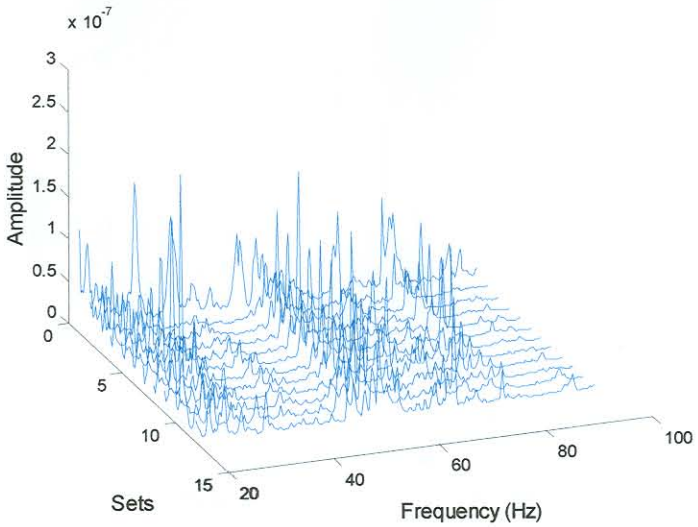

Figure E.9: Waterfall plot of support measurements

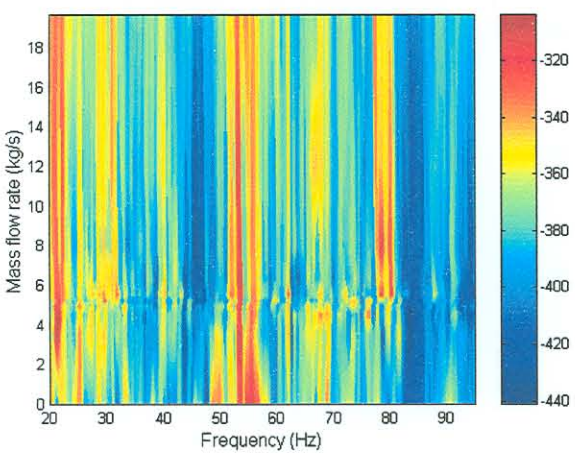

Figure E.10: a) Contour plot of support measurements

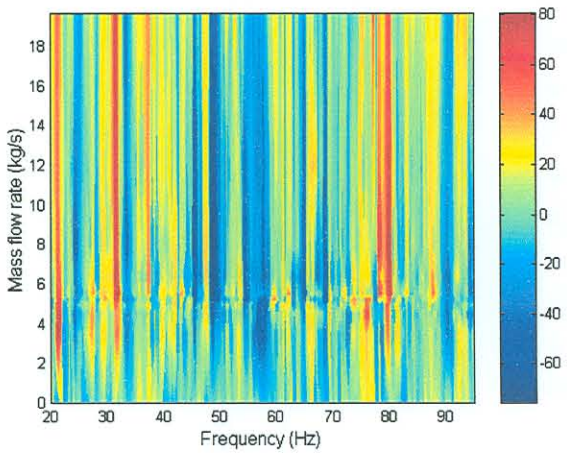

b) Contour plot of difference in support measurements

No increase in vibration is observed at the predicted values, there are however an increase in vibration at 53 Hz and 80 Hz (figures E.9 and E.10 a). In figure E.10 b) the non-operational measurements are deducted from the operational measurements. In that figure no frequency band at 53 Hz is observed, this indicates that the vibration was coming from an external source.

Position B3

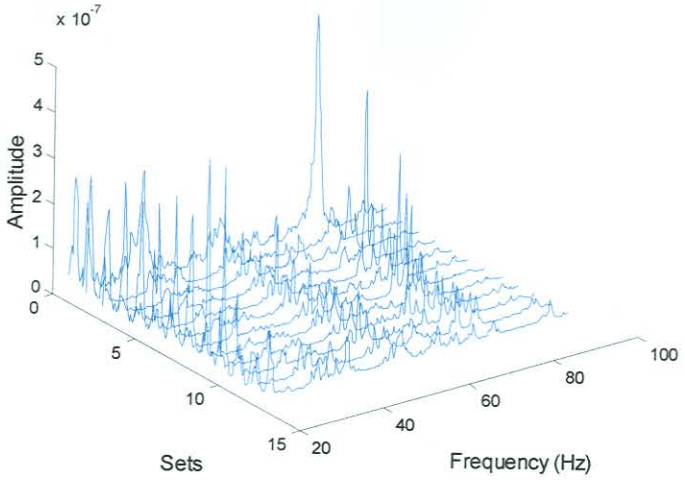

Figure E.11: Waterfall plot of support measurements

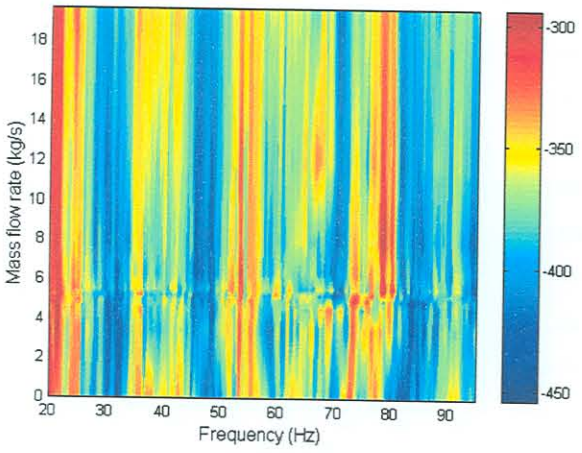

Figure E.12: a) Contour plot of support measurements

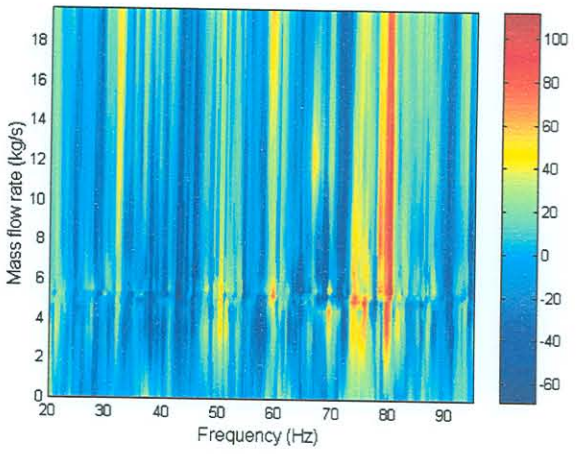

b) Contour plot of difference in support measurements

Figure E.12 a) and b) indicates vibration at a frequency of 80 Hz from a mass flow rate of 3 kg/s and upward. Figure E.18 also indicates vibration at a frequency of 25 Hz throughout the mass flow range, as well as frequency band between 35 Hz and 43 Hz, and 53 Hz and 56 Hz.

Position B4

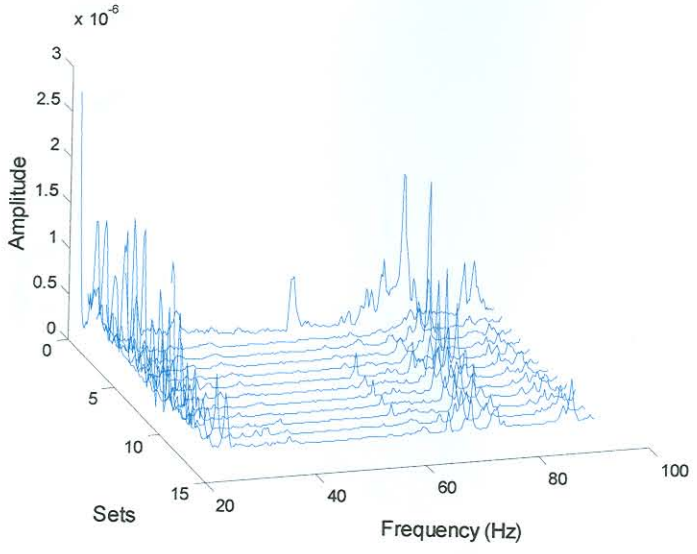

Figure E.13: Waterfall plot of support measurements

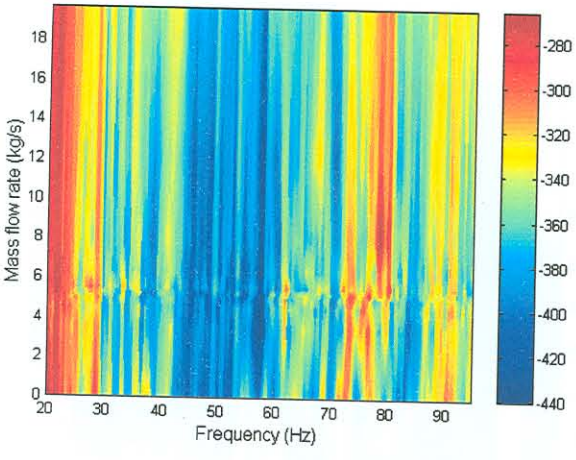

Figure E.14: a) Contour plot of support measurements

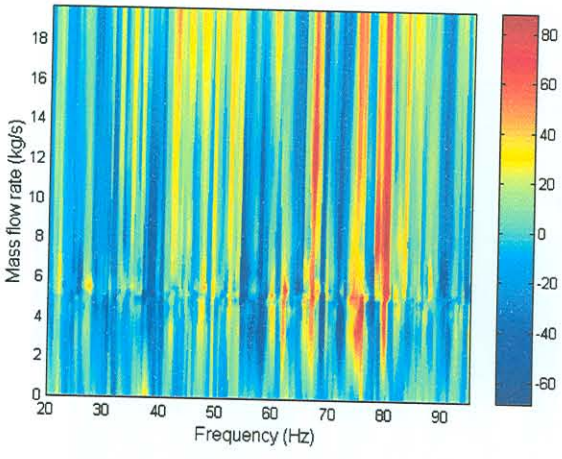

b) Contour plot of difference in support measurements

Throughout the flow range, vibration at a frequency of 28.5 Hz, is observed (figures E.13 and E.14 a). In figure E.14 b) a peak at 6 kg/s and 27.5 Hz is also visible. Good correlation between the predicted values from Chapter 2 are again obtained.

E.1.3 Shell measurements

Position A1

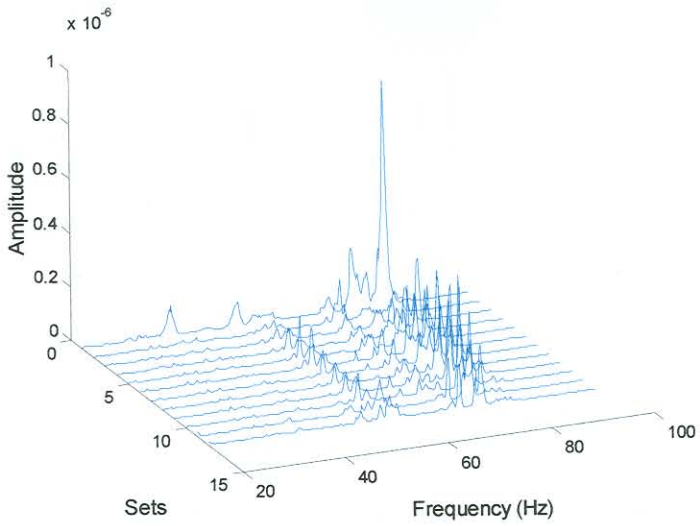

Figure E.15: Waterfall plot of shell measurements

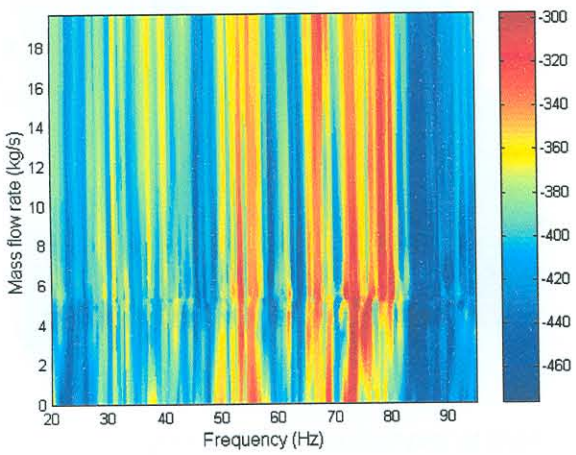

Figure E.16: a) Contour plot of shell measurements

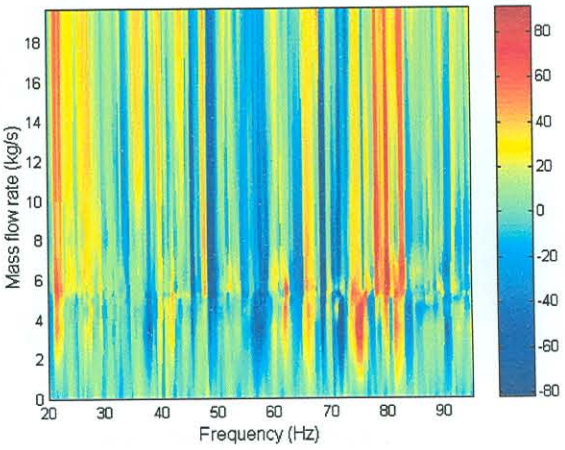

b) Contour plot of difference in shell measurements

Frequency band between 50 Hz and 60 Hz, as well as between 70 Hz and 80 Hz are observed (figures. E.15 and E.16 a). No vibration is visible at the expected frequencies.

Position A2

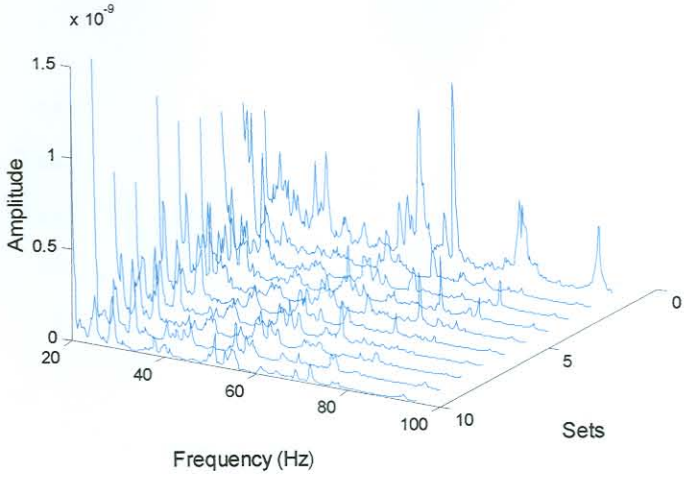

Figure E.17: Waterfall plot of shell measurements

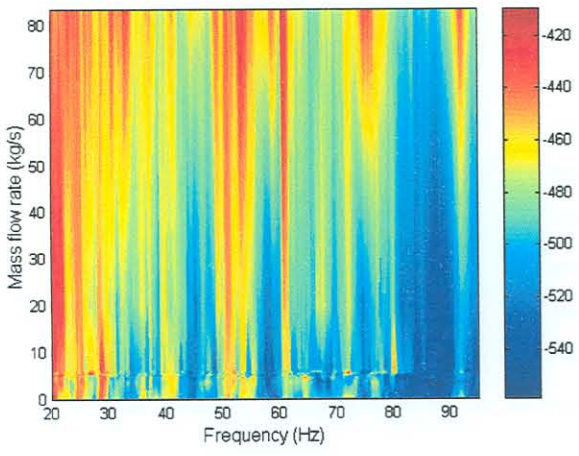

Figure E.18: a) Contour plot of shell measurements

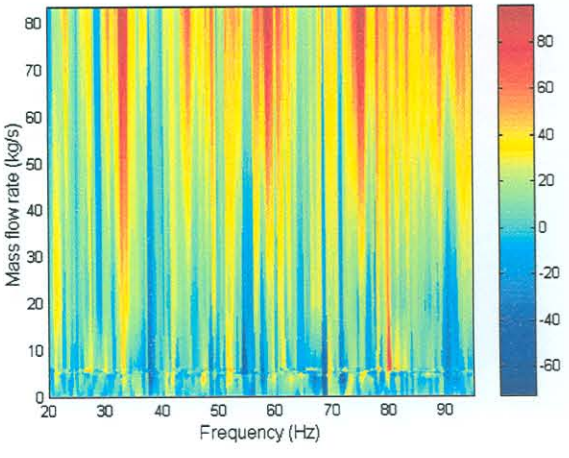

b) Contour plot of difference in shell measurements

At 24 Hz and 28Hz, increase in acceleration was recorded throughout the mass flow range. At a frequency of 32 Hz, an increase in amplitude is noted from a mass flow range of about 5 kg/s and upwards (figures E.17 and E.18).

Position A3

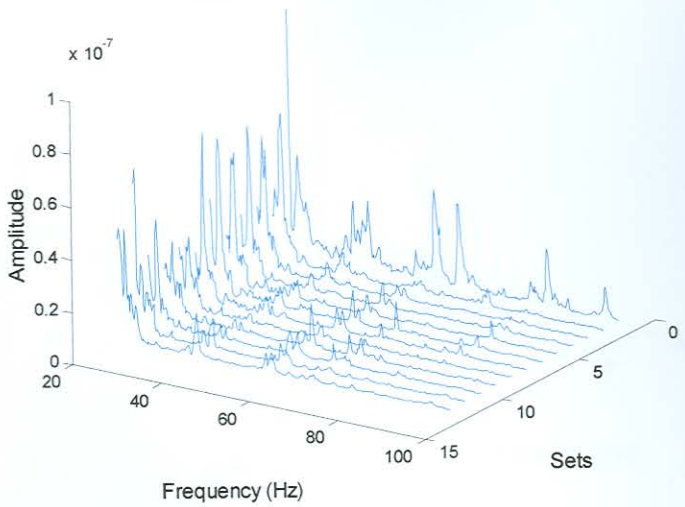

Figure E.19: Waterfall plot of shell measurements

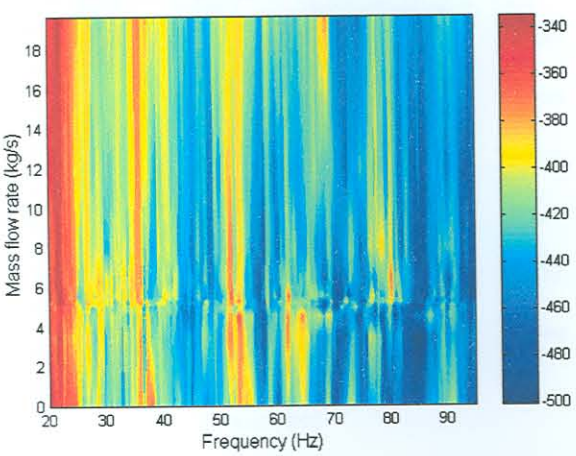

Figure E.20: a) Contour plot of shell measurements

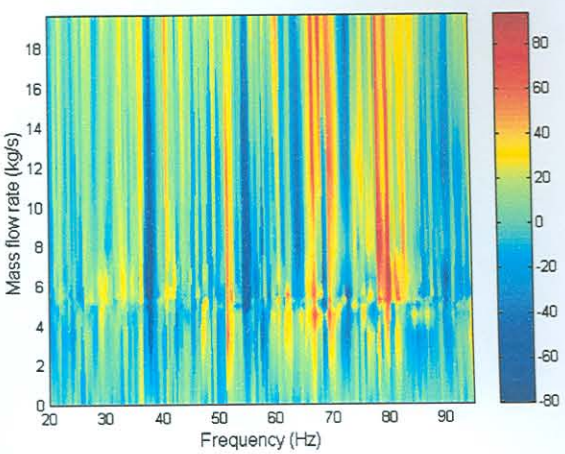

b) Contour plot of difference in shell measurements

In figure E.20 a), vibration at a frequency of 36 Hz throughout the flow range was measured. The amplitude of vibration at this frequency, increased as the mass flow rate was increased. (Also see figure E. 19)

Position A4

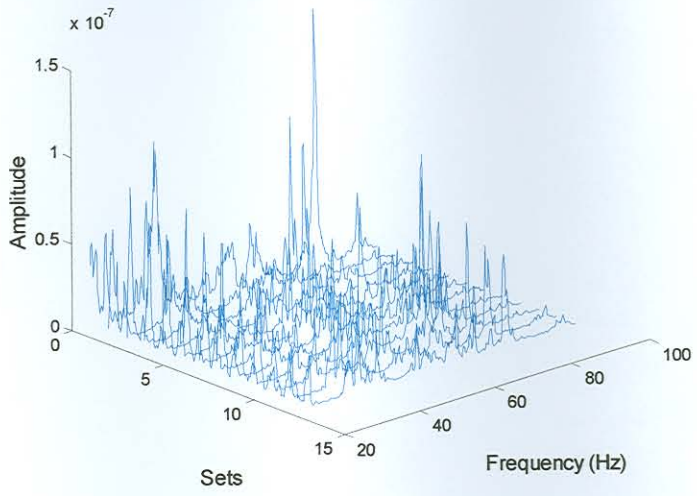

Figure E.21: Waterfall plot of shell measurements

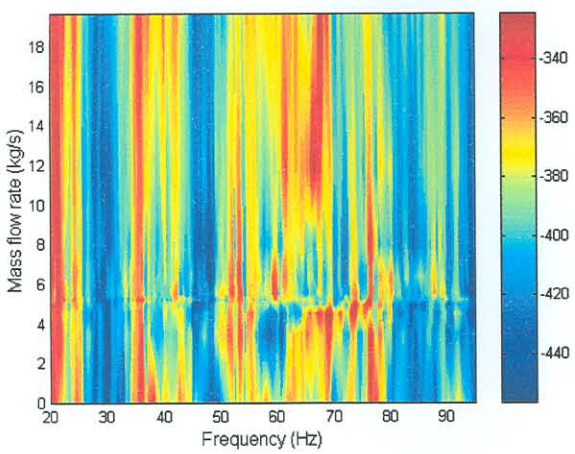

Figure E.22: a) Contour plot of shell measurements

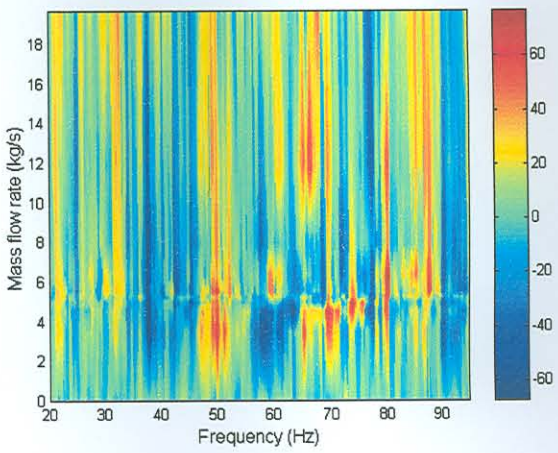

b) Contour plot of difference in shell measurements

Vibration at a frequency of 36 Hz is again observed in figure E.22 a). Figure E.22 b) also indicates an increase in vibration at this frequency from a mass flow rate of 4 kg/s and upwards. An increase in acceleration was also measured at 25 Hz (figure E.21).